

## CASSINI IMAGING SCIENCE: INSTRUMENT CHARACTERISTICS AND ANTICIPATED SCIENTIFIC INVESTIGATIONS AT SATURN

CAROLYN C. PORCO<sup>1,\*</sup>, ROBERT A. WEST<sup>2</sup>, STEVEN SQUYRES<sup>3</sup>, ALFRED McEWEN<sup>4</sup>, PETER THOMAS<sup>3</sup>, CARL D. MURRAY<sup>5</sup>, ANTHONY DELGENIO<sup>6</sup>, ANDREW P. INGERSOLL<sup>7</sup>, TORRENCE V. JOHNSON<sup>2</sup>, GERHARD NEUKUM<sup>8</sup>, JOSEPH VEVERKA<sup>3</sup>, LUKE DONES<sup>9</sup>, ANDRE BRAHIC<sup>10</sup>, JOSEPH A. BURNS<sup>3</sup>, VANCE HAEMMERLE<sup>2</sup>, BENJAMIN KNOWLES<sup>1</sup>, DOUGLAS DAWSON<sup>4</sup>, THOMAS ROATSCH<sup>11</sup>, KEVIN BEURLE<sup>5</sup> and WILLIAM OWEN<sup>2</sup>

<sup>1</sup>*CICLOPS/Space Science Institute, Boulder, CO, U.S.A.*

<sup>2</sup>*Jet Propulsion Laboratory, Pasadena, CA, U.S.A.*

<sup>3</sup>*Cornell University, Ithaca, New York, U.S.A.*

<sup>4</sup>*University of Arizona, Tucson, AZ, U.S.A.*

<sup>5</sup>*Queen Mary, University of London, London, England*

<sup>6</sup>*NASA Goddard Institute for Space Studies, New York, New York, U.S.A.*

<sup>7</sup>*California Institute of Technology, Pasadena, CA, U.S.A.*

<sup>8</sup>*Freie Universität, Berlin, Germany*

<sup>9</sup>*Southwest Research Institute, Boulder, CO, U.S.A.*

<sup>10</sup>*Université Paris 7-Denis Diderot, Paris, France*

<sup>11</sup>*DLR, Berlin, Germany*

(\*Author for correspondence: E-mail: carolyn@ciclops.org)

(Received 8 January 2004; Accepted in final form 18 May 2004)

**Abstract.** The Cassini Imaging Science Subsystem (ISS) is the highest-resolution two-dimensional imaging device on the Cassini Orbiter and has been designed for investigations of the bodies and phenomena found within the Saturnian planetary system. It consists of two framing cameras: a narrow angle, reflecting telescope with a 2-m focal length and a square field of view (FOV)  $0.35^\circ$  across, and a wide-angle refractor with a 0.2-m focal length and a FOV  $3.5^\circ$  across. At the heart of each camera is a charged coupled device (CCD) detector consisting of a 1024 square array of pixels, each  $12\ \mu$  on a side. The data system allows many options for data collection, including choices for on-chip summing, rapid imaging and data compression. Each camera is outfitted with a large number of spectral filters which, taken together, span the electromagnetic spectrum from 200 to 1100 nm. These were chosen to address a multitude of Saturn-system scientific objectives: sounding the three-dimensional cloud structure and meteorology of the Saturn and Titan atmospheres, capturing lightning on both bodies, imaging the surfaces of Saturn's many icy satellites, determining the structure of its enormous ring system, searching for previously undiscovered Saturnian moons (within and exterior to the rings), peering through the hazy Titan atmosphere to its yet-unexplored surface, and in general searching for temporal variability throughout the system on a variety of time scales. The ISS is also the optical navigation instrument for the Cassini mission. We describe here the capabilities and characteristics of the Cassini ISS, determined from both ground calibration data and in-flight data taken during cruise, and the Saturn-system investigations that will be conducted with it. At the time of writing, Cassini is approaching Saturn and the images returned to Earth thus far are both breathtaking and promising.

**Keywords:** Cassini, Saturn, Imaging, Rings, Moons



*Space Science Reviews* **115**: 363–497, 2004.

© 2004 Kluwer Academic Publishers. Printed in the Netherlands.

## 1. Introduction

On October 15, 1997, the Cassini spacecraft was launched to the planet Saturn from Cape Canaveral Launch Pad 40. When it reaches and begins orbiting Saturn on July 1, 2004, UTC it will become, at 10 AU from the Sun, the farthest robotic orbiter that humankind has ever established in the solar system. The nominal mission duration of 4 years and the variable orbit design will allow an unprecedented exploration of the Saturn system tour over an extended period from a variety of illumination and viewing geometries. Saturn's atmosphere, rings, icy satellites, Titan, and their mutual interactions will all be monitored for temporal changes in a way not previously possible during the Pioneer and Voyager flyby missions.

The Cassini Imaging Science Subsystem (ISS), the most sophisticated, highest-resolution two-dimensional imaging device ever carried into the outer solar system, has been specifically designed to image bodies in the Saturn system. In its photometric sensitivity, linearity and dynamic range, its spectral range and filter complement, resolving power and variety of data collection and compression modes, it represents a significant advance over its predecessor carried on Voyager, as demonstrated by the images obtained during the Cassini Jupiter flyby (Porco *et al.*, 2003). As on other Saturn-bound spacecraft, the ISS is also the instrument used for optical navigation of the spacecraft.

The cruise to Saturn entailed gravity assist flybys of Venus (one in 1998 and another in 1999), Earth (1999) and Jupiter (2000/2001), and a relatively close (1.5 million km) serendipitous flyby of the asteroid Masursky (2000). Aside from the usual periodic in-flight instrument checkouts during which images were collected of stars (Spica, Fomalhaut, Pleiades) for spectral and geometric calibration and for assessing instrument performance, the ISS acquired imaging data only during the Earth, Masursky, and Jupiter flybys. Earth flyby provided the first opportunity to take scientific data on planetary targets – in that case, the Moon – as well as to test in flight the stray light rejection capabilities of the ISS instrument by imaging very near the limb of the Moon. The Masursky flyby saw the first use of the autonomous target-tracking capability of the Cassini spacecraft, and the promise of future success in steady imaging during periods of rapidly changing geometry during the Cassini orbital tour. Finally, the Jupiter flyby was the first attempt to operate the spacecraft as it would be used at Saturn, using simple pointing mosaics and modules, data management in the solid-state recorder (SSR), etc., and indicated (as have subsequent observations) accurate absolute and relative pointing and a steady spacecraft. These results, as well as images collected on approach to Saturn in early 2004 (Figures 1 and 2), open up the exciting possibility of extremely high-quality, sharp, high signal-to-noise (S/N) images of all Saturn targets, bright and dark, and promise the opening of a new era in outer planet studies.

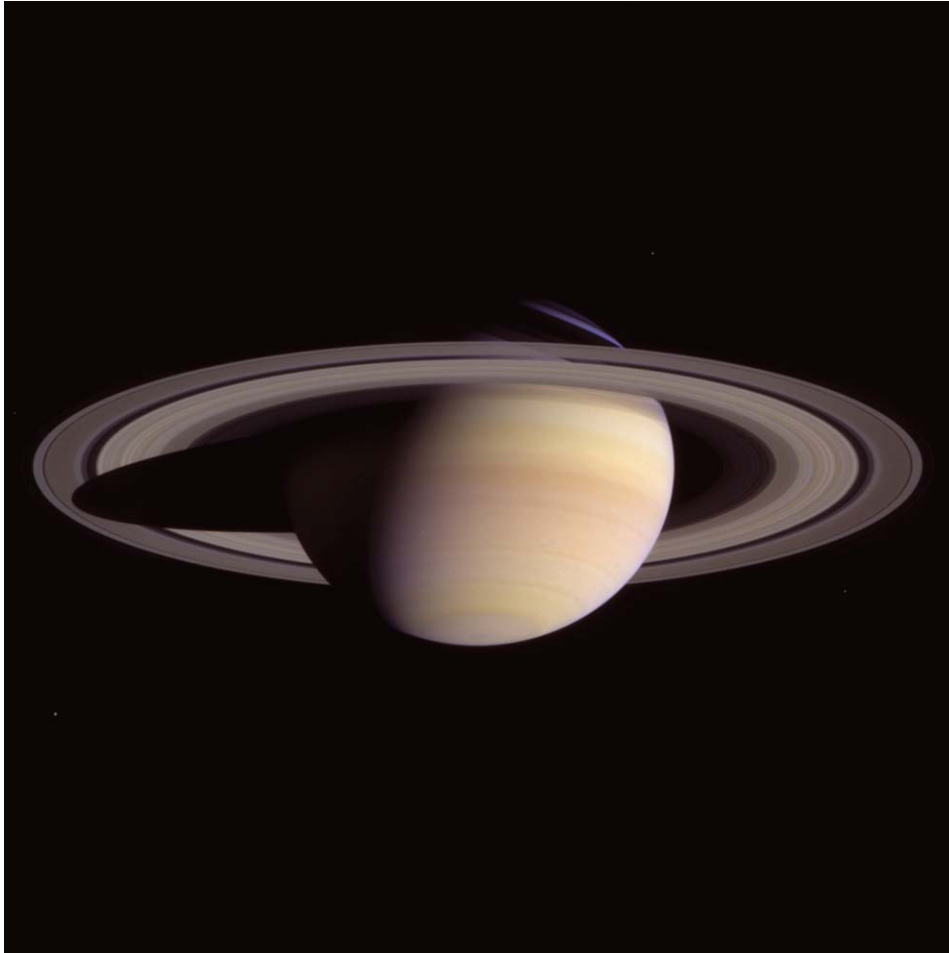


*Figure 1.* Saturn and its rings completely fill the field of view of Cassini's narrow-angle camera in this natural color image taken on March 27, 2004. This was the last single 'eyeful' of Saturn and its rings achievable with the narrow-angle camera on approach to the planet. The image shown here is a composite of three exposures in red, green, and blue, taken when the spacecraft was 47.7 million km (29.7 million miles) from the planet. The image scale is 286 km (178 miles) per pixel. Color variations between atmospheric bands and features in the southern hemisphere of the planet, as well as subtle color differences across Saturn's middle B ring, are evident.

In this article, we describe the scientific investigations that the Cassini Imaging Team (Table I) intends to conduct at Saturn (Section 2), and the characteristics of the Cassini Imaging Science Subsystem that make these investigations possible (Section 3). We also present the results of the instrument calibrations that have been performed thus far using both ground calibration data taken before launch and data taken in flight.

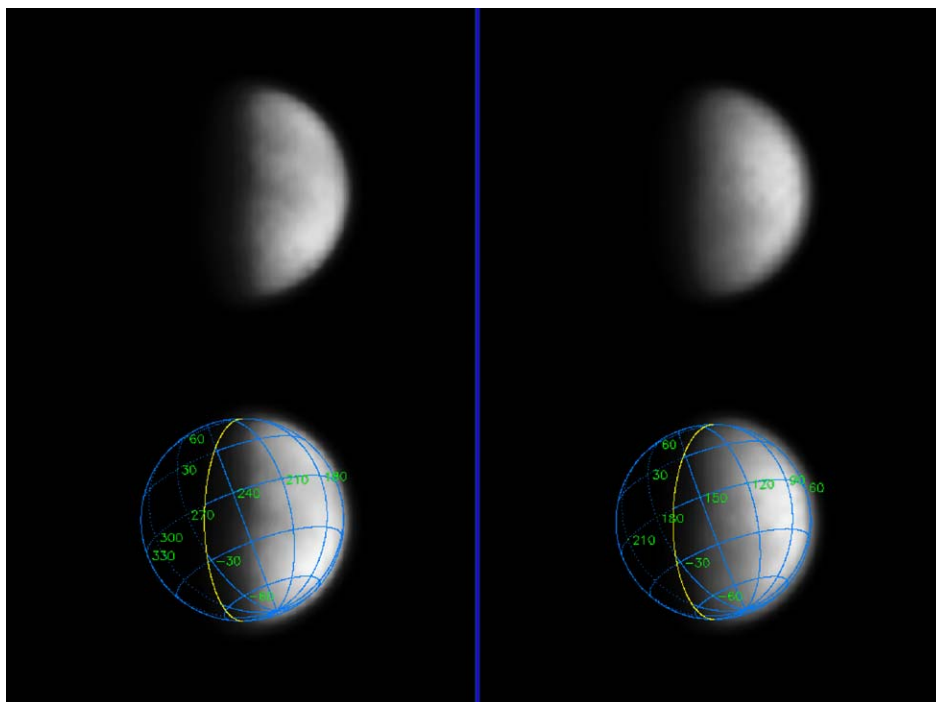


*Figure 2.* Two narrow-angle camera Titan images, each 38 s exposure, taken 4 days apart in mid-April, 2004, through the CB3 (938 nm) filter at an image scale of  $\sim 230$  km/pixel. The images have been magnified and smoothly interpolated by a factor of ten from the original images. Large-scale variations in brightness across the disk are real and can be correlated with features seen by Earth-based observers. The bottom images are the same two Titan images above, overlain with a Western longitude coordinate grid. The bright feature between  $-30^\circ$  latitude and the equator, and extending from  $\sim 60$  to  $120^\circ$  West longitude is Xanadu, the brightest feature on Titan.

## 2. Anticipated Imaging Science Investigations at Saturn

In this section, we describe the major outstanding questions concerning Saturn and its rings and moons that will be addressed by the Imaging Science experiment over the course of Cassini's multi-year orbital tour. In brief, the Cassini 4-year tour calls for:

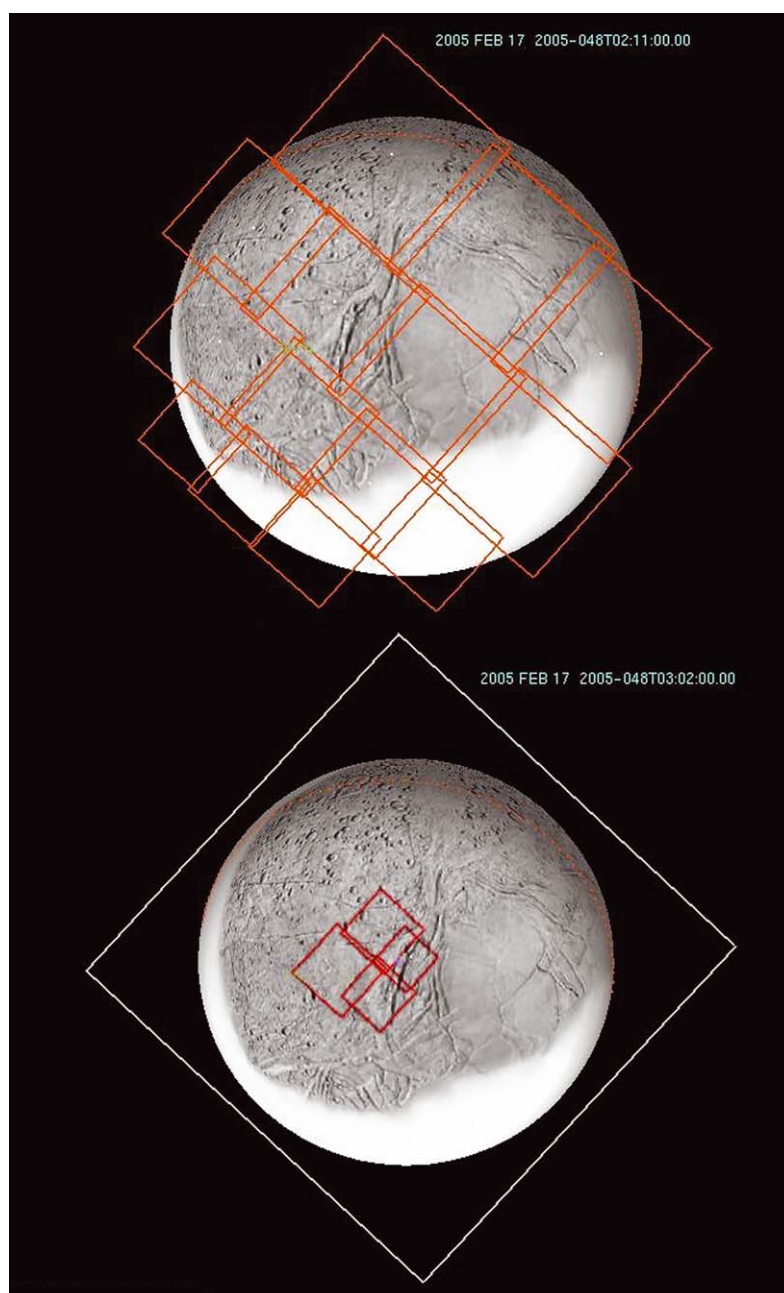
- repeated synoptic imaging of the planet and rings and Titan on approach to Saturn;
- a very close flyby of Phoebe on approach on June 11, 2004;
- extremely high-resolution imaging of the rings during the Saturn Orbit Insertion (SOI) maneuver when the spacecraft is skimming over the rings by only several tens of thousands of kilometers;

TABLE I  
Imaging team.

Carolyn Porco, Team Leader	Space Science Institute, Boulder, CO
Andre Brahic	Université Paris 7-Denis Diderot, Saclay, Paris
Joseph Burns	Cornell University, Ithaca, NY
Anthony DelGenio	NASA Goddard Institute for Space Studies, NY, NY
Henry Dones	Southwest Research Institute, Boulder, CO
Andrew Ingersoll	Caltech, Pasadena, CA
Torrence Johnson	Jet Propulsion Laboratory, Pasadena, CA
Alfred McEwen	University of Arizona, Tucson, AZ
Carl Murray	Queen Mary, University of London, London
Gerhard Neukum	Freie Universität, Berlin
Steven Squyres	Cornell University, Ithaca, NY
Peter Thomas	Cornell University, Ithaca, NY
Joseph Veverka	Cornell University, Ithaca, NY
Robert West	Jet Propulsion Laboratory, Pasadena, CA

- forty-five (45) close ‘targeted’ flybys of Titan (40 of which approach within 2500 km of the surface, and 24 of these within 1000 km of the surface);
- very close ‘targeted’ flybys of Enceladus (4) (Figure 3), Dione, Rhea, Iapetus, and Hyperion, all approaching within  $\sim 1500$  km of the surface;
- thirty-one (31) non-targeted but still close (within 100,000 km of the surface) flybys of Iapetus and the five major icy satellites Mimas, Enceladus, Tethys, Dione and Rhea;
- three (3) extended periods of inclined and low-periapse orbits (May–August 2005, September 2006–June 2007, and December 2007–June 2008) for high-resolution, high-latitude ring and Saturn observing;
- a dozen orbits with sufficiently distant apoapses to permit atmospheric movie making.

Imaging sequences planned for the nominal 4-year tour call for the acquisition of hundreds of thousands of images of known Saturn targets, as well as sequences designed to search for new satellites and faint ring material. Imaging scales on the targeted satellites will be as small as a few tens of meters/pixels; on the rings and atmosphere,  $\sim 1$  km/pixel. In comparison, the best Voyager resolution obtained on the Saturnian satellites was  $\sim 2$  km/pixel; on the rings and atmosphere,  $\sim 4$  km/pixel. The sophisticated capabilities of the ISS, together with Cassini’s upcoming variable and extended tour of the Saturn system, portend dramatic advances in our knowledge of this rich planetary system from the investigations described herein.



*Figure 3.* Example imaging sequence during part of an early 2005 close targeted flyby of Enceladus. Upper image shows the sequence of some frames at a range of about 29,000 km. Lower shows frames at about 9000 km range. Small boxes are narrow-angle images; large box in bottom example is the wide-angle field of view. Features mapped by Voyager are shown; white areas were not adequately imaged by Voyager. Best Voyager image is in Figure 7.

## 2.1. SATURN'S ICY SATELLITES

The Saturn satellite system, like that of the other giant planets, has several distinct components. The most distant outer population extends from 10 to 20 million km (out to the dynamical limit known as the ‘Hill’s sphere’), and is growing rapidly in number owing to successful ongoing ground-based telescopic searches for new Saturnian moons (Gladman *et al.*, 2001). At last count, this group contains 14 satellites, including Phoebe at a semi-major axis of 12.9 million km; none are believed to be bigger than  $\sim 20$  km across (except Phoebe at  $\sim 220$  km diameter), and about half (including Phoebe) are on retrograde orbits. With the exception of the close Phoebe flyby on approach to Saturn, no Cassini observations of this group of objects have been planned.

The inner population is a collection of bodies, from ring-embedded Pan at  $\sim 20$  km across to Mercury-sized Titan (Table II). It is arguably the most complex

TABLE II  
Saturnian satellite characteristics.

Satellite	$a (\times 10^3$ km)	Period (days)	Axes (km)			Radius (km)	Density (g cm $^{-3}$ )	References
Pan	133.59	0.5751				10		1
Atlas	137.64	0.6019	18		13	$16 \pm 4$		2
Prometheus	139.35	0.6129	70	50	37	$51 \pm 7$		2
Pandora	141.70	0.6288	55	43	32	$42 \pm 5$		2
Epimetheus	151.42	0.6946	70.2	54.1	51.9	$58.2 \pm 3$	$0.63 \pm 0.11$	3
Janus	151.42	0.6946	101.5	94.9	76.8	$90.5 \pm 3$	$0.65 \pm 0.08$	3
Mimas	185.52	0.9424	209.1	195.8	192.2	$198.9 \pm 0.5$	$1.12 \pm 0.03$	5, 4
Enceladus	238.02	1.3702	256.3	247.3	244.6	$249.4 \pm 0.3$	$1.00 \pm 0.03$	4
Tethys	294.66	1.8878	535.6	528.2	525.8	$529.8 \pm 1.5$	$0.98 \pm 0.02$	5
Calypso	294.66	1.8878	15	12	7	$11 \pm 3$		2
Telesto	294.66	1.8878	–	12	11	$12 \pm 3$		2
Dione	377.40	2.7369				$559 \pm 5$	$1.49 \pm 0.05$	6, 8
Helene	377.40	2.7369	17	–	14	$16 \pm 3$		2
Rhea	527.04	4.5175				$764 \pm 4$	$1.24 \pm 0.04$	7, 9
Titan	1221.85	15.9454				$2575 \pm 2$	$1.88 \pm 0.01$	10
Hyperion	1481.1	21.2766	164	130	107	$133 \pm 8$		11
Iapetus	3561.3	79.3302				$718 \pm 8$	$1.03 \pm 0.1$	9
Phoebe	12952.	550.48R	115	110	105	$110 \pm 3$		2

1: Showalter (1991); 2: Thomas *et al.* (1983); 3: Nicholson *et al.* (1992); 4: Dermott and Thomas (1994); 5: Thomas and Dermott (1991); 6: Davies and Katayama (1983a); 7: Davies and Katayama (1983b); 8: Harper and Taylor (1993); 9: Campbell and Anderson (1989); 10: Lindal *et al.* (1983); 11: Thomas *et al.* (1995).

collection of satellites in the solar system and exhibits an enormous variety in shape, size, planetocentric distance and surface characteristics. It contains 1430 km wide Iapetus, whose orbit is the most distant at 3.6 million km and somewhat inclined ( $\sim 15$  deg) to Saturn's equator; the small ( $\sim 300$  km wide) chaotic rotator Hyperion; haze-enshrouded Titan (5100 km across); the five major icy satellites Rhea, Dione, Tethys, Enceladus and Mimas (ranging linearly in size with distance from the planet from 1528 km Rhea to 396 km Mimas); the small (20–30 km) Trojans, Helene, Telesto and Calypso, of Tethys and Dione; and finally the remaining 'ring region' satellites Janus and Epimetheus (the 'co-orbitals'), the F ring shepherds Pandora and Prometheus, Atlas orbiting immediately outside the main rings, and Pan,  $\sim 20$  km across and orbiting within the main rings where we expect to find other small gap-clearing moons. It is this population that Cassini will investigate in depth.

The present-day physical, compositional and orbital characteristics of each of these bodies result from a combination of original formation conditions and subsequent surface and (possibly) orbit modification by external and internal processes operating over geologic time. Consequently, the ISS investigations of these bodies are focused on developing as complete and accurate a picture as possible of the visual properties of each satellite. Most of these inner satellites are tidally locked and synchronously rotating with their orbital periods. As a consequence, the Voyager spacecraft, each of which spent only a brief period of time in the Saturn system, imaged only one hemisphere of some of these moons at reasonably high ( $\sim 2$  km) resolution. Cassini's multi-year tour of the Saturn system, which includes global imaging of almost all these bodies, will in part be an initial reconnaissance of the other 'half' of the Saturnian system. Global spectral images at Voyager and better resolution, very high, sub-kilometer resolution images of localized regions, and repeated long distance images over the orbital tour for positional measurements are all part of the imaging sequences planned for the inner Saturnian satellites.

The diversity within the Saturnian satellite system, and its placement ten times farther from the Sun than that of Jupiter – the only other outer planet satellite system for which we have a moderately detailed view – provide an unusual opportunity to evaluate and disentangle the contributions of initial conditions and subsequent modifications to the satellites' present day attributes. With Cassini observations in hand, fundamental questions will be addressed, such as: How did heliocentric distance affect the composition of the original proto-Saturnian nebula materials and how did planetocentric distance affect their subsequent incorporation into the satellites? What have been the thermal and geologic histories of the Saturnian satellites? Which satellites have undergone tidal heating and do any have present-day subsurface oceans? How did the flux and chronology of impacts vary across the Saturnian system? How did the impactor populations and chronology vary across the outer solar system?

The ultimate goal of all Cassini satellite imaging investigations is to develop a more comprehensive view of the origin and evolution of the Saturnian system as



a whole, and that of outer giant planet satellite systems in general. Moreover, as a collection of bodies, all orbiting in the same plane, in the same direction, around the same massive central body, and nearly all formed from the same protoplanetary nebula, the inner Saturnian system resembles the assemblage of planets in orbit around the Sun. Consequently, the study of the Saturnian satellites will have direct impact on our understanding of the processes that were in play during the formation and subsequent differentiation and evolution of the planets. The multiplicity of satellite phenotypes around Saturn, and their distinctive characteristics when compared with the satellites of the other giant planets, offer an eagerly awaited chance to understand many fundamental aspects of planetary evolution.

The investigations of Titan, whose surface, and therefore geologic history, remain unknown, may well yield the single greatest scientific advance from the Cassini mission. Because the exploration of Titan by Cassini is special, and because the ISS has been especially equipped to penetrate the haze that obscured the surface to the Voyager cameras, we reserve a separate subsection to describe the pressing scientific questions surrounding it and our intended investigations.

#### 2.1.1. *Geomorphology*

Many of the fundamental questions about the composition, origin and evolution of the Saturnian satellites can be addressed by global and high-resolution imaging of surface morphology. The array of geological and photometric features on each satellite surface – such as crater densities, tectonic patterns, and albedo markings – tells not only the body's individual history, but may be used, in concert with other information, like mean density, to ascertain the trends across the system in composition, the physical conditions at time of formation, and other important factors that are relevant to the workings of the system as a whole.

Most morphological investigations to be addressed by imaging are relevant for all satellites. Determination of surface ages from crater density statistics is one such investigation, and is best accomplished with imaging at low solar elevation angles, where shadows are longest, and at resolutions as high as possible. The Galileo experience (Bierhaus *et al.*, 2001) has shown the usefulness of crater density measurements of sub-kilometer craters in revealing the order of geological events (stratigraphy) on satellite surfaces and in examining the mechanical properties of the substrate, although interpretations may be controversial. Many problems of general geologic evolution, such as crater degradation, tectonic faulting, cryovolcanism, viscous relaxation, isostatic rebound, and mass movements require accurate measurements of topography, including slopes. Slope information can be extracted from photometric and stereogrammetric measurements. The relative accuracy and utility of stereo imaging depend upon lighting conditions and the convergence angles and pixel scales of different images. For example, 50-m stereo images taken at a convergence angle of  $20^\circ$  (under similar lighting conditions) yield elevation accuracies of 13–26 m, depending on image contrast. The rapid flybys and slow maneuverability of the Cassini spacecraft require careful planning, use of both WA

and NA cameras, and combination of imaging from different satellite flybys to maximize high-resolution stereo data. Additionally, in some areas photoclinometry – the determination of slopes from the light scattering behavior of a surface whose photometric function is known – can be used to map relative topographic patterns. Photoclinometry can be used to measure slopes at higher spatial resolution with poorer control of regional slopes, than can stereogrammetry, so the two techniques are best combined (Giese *et al.*, 1996; Kirk *et al.*, 2003).

One geological example where critical topographic measurements are required is that of the ridged units on Enceladus, which are less than a few kilometers across and a few hundred meters high. Testing hypotheses for the formation of these ridges requires relative height determinations of a few tens of meters down to a few meters. Imaging resolutions of meter scale are also vital for the geologic mapping of ridge characteristics, a lesson learned in detail from Galileo's imaging of ridges on Europa (Figure 4; Carr *et al.*, 1998; Nimmo *et al.*, 2003). Another critical use of accurate local topographic measurements lies in mass wasting studies where measures of the filling of craters and other depressions, and the burial of otherwise positive relief features, are needed. The surprising findings of significant surface filling and erosion on Callisto from Galileo images (Moore *et al.*, 1998) show the need for these volume measures with vertical precision of tens of meters. Current tour scenarios allow for measurement of vertical displacements on some regions of Enceladus, Dione, Iapetus, Hyperion, Phoebe and possibly Rhea and Titan to a precision of a few tens of meter; areas on Mimas and Tethys may be imaged with lower resolution stereo.

Individual satellites present geological features that appear unique, and high-resolution imaging can address the question: what makes them so different? Iapetus is a prime example. The question of internal/external controls of its large albedo asymmetry has significance for both models of icy satellite interiors as well as orbital dynamics (Section 2.1.2). One requirement in imaging Iapetus is that both light and dark areas and the boundary between them be seen at favorable resolution and lighting. This requirement is met in the currently planned targeted flyby over the boundary. The low flyby speed allows high resolution ( $<50$  m/pixel) over many areas within the dark region, over brighter areas nearer the trailing side of Iapetus, and in several areas near the boundary where stratigraphic relations are sought. Planned imaging sequences include stereoscopic data and monoscopic mapping at high resolution to determine morphology and topography (as well as color and photometric sampling), much of this at much better than 1 km/pixel.

*2.1.1.1. Geodesy and Cartography.* High-resolution imaging is also required for the production of geometrically accurate maps. Correct maps are important tools for the planning of imaging activities when the objective is to point the camera precisely to specific targets. They also form the contextual basis for further geologic, geophysical and photometric studies of the satellites.

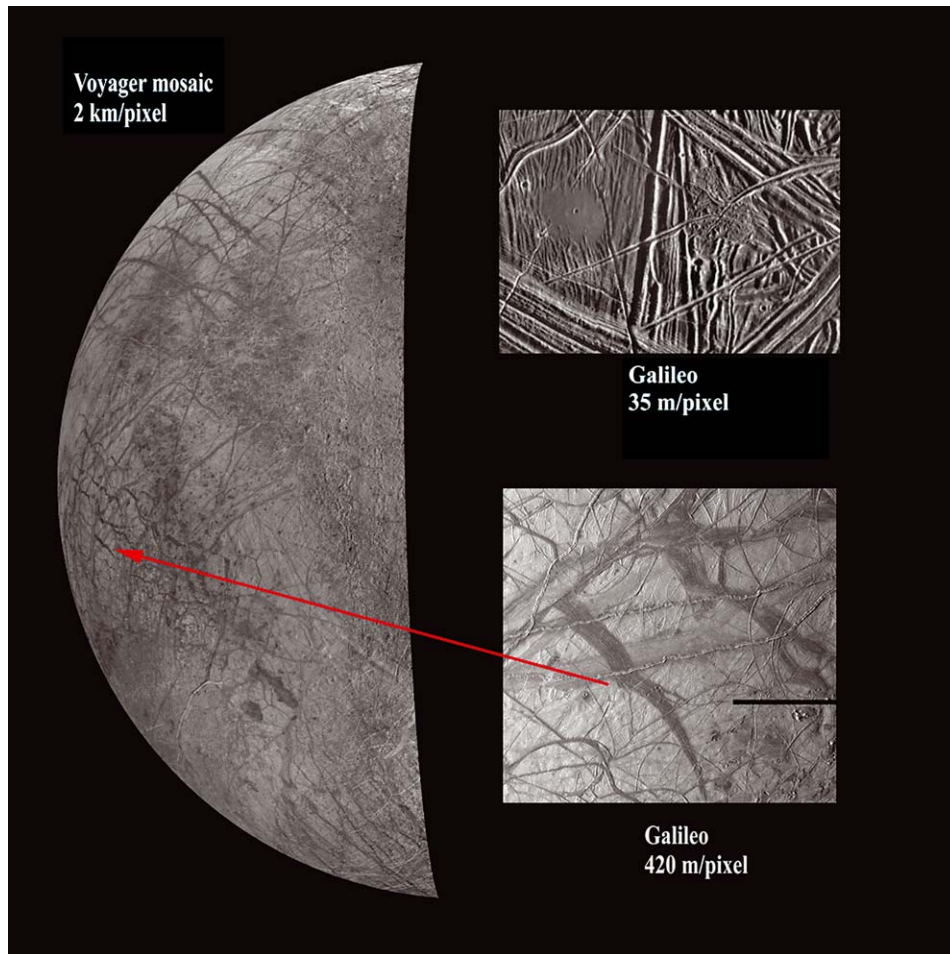


*Figure 4.* Voyager image of Jupiter's satellite, Europa, at 2 km/pixel, and two Galileo images at 420 and 35 m/pixel. The improvement in resolution from hundreds of meters/pixel to tens of meters/pixel altered the view of the morphology of Europa's 'bands' from one of crossing linear features to one of specific tectonic features of changing morphology, for which a robust chronology and morphology have been developed (see Carr *et al.*, 1998). The morphological relations revealed by high resolution are those between tectonic forms, and also between tectonics and craters and their ejecta. Image prepared by C. Philips, SETI.

The production of such maps begins with laying out networks of "control points", typically small craters, for which the coordinates in the satellite-fixed coordinate system must be determined. These are generally determined from large numbers of line/sample measurements of the control points in large numbers of images by "bundle block adjustment techniques", a dedicated inversion procedure used in photogrammetry (Davies *et al.*, 1998; Zeitler and Oberst, 1998; Oberst and Schuster, 2004). Solutions of the bundle block adjustment include latitudes, longitudes, radii

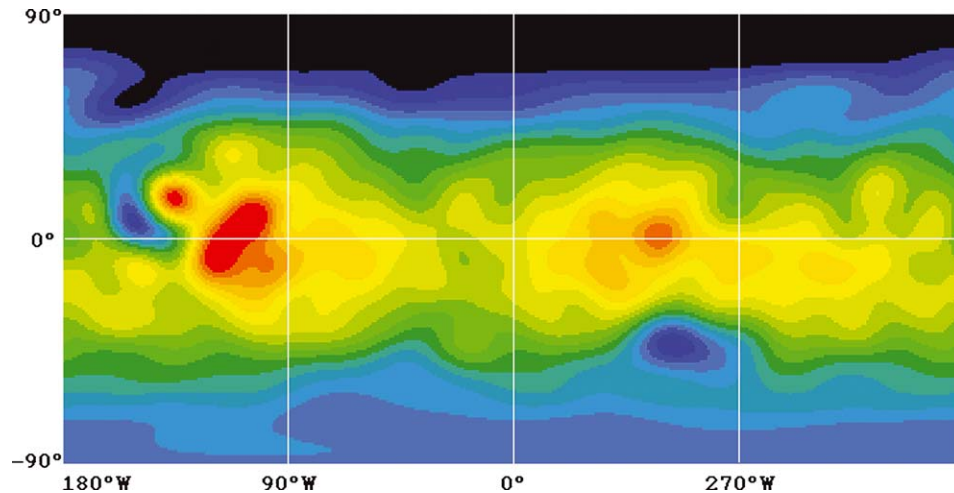


Figure 5. Spherical harmonics shape model of degree and order 16 for Mars. Parameters of this function were determined as the best fits to 3739 three-dimensional control point coordinates, obtained by photogrammetric analysis of Viking Orbiter images (Zeitler and Oberst, 1998b). Elevations with respect to a best-fit sphere range from  $-17$  km (black) to  $+21$  km (red). Similar global shape models will be obtained for the satellites of Saturn.

of the control points, pointing data for each image involved, and possibly, rotational parameters of the satellite as well. Assuming that at least 10 images with global coverage and surface resolutions of  $3\text{--}5$  km/pixel are available, three-dimensional coordinates for several hundreds of control points will be determined with precisions of one standard deviation equal to  $1\text{--}3$  km (Oberst *et al.*, 1998; Oberst and Schuster, 2004). The precision will increase as more images or images at higher resolution are available. The radius components of the control points may be used to study the global shape of the satellite, as has recently been demonstrated for Mars (Figure 5) and for Galileo control points on Io (Oberst and Schuster, 2004).

Librations are a minor uncertainty in these solutions, except for Hyperion where the departure from synchronous rotation is extreme, and possibly Enceladus (see Section 2.1.1.3). Detection of libration, which is a necessary part of the overall geodetic process, is accomplished by measuring the rotational position of landmarks on the surface in comparison to predicted rotational models, such as simple synchronous. Its success depends upon accurate stereogrammetric measurements of parts of the satellite's surface at two different points in the orbit relative to periapse.

**2.1.1.2. Topography.** Virtually all studies of geological processes require knowledge of surface topography. Topographic mapping can be carried out using stereo image analysis and "shape-from-shading" modeling.

**Stereo imaging:** Stereo image analysis will be carried out in different stages. First, as described above, control point measurements and block adjustment

techniques are used to improve the nominal pointing of the images. Next, “digital image matching” is carried out to find large numbers ( $>10,000$ ) of conjugate points in image pairs. Object coordinates (latitude, longitude, radius) of these points are computed from the improved camera pointing data. Interpolation in between these points is used to form a contiguous grid. Points from several stereo pairs can be combined to form terrain mosaics covering large areas.

The accuracies of the control point coordinates depend on lighting conditions and the specifics of the imaging geometry. For single points of interest, precisions of object coordinates on the order of one pixel can be obtained if stereo images have reasonable convergence (stereo) angles, near  $20^\circ$ . However, terrain models of large, contiguous areas typically have reliable spatial scales of three to five times larger than the image pixel size: i.e., a map resolution three to five times lower than the inherent image resolution. Coordinates are difficult to reference to absolute heights if no additional data (e.g. extra images) are available. However, relative elevation information is generally sufficient to support geological studies of the terrain.

The methods for analysis have been developed and applied using Galileo images of the Moon obtained during the Earth – Moon flyby in 1992 (Oberst *et al.*, 1997) (Figure 6) and during encounters with Ganymede and Europa (Giese *et al.*, 1998; Oberst *et al.*, 1998). However, owing to the low data rate of the Galileo spacecraft

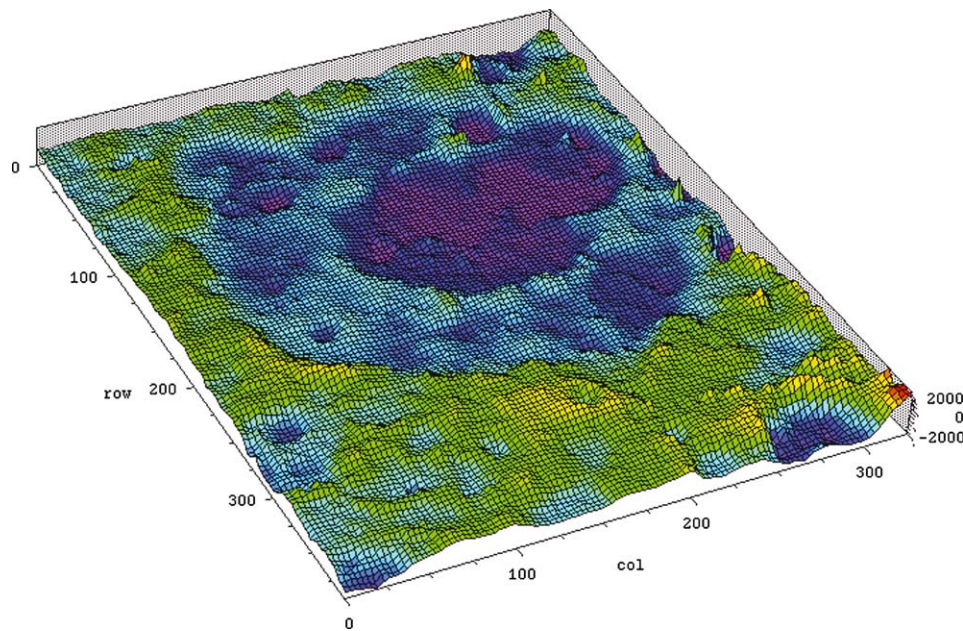


Figure 6. Digital Terrain Model of the 600 km diameter Lunar Humboldtianum Basin, derived from Galileo ( $\sim 1$  km/pixel) stereo images of the Moon obtained during the second Earth–Moon flyby in December 1992. Terrain models of this type will be obtained for selected regions on the Saturnian satellites.

at Jupiter, only a small number of stereo images were returned. We expect better results from Cassini.

*Shape-from-shading (or photoclinometry):* In this technique, which is used when stereo is not available and/or the highest possible resolution is needed, surface slopes are determined from the apparent brightness of the image. However, the photometric function (the function that describes the variation of surface brightness with illumination and viewing angles) must be known. One-dimension profiles and two-dimension grids of relative heights can be obtained by integration. The chief limitations on this technique can be the lack of knowledge of the albedo variations and photometric function across the surface. These conditions are frequently not met – in fact, the technique may be impossible on Titan due to atmospheric scattering that washes out topographic shading – but a uniformly bright satellite like Enceladus may be ideal. Photoclinometry has successfully been applied to various planetary surfaces (Figueredo *et al.*, 2002; Schenk *et al.*, 2004). Terrain models for asteroid Ida, derived from shape-from-shading and stereo image analysis show good agreement (Giese *et al.*, 1996).

*2.1.1.3. Geophysics and Internal Structure.* Important geophysical parameters such as rotational moments of inertia may be inferred from the shapes and masses of relaxed ellipsoidal satellites, and from observations of amplitudes of librations, all of which can be derived from imaging observations. The mass distribution within a satellite, inferred from the moment of inertia, can help refine interior models that constrain the composition of the originally accreted materials as well as define past and present differentiation of those materials. The primary parameter sought is the moment of inertia factor,  $C = I/MR^2$  ( $I$  is the rotational moment of inertia;  $M$  the mass,  $R$  the mean radius;  $C = 0.4$  for homogeneous sphere). The moment factor is detected with imaging by measurement of the satellite's shape parameter,  $(a-c)/R$ , where  $a$  and  $c$  are the long and short ellipsoidal axes. The  $(a-c)$  for a satellite is proportional to  $H_m$ , where  $H$  is the measure of the internal mass distribution relatable to  $C$ , and  $m$  is inversely proportional to mean density and directly proportional to rotational speed. Thus, the low density ( $<2.0$  g/cm<sup>3</sup>) and high rotational frequency of many of the Saturnian satellites means they have relatively large shape parameters,  $(a-c)/R$ , even with differentiation ( $H < 1$ ). Measurement of the shape is done with full-disk imaging, capturing the limbs. These data can be obtained with a CCD to a precision of about 0.1–0.15 pixels, so images a few hundred pixels in diameter can be measured to levels that allow useful resolution of the  $(a-c)$  values. Appropriate spacecraft satellite (NAC) imaging ranges vary between 75,000 km for Mimas and 285,000 km for Rhea – often achievable during the Cassini orbital tour – with discrimination of  $C$  likely to be better than 7% for Rhea and 1% for Mimas and Enceladus.

Limb profiles provide the most direct route to overall characterization of an ellipsoidal shape of a satellite. For restricted sections of a large satellite, or for the entire shape of smaller, irregularly shaped ones, the stereoscopic geodetic measurements

of control points provide the basic data and can be used in conjunction with limb measurements for testing high-order departures from ellipsoidal shapes (see Section 2.1.1.1). Best-fit ellipsoid parameters determined from a grid of control points, or local elevation models can address many geophysical issues (Zeitler and Oberst, 1998; Oberst and Schuster, 2004).

Moments of inertia can also be constrained by measurements of a satellite's forced libration, if the libration is large enough to be measured. The strongest result will be for Mimas, where the predicted libration amplitude of about  $0.5^\circ$  is 1.7 km on the equator (Dermott and Thomas, 1988), a quantity that should be easily observed in the planned imaging sequences. And Enceladus presents a special case in which a measure of its libration, if present, holds great significance for its internal structure and interpretation of the tectonic features seen on its surface (see below). However, in most other cases, it is more likely that the shapes will provide more accurate estimates of moments of inertia.

How might the satellites have reached different stages of differentiation? Accretional heat is believed to have been important very early in the satellites' history (Ellsworth and Schubert, 1983; Federico and Lanciano, 1983; Squyres *et al.*, 1988). Accretion for these satellites has been modeled to be quite rapid (Safronov, 1972; Safronov and Ruskol, 1977; Safronov *et al.*, 1986), and impactor kinetic energy is largely deposited as heat at and below a satellite's surface. At the end of accretion, a satellite's temperature profile is cool at the center, rises to a maximum several tens of kilometers below the surface, and drops sharply at the surface. The maximum temperature can approach or exceed the  $\text{NH}_3\text{--H}_2\text{O}$  eutectic temperature for Tethys, Dione, and Rhea even if the satellites accreted in a gas-free environment, and also for Mimas and Enceladus if a warm nebula was present (Squyres *et al.*, 1988). Following accretion then, some satellites will have had a region of relatively warm, mobile, and buoyant material a few tens of kilometers beneath the surface. An exception is Iapetus, which accretes more slowly, and is able to radiate its accretional heat effectively (Squyres *et al.*, 1988).

Continued evolution takes place by radiation, warming by radionuclides, and heat transport by conduction and (in some cases) convection. Rapid post-accretion cooling of the outer layers can produce extensional thermal stresses as large as  $\sim 200$  bars, even accounting for a viscoelastic crust (Hillier and Squyres, 1989). Such stresses should cause failure, producing extensional tectonism and perhaps enabling extrusion of buoyant subsurface materials. Deep warming can cause further extension (Ellsworth and Schubert, 1983). The magnitude of warming is limited by solid-state convection which removes heat rapidly. For Rhea and Iapetus, which can contain ice II (and for Iapetus only if it is largely undifferentiated), warming can also cause expansion via the ice II–ice I phase change. As heating diminishes and heat loss by conduction becomes dominant, the satellites cool and contract, albeit at a rate slow enough that tectonism may not result.

There are some hints on internal structures from Voyager data. The shape of Mimas is consistent with a central increase in density if the surface is in hydrostatic



equilibrium (Dermott and Thomas, 1988). However, this observation might also imply a silicate core, an increase with depth in the compaction of rubble, or just a rigid, non-hydrostatic surface layer (Ross and Schubert, 1988). On Tethys, if Ithaca Chasma is the result of relaxation of Odysseus, the flow implied places an upper limit on the size of its core of  $\sim 20\%$  of the satellite's radius (Thomas and Squyres, 1988). The shape of Enceladus, combined with reasonable assumptions on possible materials, suggests a denser core within a deep water ice mantle (Dermott and Thomas, 1994).

Enceladus is unusual in two important ways. A 2:1 orbital resonance with Dione forces its eccentricity and produces some degree of tidal heating (Yoder, 1979; Squyres *et al.*, 1983; Ross and Schubert, 1989). A simple model suggests that the present eccentricity is several times too small to maintain a partially molten interior if the thermal conductivity of the crust is that of solid ice, but perhaps sufficient if a low-conductivity regolith is present (Squyres *et al.*, 1983). A more sophisticated treatment using a viscoelastic rheology suggests that melting is somewhat more likely (Ross and Schubert, 1989), though there is still the question of why Enceladus would have melted due to this mechanism and not similarly-sized Mimas.

Also, it has been recently shown that Enceladus may be in a 3:1 secondary spin-orbit resonance capable of increasing its tidal heating over previous estimates by 100- to 1000-fold, depending on physical parameters like the rigidity of ice and the moon's oblateness (Wisdom, 2004). If Enceladus is indeed in this resonance, the model predicts a large forced libration amplitude – up to  $10^\circ$ – $20^\circ$ –which would be easily measured in Cassini images and would suggest a degree of tidal heating possibly large enough to produce a subsurface liquid mantle and hence present-day geologic activity on Enceladus. The implications for surface expressions such as geysers, chaotic 'ice flow' terrain as seen on Europa, and other morphological indicators are obvious. Enceladus could be the Europa of the Saturn system.

Hyperion's chaotic rotation presents challenges in observation and modeling. Imaging at ranges less than  $10^6$  km is sufficient to refine the shape and track rotation. Indications from Voyager data are that much of the time the rotation consists of two components that can remain fairly uniform for long periods. The combination of the close flyby imaging for geology, mass, and other compositional information, combined with rotational monitoring, should allow for excellent modeling of variations in density distribution and overall geologic history, better than for any other irregularly shaped icy object.

*2.1.1.4. Surface Processes: Resurfacing and Tectonism.* Voyager results indicate that resurfacing has occurred on several Saturnian satellites, but the mechanisms are not obvious due to the lack of very-high-resolution images of these bodies. Resurfacing is expected to occur by volcanic or "cryovolcanic" extrusion of material from below, by impacts, or by faulting and fracturing of the surface by tectonic stresses. Water (H<sub>2</sub>O)-rich material was probably extruded to the surface of these bodies, but it is not known if it was liquid, slush, or solid ice. Predominantly



liquid resurfacing is favored on theoretical grounds (Stevenson, 1982; Squyres and Croft, 1986). However, ice is difficult to melt in such small, cold satellites. Moreover, liquid water is denser than ice, so achieving melt buoyancy is difficult if the satellites have silicate-poor outer regions. Ammonia ( $\text{NH}_3$ ), which is cosmochemically plausible (Lewis, 1972; Prinn and Fegley, 1981), could help on both counts (Stevenson, 1982; Squyres *et al.*, 1983; Ellsworth and Schubert, 1983), since it lowers the melting point by 100 K, and leads to eutectic melt that is less dense than pure  $\text{H}_2\text{O}$  liquid (Croft *et al.*, 1988).

The Voyager images are inconclusive on the matter of cryo-volcanism. No lobate flow fronts are observed at Voyager resolution. This situation probably rules out solid-state flow, since plausible ice rheology should lead to thick, and therefore Voyager-observable, flows on these satellites (Jankowski and Squyres, 1988; Schenk, 1989), as seen on the Uranian moon Ariel. However, slush, which may have something like a Bingham rheology (Melosh and Janes, 1989; Schenk, 1989; Thomas and Squyres, 1989), may have properties (Kargel and Croft, 1989) such that a significant solid fraction could still yield flows too thin to be seen at Voyager resolution. (Bingham fluids have yield strengths which are independent of viscosity, and so flow characteristics – thick or thin – are not solely determined by viscosity.) High-resolution images of resurfaced (sparsely cratered) regions will place better limits on flow rheology.

Recent resurfacing on Enceladus may be indicated by its high, nearly uniform albedo (Smith *et al.*, 1981, 1982; Buratti, 1984, 1988) that ignores geological boundaries. Its physical association with Saturn's E ring (Baum *et al.*, 1981; Larson *et al.*, 1981; Pang, 1984), which consists of small particles of short lifetimes ( $10^2$ – $10^4$  years; Morfill *et al.*, 1983; Haff *et al.*, 1983; Burns, 1984) suggests Enceladus as the source of the E ring, and one possible mechanism is liquid-rich resurfacing events. Alternatively, Hamilton and Burns (1994) concluded that the ring may be self-sustaining, with meteoroid impacts on Enceladus as the originator of ring particles. High-resolution images may refute this model if small craters are rare, as seen on the Galilean satellites (Bierhaus *et al.*, 2001). Also, cryo-volcanism cannot be ruled out as a source for some ring particles and for the uniform albedo since volcanic constructs have been interpreted on its surface (Schenk and Moore, 1995).

Evidence for tectonic activity on the Saturnian satellites generally takes the form of troughs or grooves that may represent graben or other faulting, generally of an extensional nature. Evidence of compressional features on the icy Saturnian satellites is sparse from Voyager images. Investigating the tectonics on these bodies requires global mapping of fault patterns and determination of the geometry of the surface expressions of these patterns in order to work out the nature and history of events recorded in the tectonic features. Low-sun imaging to reveal very low-amplitude folding as seen on Europa (Proctor and Pappalardo, 2003) is also needed.

Enceladus shows widespread evidence for tectonism (Smith *et al.*, 1981, 1982; Squyres, 1983; Kargel and Pozio, 1996; Gomez *et al.*, 1996). While the boundaries of some resurfaced regions are diffuse, there is one band of resurfaced terrain with

sharp margins cutting through cratered terrain (Figure 7). This relationship may indicate that a structural rift has been filled with extruded material, but the contact has not been characterized in detail. Grooves concentrated within resurfaced regions are a few kilometers wide, a few hundred meters deep, and in some cases more than 100 km long. Their geometry correlates with the apparent age (crater density) of

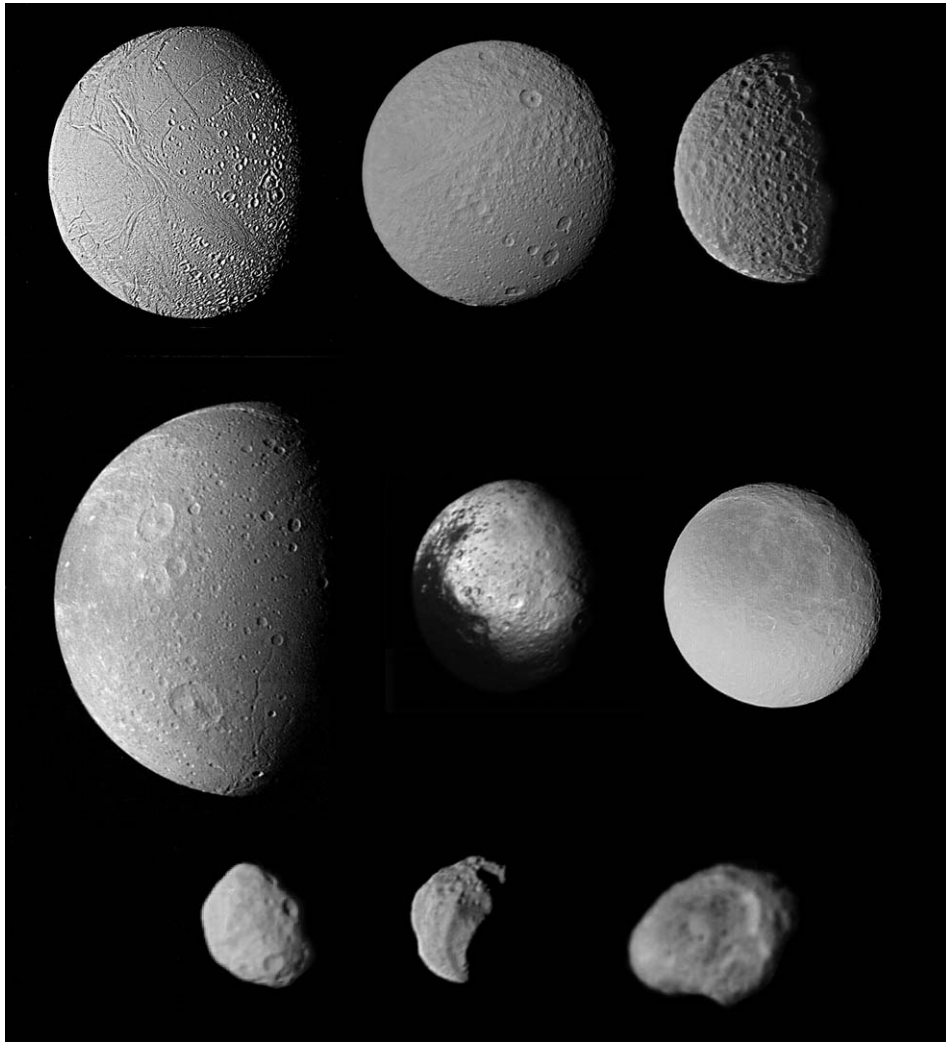


*Figure 7.* Voyager global images of icy satellites of Saturn, not to scale. Left to right, top to bottom: Enceladus: linear tectonic features, craters with variable morphology are visible. Tethys: linear marking from middle left to upper right is part of Ithaca Chasma. Mimas: non-circular outline is real: this high latitude view shows the 10% elongation due to rotational and tidal effects. Dione: bright markings, craters, and sinuous troughs. Iapetus: greatly varying albedo pattern. Rhea: heavily cratered. Janus: irregular shape and shallow craters. Epimetheus: heavily cratered and a ring shadow. Hyperion: scalloped topography suggests spallation of large amounts of material.

the terrain: in the youngest terrains, grooves are common and occur in curvilinear sub-parallel sets; in older terrains they tend to be straighter and to occur singly. The oldest terrains generally lack grooves. The details of groove morphology are poorly known, and their underlying structural nature is an open question. They may be grabens, modified extension fractures, or ductile necking features.

Several other Saturnian satellites show evidence of tectonism (Smith *et al.*, 1981, 1982; Plescia, 1983; Moore and A'Hearn, 1983; Moore, 1984; Moore *et al.*, 1985; Thomas, 1988; Gomez *et al.*, 1996; Kargel and Pozio, 1996). Mimas, Tethys, Dione, and Rhea all have narrow, shallow troughs on their surfaces. The troughs' origins are unknown. Mimas has a series of topographic troughs which show no clear association either to the largest impact crater, Herschel, or to tidal stress orientations. The surface of Tethys is also cut by an enormous trough, Ithaca Chasma (Figure 7), that extends at least 270° around the satellite. It is up to 100 km wide and perhaps ~3 km deep. The walls show evidence of complex structure, including internal terraces and grooves. Ithaca Chasma may be a large graben. It roughly traces a rough great circle across Tethys, and the large crater Odysseus lies at one pole of this great circle, suggesting a genetic link (Smith *et al.*, 1982; Moore and A'Hearn, 1983; McKinnon, 1985; Thomas and Squyres, 1988).

Dione has a few very subdued ridges that may be compressional (Moore, 1984). They are at most a few hundred kilometer long, and have very gentle slopes and low relief. They are only visible near the terminator in Voyager 1 images (Moore, 1984), so their global distribution, like their topography, is unknown.

*2.1.1.5. Crater Studies. Geomorphology.* Impact craters are ubiquitous geologic features throughout the solar system and the Saturnian satellites are no exception (Smith *et al.*, 1981, 1982). The study of craters is vital for determining material properties as well as establishing the chronology of geologic events in the satellites' histories. Crater depths are poorly determined on the basis of Voyager images, but simple craters appear to be a few tens of percent shallower than those of equivalent size on silicate bodies (Schenk, 1989). This observation may reflect a difference in the strength properties of icy material, but is not well understood. Ejecta deposits are difficult to identify in the Voyager images of the Saturnian moons. Secondary crater fields have not yet been identified but must be present. The diameter of the transition from simple to complex craters seems to scale roughly with gravity among the satellites, but there are deviations from this trend (Chapman and McKinnon, 1986; Schenk, 1989). The transition takes place at a diameter far smaller than expected by extrapolation from silicate bodies, and may indicate lower cohesion for icy materials.

Observations of large craters are severely hampered by inadequate Voyager coverage, resolution, and viewing geometry. Multi-ringed structures should form most readily on high-gravity bodies, and the clearest multi-ringed structure in the Saturn system is indeed on the second largest satellite: Tirawa, on Rhea, with a diameter of 350 km. (The presence or absence of impact basins on Titan is

presently unknown.) Tirawa lies on the terminator in Voyager images, however, so its morphology is poorly known. There may be another multi-ring structure on Rhea, seen on the limb at very low resolution by Voyager (Moore *et al.*, 1985). The largest known crater in the Saturn system is Odysseus, on Tethys, with a diameter of 430 km. It seems to have a complex central peak structure, but no clear rings.

Craters with polygonal rims are observed, and are common on Rhea (Smith *et al.*, 1981). The shapes probably indicate exploitation of trends of structural weakness during excavation (Shoemaker, 1960). Rim segments on some areas of Rhea show preferred orientations (Moore *et al.*, 1985; Thomas, 1988). This observation probably reflects an underlying structural stress pattern, but the pattern's global nature is not known.

Viscous relaxation of craters in the Saturn system appears rare, apparently due to the low gravity and cold temperatures of the satellites. Exceptions seem to be the large craters Tirawa and Odysseus (Schenk, 1989), although their degree of relaxation is poorly known. Relatively small craters on Enceladus also appear to be relaxed (Passey, 1985), probably because that satellite has undergone tidal warming. The morphology of craters on Enceladus could enable estimation of depth to a possible liquid water mantle, as has been possible on Europa (Turtle and Pierazzo, 2001; Schenk, 2003).

*Impact history:* The cratering records of the satellites are diverse (Smith *et al.*, 1981, 1982; Strom, 1981; Plescia and Boyce, 1982, 1983, 1985; Hartmann, 1984; Neukum, 1985; Lissauer *et al.*, 1988). Crater density variations are largest on Enceladus, where some areas are nearly as cratered as any in the Saturn system, and others show no craters at the best Voyager resolution. Only an upper limit may be placed on the age of the most recent resurfacing on Enceladus, due to the lack of information about the density of unresolved craters in the youngest areas. Tethys and Dione are generally more cratered than Enceladus, with a smaller variation in ages. Nevertheless, there is clear evidence on Dione and good evidence on Tethys for local resurfacing. The global pattern of resurfacing on all three satellites is poorly known due to coverage limitations. The most densely cratered surfaces on some of the moons, e.g. Mimas, might date back to a period of heavy post-accretional bombardment (Neukum, 1985).

On Mimas and Rhea the distribution of large craters is also spatially inhomogeneous (Smith *et al.*, 1981; Plescia and Boyce, 1982). However, statistical analyses (albeit based on limited numbers of craters) suggest that this degree of inhomogeneity is expected from spatially random cratering (Lissauer *et al.*, 1988). More complete coverage of the satellites' surfaces is needed to confirm this conclusion. Some areas on Rhea also show an apparent shortage of small craters (Plescia and Boyce, 1982) – an observation that could indicate local surface mantling or a paucity of small comets in the outer solar system (Zahnle *et al.*, 2003). However, there is a correlation of small crater density with illumination geometry (small craters appear scarcest where the sun is overhead (Lissauer *et al.*, 1988), so the observation is

inconclusive. Images with different illumination geometries and higher resolution are needed.

The crater density on Iapetus is large (Smith *et al.*, 1982; Plescia and Boyce, 1983; Lissauer *et al.*, 1988), but poorly known due to Voyager resolution limitations: the highest resolution Voyager image had a scale of 8.5 km/pixel. Craters on Iapetus are mainly observed in bright terrain. Only recently were craters also detected and counted in Voyager images of the northwestern edge of the dark terrain under photometrically favorable (low-sun) conditions (Denk *et al.*, 2000), indicating that the crater size – frequency distribution is similar in the measured parts of the dark and bright terrain. Interestingly, Rhea and Mimas, which lie deeper in Saturn’s gravity than Iapetus, appear to have crater densities lower than that of Iapetus by a factor of about 1.5 (Smith *et al.*, 1981, 1982; Plescia and Boyce, 1982, 1983; Lissauer *et al.*, 1988). Either Iapetus preserves a record of impacts by planetocentric debris that did not cross Rhea’s orbit (unlikely according to Zahnle *et al.*, 2003), or the surfaces of Mimas and Rhea are younger than that of Iapetus. We can potentially use the density of craters on Iapetus to calculate the probability that the other satellites have been collisionally disrupted since formation of Iapetus’ surface. One such calculation suggests multiple disruptions and reaccretions of most satellites inside Rhea (Smith *et al.*, 1982). Another hypothesis suggests that disruption is only probable for the small satellites – Atlas, Prometheus, Pandora, Janus, Telesto, and Calypso – whose irregular shapes suggest they are collisional remnants (Lissauer *et al.*, 1988).

Old surfaces in the system have, in general, less “steep” crater size – frequency distributions than young ones (Smith *et al.*, 1981, 1982; Plescia and Boyce, 1982; Lissauer *et al.*, 1988). A “steep” distribution indicates a rapid increase in the cumulative number of craters larger than a given diameter as that diameter decreases. One interpretation is that there were two impactor populations: an early Population I, with a “normal” amount of large impactors, and a later Population II with fewer large impactors (Smith *et al.*, 1981, 1982). In this scenario, young regions were cratered primarily by Population II. Another interpretation is that there was a single “steep” impactor population. Under this interpretation, young surfaces retain the shape of the production distribution, while old surfaces have had their curves “flattened” at large diameters by saturation-equilibrium effects. For the Galilean satellites, the high-resolution image data returned by the SSI camera onboard the Galileo Orbiter has not resolved this issue (Neukum, 1997; Neukum *et al.*, 1998; Chapman *et al.*, 1998; Zahnle *et al.*, 2003; Schenk *et al.*, 2004). Neukum (1985) and Wagner and Neukum (1996) found similarities between crater distributions in the inner solar system, the Galilean satellites of Jupiter, and the satellites of Saturn. This similarity, if real, suggests a similar projectile population, derived from collisionally evolved bodies, such as Main Belt asteroids, and a lunar-like impact cratering scenario with (1) a heavy bombardment period prior to about 3.3 Gyr and (2) a constant cratering rate ever since (Neukum, 1997; Neukum *et al.*, 1998).

Other investigators (Zahnle *et al.*, 1998, 2003; Schenk *et al.*, 2004; Chapman *et al.*, 1998; Bierhaus *et al.*, 2001), have presented evidence that comets play the

major role in impacting the jovian satellites. Zahnle *et al.* (1998, 2003) summarize observations and calculations showing that comets dominate the present-day cratering in the outer solar system. They note that while there is a paucity of small primary impacts on the Galilean satellites (Chapman *et al.*, 1998; Bierhaus *et al.*, 2001; Schenk *et al.*, 2004), the small craters on Triton, if primary rather than secondary craters, imply a population rich in small bodies. Small craters on Triton may be of heliocentric or planetocentric origin. Zahnle and colleagues considered two cases for Saturn, one in which the size – frequency distribution is like that at Jupiter, and the second in which small objects obey a collisional distribution. Resulting surface ages for the Saturnian moons are much younger in the second case. For example, average surface ages for Tethys, Dione, and Rhea may be as young as 1 Gyr or as old as 4 Gyr. Iapetus should have experienced little planeocentric cratering and must be very old.

Both global coverage and high-resolution images of the Saturnian satellites will help to extend the database of crater distributions at all sizes to another satellite system, crucial to interpreting the cratering record of these bodies and others in the outer solar system.

#### 2.1.2. Spectrophotometry

Multi-spectral imaging is a powerful tool for understanding the relationships between satellite compositions, geology, and surface modification processes, both endogenic and exogenic. In general, multi-spectral imaging can be used to attempt the difficult task of specific compositional identifications or to identify color units that have specific geologic associations. In particular, the nature and origin of the dark material in the Saturn satellite system, which as a collection of bodies is unusually bright, is of special interest (Owen *et al.*, 2001), both because dark material is rare in the Saturnian system and because of the inferred presence of organics on Iapetus and Titan. Variations in the scattering of light as a function of viewing and illumination geometry may also provide information on surface texture that can be associated with either local geology or with patterns expected from exogenic effects.

The geometric albedoes of many of the satellites are very high: the inner five major satellites, Mimas, Enceladus, Tethys, Dione, and Rhea, all have albedoes as high as, or higher than, the brightest icy satellite of Jupiter, Europa. Enceladus is extraordinarily bright, with a geometric albedo of  $\sim 1.0$  (Smith *et al.*, 1981; Buratti and Veverka, 1984; Buratti, 1988). There is little variability of albedo, and essentially no correlation of albedo with underlying geology. These observations are consistent with recent deposition of surface frost. Most of the other satellites are also bright, with Bond albedos of 0.45–0.6, and phase integrals of 0.7–0.9 (Buratti and Veverka, 1984).

Dione and Rhea both have bright leading and darker trailing hemispheres (Noland *et al.*, 1974; Franz and Millis, 1975; Smith *et al.*, 1981, 1982; Buratti and Veverka, 1984), and Rhea's normal reflectance is strikingly bimodal (Verbiscer and

Veverka, 1989). Tethys has a broad, darker north – south “stripe,” observed only at very low resolution, centered on its trailing hemisphere (Smith *et al.*, 1981; Buratti and Veverka, 1984). Dione and Rhea also have bright “wispy” markings transecting their trailing hemispheres (Smith *et al.*, 1981, 1982), and on part of Dione these appear to correlate roughly with some poorly observed tectonic features. However, the wispy markings have not been observed with favorable geometry or resolution, and their origin is unknown.

Current knowledge of the spectral properties of the major icy Saturnian satellites comes from a combination of ground-based telescopic and Voyager data. Telescopic near-infrared spectra ( $\sim 1\text{--}3.5\ \mu\text{m}$ ) show that essentially all of these objects are rich in water ice or frost on their surfaces (Johnson *et al.*, 1975). Color data from ultraviolet to near-infrared wavelengths ( $\sim 0.35\text{--}1.0\ \mu\text{m}$ ) give evidence for varying amounts of non-water ice constituents mixed with the ices and frosts on the surface (McCord *et al.*, 1971; Noland *et al.*, 1974; Morrison *et al.*, 1984; Cruikshank *et al.*, 1984; Cruikshank, 1981, 1999). (The low mean densities of the satellites for which we have mass estimates are consistent with a dominance of water ice. Densities of about  $1.0\text{--}1.5\ \text{g/cm}^3$  suggest that the satellites overall are predominately ice mixed with tens of percent of non-ice material: i.e., rock plus carbonaceous material.)

The satellites also have relatively bland colors in the visible and ultraviolet and are redder than expected for pure ice models but much less so than the Galilean satellites (McCord *et al.*, 1971; Noland *et al.*, 1974; Smith, *et al.*, 1981; Buratti *et al.*, 1990). (Interestingly, the ring colors are significantly redder than the inner satellites and comparable to the Galilean satellites (Lebofsky, *et al.*, 1971; Smith, *et al.*, 1981) in spite of also being primarily pure water ice.) Buratti *et al.* (1990) found broad-scale patterns of spectral variation without a high degree of correlation to geologic structures. The major exception is the so-called “wispy” terrain which appears as a distinct “bluish” unit, possibly indicating that it is a deposit of fresher frost of some type. The dark material on Iapetus is both dark and red, and it has been suggested that this material is similar to very dark red asteroids (so-called D-class) and to complex organic material produced in laboratory experiments (“Tholins” – Bell *et al.*, 1985; Wilson and Sagan, 1995). Hyperion, inward of Iapetus, appears to also be abnormally red, while Phoebe, probably a captured object, is representative of another class of dark, more spectrally neutral material.

Among the observational goals of the Cassini ISS team will be searching for spectral correlations with geologic units at high resolution. Spectral imaging of the Galilean satellites by Galileo has demonstrated the utility of such studies, and Cassini ISS has many more spectral bandpasses. On Jupiter’s satellite Europa, for instance, the near-infrared range of the CCD allows the separation of units with differing ice particle sizes that led to the discovery of “IR-bright” units not visible at shorter wavelengths; these results allowed the relative ages of the surface units to be determined (Geissler *et al.*, 1998). Comparisons of visible and near-infrared spectral units with those seen at longer wavelength by NIMS (whose improved Cassini counterpart is VIMS) have proven vital to understanding the geologic setting

of non-ice materials identified as hydrated salts by the NIMS experiment. Galileo found that dark, non-ice materials are concentrated in low areas on Europa and Ganymede (Oberst *et al.*, 1999).

Exogenic modification may mask local variations in composition or texture. Concentration of non-ice material by preferential removal of volatiles through evaporation, impact or sputtering has been considered as an important process, but its relative importance compared with collection of material from infalling meteoritic and ring material is unknown at present. The ambiguity concerning the origin of the unusually uniform spectral and photometric properties of Enceladus, mentioned in Section 2.1.1.3, is an example. Exogenic modification by the E ring on several other satellites besides Enceladus is suggested by near-IR photometry (Buratti *et al.*, 1998). Additionally, the hemispheric dichotomies exhibited by some of the other satellites has been suggested as arising from preferential bombardment of the leading sides of the satellites by cometary and meteoritic material (see Buratti *et al.*, 1990). The effects of radiation on the surface materials is another potential source of spectral modification. The identification of O<sub>3</sub> on Dione and Rhea (Noll *et al.*, 1996), probably in gas inclusions in the surface ices, is a piece of evidence suggesting radiation modification of the near surface.

Iapetus has perhaps the strangest photometric properties in the solar system. At low Voyager resolutions, the color properties across the hemispheres appear to vary as a smooth mixture of ice with the dark red material (Buratti and Mosher, 1995), but there are also hints that at high resolution, material might be very localized. Normal reflectance ranges from  $\sim 0.03$  near the apex of orbital motion to  $\sim 0.6$  near the poles (Squyres and Sagan, 1983; Goguen *et al.*, 1983; Squyres *et al.*, 1984). The dark material is reddish in color (Cruikshank *et al.*, 1983; Squyres *et al.*, 1984). The albedo pattern is symmetric about the apex, and photometric contours nearly parallel calculated impact flux contours. Along the boundary between bright and dark terrain there is evidence for topographic control of albedo, including dark-floored craters and bright slopes facing toward the antapex. Evaluation of the spectrum of dark components on Iapetus and Hyperion suggest similar materials on both bodies (Jarvis *et al.*, 2000).

Hypotheses proposed to explain the pattern of Iapetus' albedo (Cook and Franklin, 1970; Soter, 1974; Smith *et al.*, 1982; Squyres and Sagan, 1983; Bell *et al.*, 1985) include coating of the leading hemisphere with debris from Phoebe, and volcanic eruption or exposure by impact erosion of dark material indigenous to Iapetus. A case can be made that the varying impact flux has influenced the albedo pattern, but present poor resolution and signal-to-noise ratio make it impossible to evaluate confidently the relative roles of endogenic and exogenic processes. While debris from Phoebe (which is in a retrograde orbit) may add to the asymmetric impactor flux, it is unlikely that coating of Iapetus' surface with this material is the answer. Phoebe has a low normal reflectance of  $\sim 0.05$  (Simonelli *et al.*, 2000), but is spectrally neutral except for a slope in the  $0.3\text{--}0.4\text{ }\mu\text{m}$  range (Degawij *et al.*, 1980; Tholen and Zellner, 1983; Thomas *et al.*, 1983a) and a turndown from 0.9



to  $1.1\ \mu\text{m}$  (Tholen and Zellner, 1983). It shows some spatial variations in albedo, though little is known of their detail or origin, or about spatial variations in color.

Description of the satellites' photometric properties is limited by phase-angle coverage, which is spotty and in only a few cases extends past  $70^\circ$ . The fitting of Hapke's photometric function (Hapke, 1981, 1984, 1986) suggests high single-scattering albedos, regolith compaction similar to Moon's, and particle phase functions somewhat more backscattering than Moon's (Buratti, 1985). Estimation of surface roughness is virtually precluded by a shortage of high phase angle data.

### 2.1.3. *Determination and Refinement of Satellite Orbits and Masses*

Before the advent of spacecraft flybys, ground-based astrometric observations of orbital variations were the only means of determining satellite masses. Doppler tracking of the Cassini spacecraft during close satellite flybys will yield mass determinations for some of the satellites, but detailed analysis of satellite orbits and their variation over the Cassini tour from ISS images will be an invaluable complement. In addition to the mutual perturbations of all the satellites, there are three resonant relationships in the Saturnian satellite system that induce significant orbital variation between pairs of satellites: (i) Mimas and Tethys are involved in 2:1 resonance that modulates the inclination of both satellites; (ii) Enceladus and Dione are locked in a 2:1 resonance which leads to a significant forced component on the eccentricity of each satellite; and (iii) the 4:3 resonance between Titan and Hyperion has no effect on Titan but causes a large forced eccentricity (0.1042) on Hyperion. These resonant relationships are important because they can be used to determine the masses of some of the satellites involved.

Detailed knowledge of the orbits of the satellites and their variation derived from ISS observations is essential for the success of the Cassini mission. This is because the optical navigation of the spacecraft utilizes ISS images of distant satellites against the background stars to determine the position of the spacecraft. Such images are also used, in turn, to improve the orbits of the satellites and thereby help in targeting close flybys. The best ground-based astrometric observations of Saturn's larger satellites (such as Titan, Rhea, Tethys and Dione) have 1-sigma residuals of  $\sim 0.08$  arcsec, corresponding to positional errors of  $\sim 500$  km. For the smaller satellites (such as Mimas, Enceladus and Iapetus) the errors are  $\sim 1200$  km. Because Phoebe is so distant it is difficult to obtain plates or CCD frames of it with other satellites and so its positional error is currently  $\sim 6000$  km. The limits of ground-based astrometry will be overcome and the positional errors reduced by using the Cassini ISS data as they become available throughout the mission. Therefore, one of the end products of the mission will be sets of orbital elements for the satellites that can be used as starting values for long-term numerical simulations of the dynamical evolution of the system.

Accurate orbit determinations of the Trojan satellites can be used as independent checks on the masses of Tethys and Dione, and indeed any satellite that is found to have a co-orbital companion. This is because for small amplitude librations about

the equilibrium points,  $T \propto (M/m)^{1/2}$ , where  $T$  is the period of libration of the Trojan satellite,  $m$  the mass of the parent satellite and  $M$  the mass of Saturn. For Tethys and Dione the respective libration periods of their Trojan should be close to 660 and 775 days, respectively; Cassini should be able to observe several libration cycles.

The Janus and Epimetheus pair is unique in the solar system. Both satellites are in near-circular, near-equatorial orbits with an orbital separation of 50 km, which is less than or comparable to the smallest physical dimension of either object. However, rather than collide, a study of the three-body problem shows that although they come close to one another every 4 years, they cannot pass even though they affect each other's orbits. The resulting configuration is called a horseshoe orbit. At closest approach, the radial displacements of each satellite ( $\pm 10$  and  $\pm 40$  km from the mean semi-major axis for Janus and Epimetheus, respectively) are functions of their mass ratio and their separation in longitude is a function of the sum of their masses (Yoder *et al.*, 1983). Given that the Voyager spacecraft obtained resolved images of both Janus and Epimetheus, their volumes are known and astrometric observations have led to estimates of their densities of  $0.65 \pm 0.08$  and  $0.63 \pm 0.11$  g/cm<sup>3</sup>, respectively (Nicholson *et al.*, 1992). Therefore, these icy objects are significantly underdense and may be typical of the material of which the small satellites and rings are composed. A major goal for ISS will be to derive improved shape models and volumes for these satellites to combine with improved orbits in order to get better estimates for their densities. During the nominal tour, an orbital switch of Janus and Epimetheus is due to occur in February 2006 when, over the course of a few days, Janus will move inwards by  $\sim 20$  km while Epimetheus moves outwards by  $\sim 80$  km. Observations of the switch have a particular importance for satellite and ring studies (see Section 2.3.1.2).

#### 2.1.4. Summary of Satellite Imaging Objectives

With these fundamental scientific questions in mind, the satellite science objectives for the Cassini ISS experiment include the following.

*All satellites:* Complete high-resolution global coverage to make geodetic maps, characterize the surface, and identify geologic resurfacing and tectonic mechanisms on all satellites; Acquire high-resolution and multiple-geometry images of cratered terrains for crater formation, size–frequency, and spatial distribution studies; Establish the spectrophotometric properties of surface units over a broader and more complete range of viewing and illumination geometries than currently available; Determine the nature of the dark material in the Saturn system; Establish the details of satellite shape to draw inferences about internal structure; Measure librations, where present.

Utilize the information gathered on all the satellites on tectonic patterns, albedo patterns, projectile populations, resurfacing events, composition, masses, densities, etc. to formulate a history (i.e., origin scenarios and evolution) of the entire Saturnian satellite system; Determine what is unique about this system's origin

and evolution, and how it differs from the satellite systems of Jupiter, Uranus, and Neptune.

Some satellite-specific objectives are given as follows.

- Mimas, Enceladus, Tethys, Dione, Rhea: Establish detailed morphology of topographic grooves to investigate their formation mechanism.
- Enceladus, Tethys, Dione: Examine resurfaced regions at high resolution, to investigate the resurfacing mechanism.
- Enceladus, Tethys, Rhea: Determine topography of relaxed craters, to infer rheology.
- Tethys, Dione, Rhea, Iapetus: Characterize global-scale photometric variations.
- Dione, Rhea: Obtain coverage at high resolution and a range of illumination and viewing geometries of “wispy” markings.
- Enceladus: Determine crater densities in youngest regions. Perform regular monitoring to search for eruptive events. Measure libration amplitudes as evidence of spin-orbit resonance and tidal heating. Use crater morphologies and dimensions to constrain the depth to a potential water mantle (or “subsurface ocean”).
- Tethys: Establish the morphologic details of Ithaca Chasma.
- Dione: Obtain high-incidence-angle coverage of ridges to confirm topography and global distribution.
- Rhea: Characterize the global distribution and orientations of polygonal crater rims.
- Hyperion: Investigate the details of color and albedo variations to help constrain the nature and origin of the dark material.
- Iapetus: Establish the details of the distribution of dark material at much higher resolution, particularly at the dark/light boundary. Establish the details of photometric properties and topography on the leading hemisphere, using images with high signal/noise ratio.
- Phoebe: Investigate the details of color and albedo variations to help constrain the nature and origin of surface material.
- All small irregular satellites: Globally characterize these bodies – cratering statistics, surface topography and morphology, shapes, colors, etc. – at high resolution. Search for evidence for collisional fragmentation and evidence of unique surface processes. Determine color variations among satellite terrains and differences or similarities to ring colors.
- Tethys/Mimas, Enceladus/Dione, Titan/Hyperion, Janus/Epimetheus: Use refined measures of their orbital elements and evolution to determine accurate masses and densities.

Observational plans to accomplish these goals are as follows.

- Global, low-resolution (few km/pixel, or better) observations covering as wide a range of longitudes as possible at approximately regular phase-angle increments, in concert with other remote sensing instruments, to characterize the global spectrophotometric properties of the satellites.
- At those times when satellites fill a substantial fraction of the NAC FOV, imaging from different viewing geometries throughout the ‘encounter’ allows for high-resolution morphology and color, as well as stereo observations for topography, and limb observations for shape.
- During those times outside of the ‘targeted’ flybys, when the satellite still subtends more than a NAC FOV, specific targets on the surface are selected on the basis of the low-resolution views obtained by Voyager. Many of these mosaics are in areas where there is essentially no useful Voyager coverage and thus are purely exploratory. The speed of the flybys determines roughly how many images can be obtained at these close ranges. The target characteristics influence whether stereo or color is sought at very high resolution over limited areas.
- ‘Targeted’ flyby imaging, to give very high-resolution (tens of meters per pixel) morphology of specific features (e.g., Figure 4) in those instances where Voyager data indicate potentially diagnostic features, such as structural forms, and to make surveys at high resolution where we currently have no specific geologic expectations. Color and stereo are important parts of these sequences, although the high angular rates restrict the amount of such coverage. Wide-angle images are also taken during close passes, as they can provide context and obtain more regional views at specific geometries than can be done solely with the NAC.
- Some very high-phase observations of Enceladus are planned to seek any associated particles or venting phenomena. Some of these are obtained while the moon is in the shadow of Saturn.

#### 2.1.5. Combined Studies with Other Cassini Instruments

Many instruments on the Cassini Orbiter in addition to ISS will observe icy satellite surfaces. These include the Composite Infrared Spectrometer (CIRS), the VIMS, the Ultraviolet Imaging Spectrograph (UVIS), and RADAR. Coordinated observations and scientific analyses of satellites are planned utilizing data from all instruments. ISS–VIMS coordination is important since the two instruments are functionally complimentary and co-analysis is scientifically powerful. (Co-analysis between comparable experiments on Galileo (SSI and NIMS) has proven fruitful (e.g., Lopes-Gautier *et al.*, 1998; Fanale *et al.*, 1998).) The spectrometer is limited to covering relatively small areas at moderate spatial resolution ( $\sim 1$  km/pixel or better) because of the high data volume produced by hyperspectral imaging and short period at close range to targets. The imaging experiment is limited with respect to compositional interpretations by the spectral range ( $0.25\text{--}1.1\ \mu\text{m}$  for ISS versus  $0.35\text{--}5.1\ \mu\text{m}$  for VIMS) and spectral resolution (even though ISS has many color filters). With a coordinated ISS–VIMS observation plan it is possible to achieve (1)

global mapping of color units with ISS (via wide-angle camera (WAC) when close and NAC when distant); (2) VIMS spectra that sample all color units at moderate resolution, to enable more definitive compositional interpretations of the ISS color units, and (3) high-resolution and stereo images of surface features for interpretation of processes (impact, tectonic, etc.). RADAR should be synergistic with ISS images and VIMS spectra of icy satellite surfaces, providing very different information (such as subsurface structure). CIRS and UVIS spectra, giving temperature and composition, can be related to the geologic context of ISS images.

## 2.2. SATURN'S ATMOSPHERE

The state of our knowledge of Saturn's atmosphere is immature in comparison with that of Jupiter's. As a starter, the colder temperatures of the Saturnian atmosphere result in a visible cloud deck being lower in the atmosphere, and overlain by a greater abundance of haze, than for Jupiter, so contrasts are intrinsically lower. Moreover, the jovian atmosphere has been more extensively studied – both from spacecraft and from Hubble Space Telescope (HST) – than Saturn's. For example, in the derivation of cloud-tracked winds, the Voyager imaging team gathered 10 times more wind vectors from Jupiter than from Saturn, owing entirely to the poor visibility of cloud features on the latter. The latest advances in jovian atmospheric science were made, in fact, by the Cassini ISS during the Cassini December 2000 Jupiter flyby (Porco *et al.*, 2003).

Nonetheless, what we do know about Saturn is that, unlike the apparent stability of the jovian jets, Saturn's atmosphere is remarkably changeable. HST images during 1990–1991 captured the eruption of a giant equatorial storm (Sanchez-Lavega *et al.*, 1991), and other similar disturbances in 1994–1997 (Sanchez-Lavega *et al.*, 1996, 1999). And recent observations (Sanchez-Lavega *et al.*, 2003) have suggested that the equatorial jet on Saturn has decreased in speed by a factor of two from 1996 to 2002, although it is not clear whether or not these recent observations sample the same level in the vertical wind profile as earlier measurements.

Cassini ISS goals are focused on using the unique spectral and photopolarimetric capabilities of the instrument to derive the observational quantities necessary for estimating the cloud and aerosol structure and energy balance in the atmosphere, to search for previously unseen atmospheric phenomena, to measure and understand the three-dimensional general circulation of the atmosphere, including indirect inferences about conditions below the visible cloud tops, and to measure the spatial, spectral, and temporal properties of Saturn's auroral and lightning emissions, the latter being especially important as tracers of atmospheric convection.

### 2.2.1. *Photometric and Polarimetric Studies of Saturn*

The spectrophotometric capabilities of the ISS, and its photometric precision and linearity, will be used to singular advantage in the study of the processes energizing the Saturn atmosphere. Accurate knowledge of the intensity, spectral variation, and

linear polarization state of light reflected from Saturn can be used to address a variety of atmospheric objectives, listed as follows.

1. Deriving the optical properties and vertical distribution of aerosols to develop quantitative models of radiative forcing, and investigate the coupled dynamical, radiative, chemical and aerosol microphysical processes that determine the state of the upper troposphere and stratosphere. This objective addresses the mean meridional circulation, vertical and latitudinal transports and seasonal effects.
2. Improving our understanding of the formation mechanisms and composition of aerosols in the stratosphere and upper troposphere by comparing their spatial distribution with models of their source regions, and by interpreting diagnostic photometric and polarimetric signatures such as halo features at specific scattering angles.

Radiative balance calculations for meridional circulation models require knowledge of methane absorption, particle distribution, particle single scattering albedo, optical depth, and scattering phase function throughout the entire spectrum. No single instrument can provide these quantities over the whole spectrum. The ISS can (with its suite of filters and observing strategy) provide information on methane absorption, aerosol distributions and optical properties from about 250 to 1000 nm. Knowledge of aerosol optical properties can be used to infer aerosol physical properties (size, shape, imaginary refractive index) which can be used to constrain aerosol microphysical models.

Aerosol single-scattering albedo, scattering phase function and linear polarization can be deduced from the types of measurements ISS will make, as summarized in Table III. The measurements listed in Table III are compared with multiple-scattering models to derive the phase function, polarization and single-scattering albedo. For Saturn the derivation of particle polarization at visible wavelengths relies on knowledge of the vertical structure as molecular scattering is strongly polarized. The vertical structure and aerosol properties must be modeled simultaneously.

TABLE III  
ISS diagnostics for aerosol optical properties.

Aerosol property	Measurement
Single-scattering albedo	Intensity at disk center at low phase angles at continuum wavelengths
Derivative of single-scattering albedo with depth	Limb darkening at low phase angles at continuum wavelengths
Phase Function	Behavior of intensity with phase angle
Polarization	Behavior of polarization with phase angle
Derivative of single-scattering polarization with depth	Center-to-limb behavior of the polarization

Aerosol optical properties lead to an estimate of aerosol physical properties. It is unlikely that particles are spherically shaped because the particles are most likely in the solid phase. Particles produced photochemically or as a result of auroral bombardment in Saturn's upper atmosphere may be aggregates of small ( $r \ll 1 \mu\text{m}$ ) particles (West and Smith, 1991). Unlike spheres, these types of particles can have phase functions that are forward scattering while at the same time producing strong positive linear polarization near  $90^\circ$  scattering angle. Table IV summarizes how optical properties will be used to infer physical properties.

Information on the vertical structure of the aerosols is carried by the same intensity and polarization data used for aerosol optical properties. The ISS has available four types of measurements for studies of vertical structure, listed in Table V.

The suite of measurements listed in Tables III and V will be combined to yield information on the vertical structure and optical properties of atmospheric aerosols. Images in each of the three short-wave (400–700 nm) polarizing filters on the NAC will be combined to produce linear polarization images. The orientations of the

TABLE IV  
ISS diagnostics for aerosol physical properties.

Aerosol optical property	Derived physical property
Phase function in forward scattering ( $\sim 20^\circ$ to $40^\circ$ scattering angle)	Particle effective radius
Single scattering albedo	Imaginary part of refractive index, particle composition
Halo feature	Crystal shape, refractive index, and composition
Polarization	Particle shape and effective radius (contingent on available laboratory or theoretical results)
Dependence of extinction cross-section on wavelength	Particle shape, after radius and imaginary refractive index are determined

TABLE V  
ISS diagnostics for aerosol vertical structure.

Measurement technique	Comments
Limb images	Vertical profiling (6 km/pixel at $16R_S$ in the NAC); Stratospheric vertical coverage to 150 mb at $1 \mu\text{m}$
Methane band photometry	ISS has three methane filters that probe to different depths
Polarimetry near $0.4 \mu\text{m}$ wavelength	Rayleigh scattering is highly polarized near $90^\circ$ scattering angle
UV center-to-limb photometry	Probes altitudes of UV-absorbers

polarization axes of these filters are offset by  $0^\circ$ ,  $60^\circ$  and  $120^\circ$  from the line in the image plane perpendicular to the Z-axis of the spacecraft. We estimate an uncertainty of  $\pm 0.5\%$  in the magnitude of linear polarization if  $5 \times 5$  pixel regions are summed. Two orthogonally oriented near-IR (700–1100 nm) polarizers are mounted in the WAC filter wheel. These give a good measure of the linear polarization, provided the spacecraft Z-axis is approximately parallel or perpendicular to the plane of scattering. Both short- and long-wave polarizers can be combined with passband filters, including methane filters to measure the wavelength dependence of the polarization. The NAC filter wheel contains a single near-IR polarizer which can be used to filter polarized light and provides deeper penetration of the atmosphere at intermediate phase angles.

Our measurement strategy for Saturn calls for images at many wavelengths, over the globe, and at many solar incidence, emission and phase angles. Of the spacecraft encounters with Saturn thus far, only the Pioneer imagers obtained good phase-angle coverage, but only at two wavelengths and not sufficiently dense in phase-angle coverage to look for halo features. During the Saturn tour, we will obtain images of Saturn at many wavelengths from the near-UV to near-IR, in three methane bands, and with polarization filters. The requirement to orient the spacecraft in order to align the axes of the polarizers with the scattering plane posed real but manageable operational constraints on observation planning.

Global views with the NAC are possible only if the spacecraft is greater than about  $60 R_s$  from Saturn; at closer range, the required number of images and observing time to cover the planet is prohibitive. Therefore, the Saturn approach period and the apoapses of the most distant orbits are the best times for global coverage in the UV and in the short-wave polarizing filters. Phase-angle coverage will be built up gradually over the tour. We will take advantage of special circumstances during the orbit. The orbital characteristics of the tour will permit good coverage in both hemispheres, especially at high latitudes on inclined orbits. We will make use of opportunities to photograph stars near the limb in order to establish accurate altitudes for limb hazes.

### 2.2.2. *Atmospheric Dynamics and Thermodynamic Structure*

The first-order science objective for the ISS atmospheric dynamics investigation is to determine the processes responsible for maintaining the banded alternating jet and cloud structure on Saturn. The only direct information comes from visible cloud levels and above, while the relevant driving mechanisms have their roots below. Thus, the challenge for Cassini ISS is to use imaging to infer as much as possible about conditions at depth. Voyager satisfactorily observed the cloud-top mean zonal wind field on Saturn (cf. Ingersoll *et al.*, 1984), and Cassini ISS will do the same, with the specific objective of verifying recent suggestions of weakening of the equatorial jet. We will document such changes at much higher resolution than is possible from HST, increasing confidence that the changes are associated with actual winds rather than wave motions. Multi-spectral imaging will offer the



possibility of detecting vertical shears in these winds and will allow us to determine whether the observed changes in the mean zonal wind of the equatorial jet are due primarily to changes in the wind at a given pressure level or to an upward shift of the visible cloud top after the disturbances of the 1990s. Observations of high latitudes in both hemispheres will allow us to extend our knowledge of the jet structure on Saturn farther poleward than was possible with Voyager, just as we did on Jupiter (Porco *et al.*, 2003), though observations of the north pole will not take place until after the nominal 4-year mission when that pole is finally illuminated by sunlight. Accurate observations of flow curvature can be combined with potential vorticity conservation and mixing concepts to learn more about the state of the atmosphere below the visible cloud level (cf. Dowling and Ingersoll, 1989; Allison *et al.*, 1995; Allison, 2000). However, observations of mean zonal winds alone are not sufficient to constrain the responsible dynamical mechanisms.

To understand jovian planet dynamics at the process level, additional information is required.

- (a) Voyager imagery indicates a variety of eddies on the jovian planets. Do these eddies maintain or deplete the jets (Ingersoll *et al.*, 2000), or is their role only secondary to that of other processes? Are the important drivers tied to deep-seated convection or do they originate in a shallower “weather layer” near and below the visible cloud tops? To understand Saturn’s heat and momentum budgets, we must observe eddy fluxes and eddy-mean kinetic energy conversions. Estimates from Voyager cloud-tracked winds exist, but the sampling is inadequate and perhaps biased. Over a period of three Saturn rotations (1.25 days) of useful imaging for cloud tracking (at resolutions of 50–100 km/pixel), Voyager obtained about 800 wind vectors, about 10% of that observed by Voyager at Jupiter because of Saturn’s lower contrast at visible wavelengths. RMS deviations from the mean wind speeds at different latitudes varied inversely as the square root of the number of observations, indicating that real eddy motions were not being measured, i.e., a  $S/N \leq 1$ . For Cassini to diagnose eddy motions reliably, a 10:1  $S/N$  is required, necessitating a wind vector inventory 2 orders of magnitude larger than that acquired by Voyager.
- (b) Mean meridional motions are diagnostic of deviations from geostrophic balance and hence provide clues about either thermally forced overturning circulations or mechanically driven (i.e., by eddy momentum flux convergences) cells. The sign of the convergence of the meridional wind indicates the global pattern of upwelling and downwelling and thus gives insights into cloud formation and dissipation processes as well as observed spatial variations in condensable gas concentrations. Meridional winds are anticipated to be several orders of magnitude weaker than mean zonal winds and perhaps comparable to the eddy wind components. Thus, the observational requirements are similar to those described in (a). In addition, since pointing errors can alias a small fraction of the zonal wind into a spurious first-order meridional wind, monitoring of

meridional motions requires that NAC cloud-tracking mosaics be accompanied by single-frame WAC images of the entire planet (or at least a large fraction that includes much of the bright limb) for the most accurate navigation possible.

- (c) The objective information acquired from circulation statistics is only one of the two complementary ways of observing jovian planet dynamics. By creating movies of the Saturn atmosphere in motion, we can observe the life cycle of vortices as they merge, split, or oscillate (Ingersoll, 1990; Polvani *et al.*, 1990; Li *et al.*, 2004; see movies of the Jupiter atmosphere at <http://ciclops.org>). The nature and time scales of these nonlinear interactions provide information about the vertical structure and depth of the layer in which they occur and hence constrain candidate theories for their formation. Movies also allow us to visually observe the eddy–jet interactions responsible for the eddy fluxes described earlier. They can be used to determine propagation characteristics of planetary-scale and mesoscale waves, which in turn constrain the unknown deep vertical stratification (cf. Allison *et al.*, 1990). Finally, movies can capture the rapid evolution of small-scale clouds typically interpreted as being the visible evidence of outflow at the tops of deep convective updrafts and hence diagnostic of Saturn’s deep water abundance and stability. The presence of near-infrared continuum, weak methane, and strong methane band filters on the NAC allows us to determine the optical thickness and top heights of such clouds and more confidently identify them as the products of moist convection (Banfield *et al.*, 1998; Gierasch *et al.*, 2000; Porco *et al.*, 2003). The observational strategy for Saturn movies is repeated multi-spectral global and regional imaging; a proper imaging sequence design can satisfy the requirements for both movies and cloud-tracking simultaneously (Porco *et al.*, 2003).
- (d) All the strategies described earlier infer information about the deep Saturn atmosphere indirectly from cloud-level signals. An opportunity for more direct sensing of deeper levels arises if Saturn has a sufficient inventory of water to experience deep moist convection (cf. Del Genio and McGrattan, 1990; Hueso and Sanchez-Lavega, 2001). If the lapse rate above the condensation level exceeds the moist adiabatic lapse rate, cloud-scale updrafts may be vigorous enough in some places to mix supercooled liquid water above the freezing level into regions of ice formation, and the resulting interaction can be expected to generate lightning. Jupiter lightning and moist convection detection by Galileo and Cassini (Little *et al.*, 1999; Porco *et al.*, 2003) has shown that convective storms occur only on the poleward sides of the eastward jets, i.e., in the cyclonic shear zones. This observation has broad implications because it implies that the belts are regions of net upwelling motion and convergence at depth, just the opposite of the traditional picture (Ingersoll *et al.*, 2000; Porco *et al.*, 2003). ISS results at Jupiter also confirmed that convection and lightning have different latitudinal distributions, implying cooler temperatures at higher latitudes above the condensation level. Finally, differences in lightning frequency on Jupiter seen through a narrow-band Cassini ISS filter and a

broad-band Galileo filter can be interpreted as an indicator of super-solar water abundance (Dyudina *et al.*, 2004). Thus, our goals at Saturn are to detect both moist convection and lightning, map their latitudinal distributions, and define the spectral characteristics.

The science objectives described earlier can be met with the following observational strategies.

On day-side apoapsis orbits.

- The majority of imaging for atmospheric dynamics will take place on orbits with distant day-side apoapses (of order 60  $R_s$  or greater, ideally) at low phase angles. This allows for maximum contrast in cloud features formed in reflected sunlight (a priority on Saturn, whose overlying haze reduces feature contrast relative to Jupiter), and allows global coverage to be obtained at resolutions comparable to that of Voyager with reasonably sized NAC mosaics plus single WAC frames of the globe for navigation. The best opportunities occur on orbits 49–52, when we will acquire repeated near-global mosaics near apoapsis (Fig-

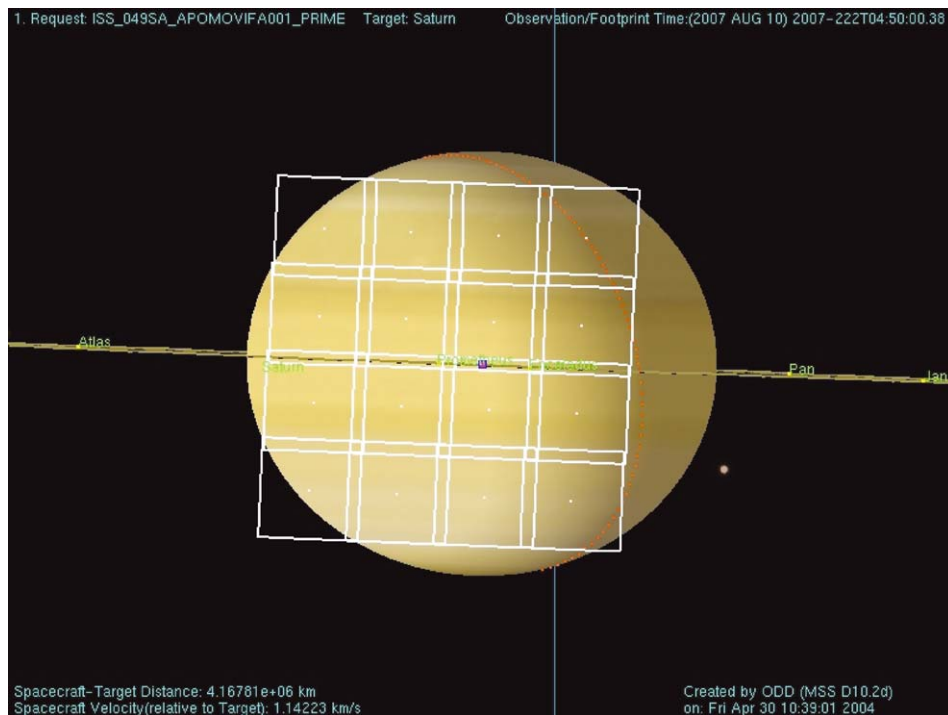


Figure 8. Typical mosaic of NAC frames of Saturn from the apoapsis of Rev 49, one of the most distant in the tour, which constitutes a single ‘picket’ or snapshot of the planet as it rotates. Mosaics like these are repeated every 1.75 h over a Saturn rotation, and then again over weeks (minus downlink periods), to form movie sequences for studying atmospheric dynamics.

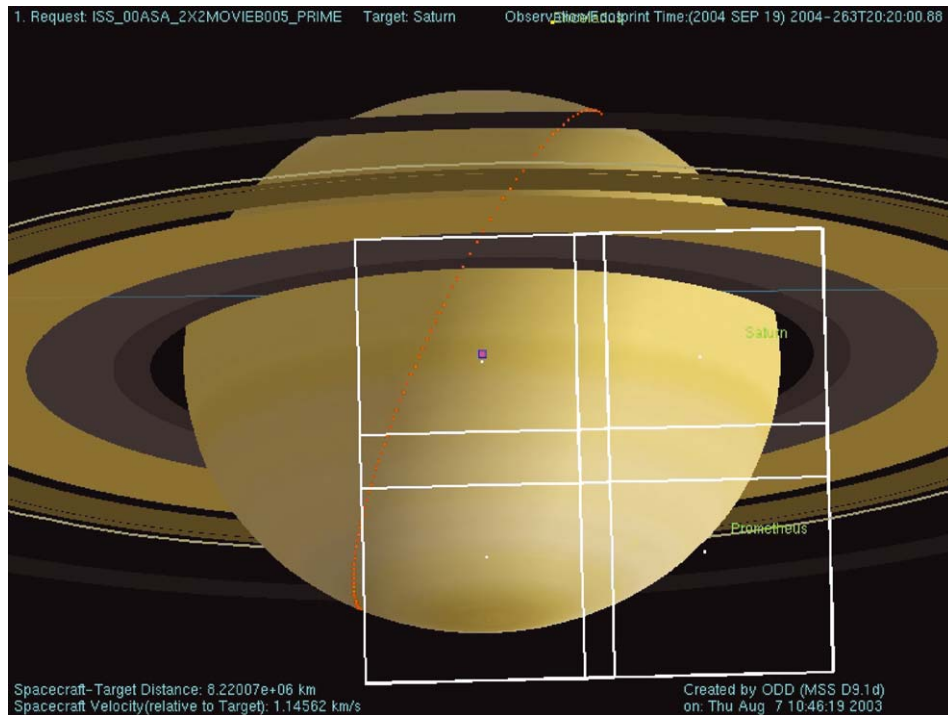


Figure 9. Typical ISS NAC mosaic of Saturn in 13 spectral filters early in the tour on Rev A for the study of atmospheric dynamics and spectrophotometry.

ure 8) in two filters (methane band and continuum) and higher-resolution strip mosaics along specific latitude bands outbound and inbound near  $40 R_s$  in six filters.

- Similar opportunities occur to a lesser extent during 96 days on approach to Saturn at lower spatial resolution and intermediate phase angles (Figure 1) but with better spectral coverage (generally, five or more visible and near-IR filters) and in orbit A, when moderate phase angles are sampled at very large distances (Figure 9).
- During orbits 4–20, when apoapses are close to  $40 R_s$  and phase angles moderate, two-color mosaics will be acquired in high-resolution longitudinal strips at different latitudes.

Each mosaic usefully observes only about a  $70^\circ$  wide swath on Saturn centered on nadir (outside this range, foreshortening and contrast loss due to the increasing slant path limit feature discrimination), and it is necessary to observe each meridian once per Saturn rotation to detect motions at all longitudes. To accomplish this, we will acquire mosaic sequences every 1.7–2.13 h as often as possible while the spacecraft is at least  $60 R_s$  distant from Saturn.

On night-side apoapsis orbits.

- Lightning storms flash once every few seconds, and the camera shutter must be open at least that long to reliably see the flashes. However, a day-side image saturates at these long exposures, so the lightning search must be conducted on the night side. At Saturn, reflected light from the rings illuminates much of the night side and tends to saturate the long-exposure images, though the rings will become fainter and this effect will be diminished as the tour progresses and the Sun descends towards Saturn's equator plane. During the Cassini tour, the best place to avoid both ring shine and direct sunlight is the north polar region, because the rings are over the horizon at latitudes greater than  $\sim 65^\circ$  and the north pole is in darkness during this season. Orbits 27–36 offer the best opportunities, because apoapse is over the north pole.
- We will also search for lightning on the large-apoapsis, high phase angle orbits 21–28, which offer better spatial coverage albeit with the potential for more ring-shine contamination. We will use a mix of exposure times and filters (broad-band clear, broad-band red, and narrow-band  $H\alpha$ ) to determine the best lightning detection strategy and to define its spectral signature. The spatial distribution, spectral range, and temporal variation of the emissions all are of interest. Because the distribution of lightning is not known, sequences are designed to scan the night-side atmosphere. In some cases, the same terrain is viewed on the day and night sides so that lightning strikes can be associated with specific cloud structures. A multi-instrument auroral campaign occurs in orbits 70–74.

'Feature track' sequences target specific atmospheric regions with NAC or WAC mosaics during several periapsis portions of orbits, when the NAC FOV is smaller than Saturn. Multi-spectral, spatial mosaics are acquired at several time steps, following a particular feature from day side to night side as was done by Galileo and Cassini at Jupiter (Little *et al.*, 1999; Gierasch *et al.*, 2000; Porco *et al.*, 2003). The day-side images allow one to study motions, cloud heights, and radiative properties, and the night-side images allow one to look for lightning. Targets vary throughout the tour, but include the equatorial and polar regions.

### 2.2.3. Auroral Phenomena

Trauger *et al.* (1998) present images taken by the HST of Saturn's UV aurora. The observations show the bright auroral arc on the day side of the planet. In contrast, ISS can image the aurora in visible light on the night side of the planet, and with much higher spatial resolution, than HST; it did so at Jupiter (Porco *et al.*, 2003). These differences are important for several reasons. First, the visible emissions represent less energetic processes than the UV emissions, and may be occurring by different mechanisms. Second, the day/night differences may reflect differences in the magnetic field upstream and downstream of the planet in the solar wind flow.

Third, the higher spatial resolution yields edge-on views of the limb that give the altitude of the aurora. One can also study the relation of the aurora to magnetic field lines and the time-dependent behavior of small features within the aurora. Such features might be monitored by particles and fields instruments as the spacecraft flies through the magnetic field lines that connect to surface features seen by ISS.

Aurora observations were made at Jupiter by Galileo (Ingersoll *et al.*, 1998; Vasavada *et al.*, 1999), and have proved useful in all the above ways. Cassini repeated the Galileo observations 4 years later (Porco *et al.*, 2003), and observed changes in position over periods of 10 h, 12 days, and 4 years. Some changes are due to local time-of-day effects at points on the planet. Other changes are due to the dynamic nature of the aurora. The Galileo Jupiter observations also revealed auroral-type emissions at the base of the magnetic flux tube that connects to Io. It will be interesting to see if any of Saturn's satellites exhibit similar phenomena. As with the lightning observations, the best opportunities are on orbits 27–36 when the apoapse of Cassini's orbit is over Saturn's north pole.

#### 2.2.4. Combined Studies with Other Cassini Instruments

Eddy heat fluxes have never been measured on any planet except Earth. Detection of correlated wind and temperature fluctuations would be an interesting and fundamental contribution to our understanding of Saturn dynamics, indicating whether baroclinic conversion analogous to that which dominates terrestrial midlatitude storms occurs on jovian planets. CIRS will retrieve temperatures just above the ISS viewing altitudes, though at much lower spatial resolution. CIRS may also retrieve the H<sub>2</sub> *ortho/para* ratio and abundances of condensable gases like ammonia (NH<sub>3</sub>), which are sensitive measures of upwelling and downwelling. Thus, coordinated ISS – CIRS scans across the Saturn disk are planned. This is best done near periapse when CIRS resolution is <1000 km, which is sufficient to resolve the large-scale eddies. Having 10 to 12 of these so-called “feature tracks” would allow one to sample all latitudes and dynamical regions.

Similar comments apply to coordinated VIMS–ISS observations. Because VIMS can measure in the strong absorption bands of methane and ammonia, as well as in the window regions, it can discriminate both high and low clouds in the atmosphere. ISS has a similar capability with filters that are sensitive to methane absorptions between 700 and 1000 nm (Banfield *et al.*, 1998). ISS has better spatial resolution than VIMS, but VIMS has better spectral coverage. Together they provide outstanding information on cloud heights and vertical structure. One goal, not yet realized for any of the outer planets, is to directly measure vertical wind shear, e.g., the variation of horizontal wind with altitude.

UVIS is generally sensitive to higher altitudes than ISS and the other instruments. Coordinated observations might yield evidence that dynamical features extend from cloud top levels into the upper atmosphere.

The observational strategy for measuring cloud-tracked winds at periapse is similar to that employed at Jupiter by both Galileo (Vasavada *et al.*, 1998) and

Cassini (Porco *et al.*, 2003). The problem is that the planet more than fills the FOV of the Cassini WAC, and the limb cannot be used directly as a reference to determine camera pointing. The same problem occurs with Galileo, which has no WAC to determine pointing for the NAC. In both cases, camera pointing is determined either by mosaicing in from the limb or by referencing to the large-scale features and jets, which are nearly steady in time. The small-scale motions are then determined relative to the large-scale features. For measurements of eddy fluxes and the eddy life cycles, these methods work quite well (Vasavada *et al.*, 1998).

The ISS shares many aerosol/radiation science goals with UVIS and VIMS. The UVIS will probe to shorter wavelengths than ISS while VIMS will probe at longer wavelengths. The shorter UV wavelengths and VIMS data in strong methane bands will be more sensitive than ISS to aerosols high in the stratosphere. The combined wavelength coverage of all three instruments will more tightly constrain aerosol models than is possible with any single instrument. The net radiative heating, which can be inferred from measurements with all three instruments, can be combined with information on net radiative (thermal-infrared) cooling provided by the CIRS instrument to deduce net heating and cooling for studies of stratospheric dynamics (West *et al.*, 1992).

### 2.3. SATURN'S RINGS

Voyager observations from a variety of experiments (imaging, stellar occultations, radio occultations) revealed a remarkable architectural diversity within the rings of all four giant planets. Saturn's rings are representative of all rings in being home to many of the types of features found around Jupiter, Uranus and Neptune. There are eccentric, inclined narrow rings; non-axisymmetric and sharp ring edges; broad, tenuous rings; incomplete arc-like ring segments; small moons 'shepherding' nearby ring material; tightly wound spiral waves; axisymmetric but radially irregular features; azimuthally asymmetric ring brightness variations; and a great deal more. A collisional disk if left to itself should spread until it is featureless. But Saturn's main rings are far from featureless.

Characterizing ring structure at a spatial scale finer, and a spectral range wider, than previously possible, determining its root causes, and searching for secular changes in the rings both during the multi-year long Cassini mission and since the Voyager era are prime objectives of the ISS ring investigations at Saturn. The latter in particular, if successful, will provide a direct measure of ring evolution time scales – at the heart of which is the rate at which angular momentum is being exchanged within and/or removed from the ring – and could definitively replace current theoretical and poorly constrained estimates of ring age and lifetime.

Ring structure may either be externally or internally caused. In the case of the main Saturnian rings, consisting primarily of cm- to meter-sized

particles – external causes can vary from meteoroid impacts to the gravitational perturbations of nearby or distant satellites or the non-sphericity of the planet's gravity field (see Section 2.3.1). Internal causes have their origins in the free mechanical energy derived from the global Keplerian angular velocity shear across the rings balanced by the energy dissipation and viscosity that arises from highly inelastic particle collisions. Even in the absence of external forcing, radial variations in particle number density (i.e., the number of particles per unit volume) across the rings may develop and self-perpetuate from initial local radial gradients in particular characteristics of the particle distribution: e.g., viscosity or effective local velocity shear in the presence of finite-sized particles (see Section 2.3.2). In the case of non-collisional tenuous rings made of dust-sized particles, atmospheric drag, Poynting – Robertson drag, and electromagnetic effects are among the external causes that can have dramatic and observable effects (Section 2.3.5). In each of these processes, a torque is imposed on a local patch of ring, angular momentum, the lifeblood of a collisional ring system, is exchanged, and the ring system evolves.

#### 2.3.1. *Ring Structure: External Perturbations*

The greatest success in explaining the origins and gross characteristics of the ring features that are composed of particles on longitudinally phased, eccentric and/or inclined orbits has been achieved by relying on the perturbations of satellites, either outside, or embedded within, the ring system. Most of the structure in the intermediate density A ring, for example, can be explained by the interactions with external satellites which force a sizable number of density and bending waves in the A ring at the location of their gravitational resonances, or by the presence of a tiny moon in the rings which opens and maintains a gap and also sculpts its wavy edges, such as the Encke gap. (The degree to which perturbations on ring particle orbits create visible disturbances in a featureless disk system depends on the ring's natural ability to distribute the change in angular momentum resulting from the imposed torque. If the angular momentum removed, deposited or exchanged is less than the ring's natural ability to carry the excess/deficit away from the excitation region, then the ring response (if any) will take the form of a wave. On the other hand, if the external torque is greater than this natural ring 'viscous' torque, then the ring will respond by opening a gap, presumably with sharp edges: the particles themselves must physically move to accommodate the external driving.)

However, despite the success in associating ring features with satellite perturbations, the detailed characteristics of most of these non-axisymmetric features are not completely understood.

**2.3.1.1. *Ring Edges.*** The origin and maintenance of extremely sharp edges ( $</\sim 1$  km) within the vast expanse of otherwise continuous ring material is of considerable interest. 'Flux reversal' – the phenomenon by which a resonantly perturbed ring may actually contribute to its own edge sharpening – has been predicted to occur in these locales (Borderies *et al.*, 1982, 1983). The two strongest resonant



perturbations in Saturn's rings are in fact responsible for the very sharp edges of the major rings A and B, as well as for their kinematics and non-axisymmetric shapes: i.e., the two-lobed rotating pattern of radial oscillations observed in the sharp outer edge of the B ring, and the seven-lobed rotating distortion observed in the outer A ring edge, are due to the Mimas 2:1 and the Janus/Epimetheus 7:6 Lindblad resonances, respectively (Porco *et al.*, 1984b).

In a simple model of resonant perturbations, the amplitude of a radial distortion is a function of the satellite's mass and other geometrical quantities. However, in both the outer A and B rings, the observed distortion amplitudes, and even the azimuthal shape, are not accurately described by the simple model. For the B ring, significant residuals ( $\sim$ several kilometers) in the fitted two-lobed model, the extension of the outer edge  $\sim 24$  km beyond the resonance position, and the fact that the distortion amplitude of  $\pm 75$  km is a factor of  $\sim 4$  larger than would be expected from the simple model indicate that other perturbations on the ring particle orbits are present. In an interplay of local and external influences, the rings' self-gravity and viscosity may play a role in enhancing the amplitude of the externally produced distortion (Porco *et al.*, 1984b); amplification of a standing density wave, excited at the Mimas resonance location and reflecting off the sharp outer B ring edge, may also help explain the amplitude enhancement as well as the extension of the ring beyond the resonance (Namouni and Porco, 2002). High-resolution imaging observations of this unusual region, taken over the course of the Cassini mission, will be critical in developing a full description of the rings' shape and behavior, which in turn will help constrain the region's surface mass density and viscosity, quantities that are presently unknown. The mass present in the outer B ring may also play a role in distorting the narrow Huygens ring 250 km beyond in the Cassini Division (Turtle *et al.*, 1991, 1992; Section 2.3.1.5), another reason why examination of this region is particularly interesting.

Understanding the confinement of the outer A ring edge offers a special challenge. Analysis of Voyager imaging and occultation data indicated that the shape and kinematics were consistent with a seven-lobed distortion rotating with the mean angular velocity of the co-orbital satellites. However, as with the B ring, the amplitude ( $\pm \sim 7$  km) is larger than predicted from simple resonant perturbations, and the latter are complicated by the presence of many potential components with slightly different pattern speeds. These arise from the frequency splittings associated with two fundamental frequencies: the mean orbital frequency of the two satellites and their libration frequency (Section 2.3.1; Porco *et al.*, 1984b). The 'side-band' resonances are spaced at  $\pm 3$  km on either side of the central resonance; the uncertainty in the A ring outer edge is  $\sim 8$  km, so it is unclear which, if any, is the dominating resonance and how the side resonances affect the observed behavior. (The satellites' eccentricities, and the uncertainty in the exact mass ratio of the co-orbitals, complicate this brew even further.)

Nonetheless, an interesting opportunity to examine this unusual configuration is presented by the swapping of orbits that the co-orbital satellites, Janus and

Epimetheus, will undergo in early 2006. Any resonances produced by these bodies should shift by measureable amounts as the outside moon moves to the inside track and the inside moon moves to the outside. This is a unique opportunity to see the rings respond to a very specific external stimulus. Although theory suggests that the edge region will take several months to settle into the new regime, valuable information on the physical properties of the rings will be gained by observing the switch and its consequences. High-resolution observations of this region, and adequate azimuthal coverage of the ring's edge, both prior to the switch and after, to monitor the response of the ring system, are required. The changing response of the rings at other resonances produced by these satellites (e.g., density waves throughout the A ring; see the following paragraphs) will also be examined. High-resolution radial scans of the entire ring region are planned to straddle the orbit switch.

**2.3.1.2. Waves.** The rings, particularly the outer A ring, contain dozens of density waves (Cuzzi *et al.*, 1981) and a few bending waves (Shu *et al.*, 1983). These tightly-wound spiral waves are excited by Saturn's moons Prometheus, Pandora, Janus, Epimetheus, and Mimas (Lissauer, 1985; Gresh *et al.*, 1986; Rosen *et al.*, 1991). The waves typically damp within  $\sim 100$  km of the resonance at which they are excited, and the wave region generally contains  $\sim 10$  cycles of the wave.

The forcing and damping of density and bending waves is a major and important problem in planetary ring dynamics. In principle, the observations of decaying waves provide a tool for probing the particles' physical properties and nature of the disk: the local ring surface mass density can be estimated through measurement of the variation in wavelength with distance from the resonance, and the damping rates inferred from the decrease in wave amplitude with distance can be used to derive an estimate for the local ring viscosity, and hence, the elastic ring particle properties. However, these results suffer from the fact that none of the theories of wave propagation, either linear or nonlinear, completely describe the observations as they presently stand. The strongest waves in Saturn's rings are all highly nonlinear, and radial profiles through the crests of the waves are generally noisy. Improved profiles of density waves, and improved measurements of the heights of bending waves from Cassini imaging and occultation observations, will aid this situation enormously. Also, as indicated earlier, the co-orbital satellites' swap and the consequent response of the ring to a changing external stimulus should help in independently ascertaining the A ring's internal properties, such as the ring's viscosity, in a perturbed region, a needed ingredient in interpreting density waves.

**2.3.1.3. Satellite Orbital Evolution.** The generation of spiral density waves at the location of a Lindblad resonance with a satellite leads to an exchange of orbital angular momentum. The net consequence is a secular evolution of the satellite orbit away from the rings. The exact rate of orbit expansion for a given satellite depends on parameters such as the surface density of the rings and the mass of the satellite.

Thus, in principle, if a satellite's mass is known, an observation of a secular change in its orbit can yield (i) a direct measure of the rate of ring evolution and (ii) a measure of the ring's surface mass density. However, with the exception of Janus and Epimetheus, the masses of the small satellites of Saturn are essentially unknown. Also, complications arise due to the mutual perturbations of the satellites on each other, which can also lead to changes in their orbital elements. The net drift rate of a satellite drawing angular momentum out of the rings at a Lindblad resonance will be slowed if it is in resonance with another satellite.

Prior to 1995, the best candidate for deducing the rate of angular momentum exchange between a satellite and the rings was Prometheus which drives a number of resonances within the A ring. Its orbit was expected to expand sufficiently rapidly that by 1995, over 14 years after the Voyager flybys, when the Sun and Earth passed through Saturn's ring plane as Saturn orbited the Sun, it should have lagged behind its expected Voyager-derived position by  $\sim 0.2^\circ$ . However, a lag that was 2 orders of magnitude larger than this was observed (Bosh and Rivkin, 1996; Nicholson *et al.*, 1996). Further, observations since 1995 using the HST indicated a similar problem with the orbit of Pandora. Both orbits changed again in late 2000 (French, 2003).

This is now known to be due to the chaotic environment in which the two moons reside – a circumstance initially pointed out by Borderies *et al.* (1984), subsequently detailed by Goldreich and Rappaport (2003a,b) – as well as the fact that every 6.2 years, the apsidal lines of Prometheus and Pandora become anti-aligned, bringing the satellites very close to each other. Other effects are certainly present in their orbits, such as a nearby Mimas 3:2 resonance.

One major objective of the ISS investigations at Saturn is refinement in the orbital elements of the known satellites, including Prometheus and Pandora, and a measure of their periodic and secular (if any) changes with time. An orbital integration of the whole satellite system will likely be needed to derive estimates of individual satellite masses from their mutual perturbations and to detect any secular changes due to these interactions or ring torques. Images are planned to capture all the known satellites at various points in their orbits and throughout the tour for just this purpose; many ring images will serendipitously capture the ring region satellites over the course of the mission. These measurements will be combined with observations of these bodies made by Voyager 25 years earlier and HST in the interim. Relative precisions in the orbital elements of the known small satellites of  $\Delta n/n \sim 10^{-9}$ , and  $\Delta e/e \sim \Delta i/i \sim 10^{-4}$  can be expected by the end of the nominal 4-year orbital tour.

For geophysical purposes as well, the satellite densities are of great interest. Janus, Epimetheus, Prometheus and Pandora are all believed to be very porous, with densities less than  $1 \text{ g/cm}^3$ . The fact that the densities of most of the small satellites and even of the ring material itself are unknown highlights the need to obtain masses of objects by observations of their gravitational effect on other bodies, since no targeted flybys from which mass might be determined from spacecraft tracking are planned. We require good size and shape models of the satellites in

order to determine their densities. Images to capture ring region satellites at high resolution are planned for this purpose.

*2.3.1.4. Planetary Acoustic Oscillations.* Traveling acoustic oscillations within the body of Saturn, in particular the low degree f-mode oscillations which have the potential to create the largest disturbances among all the modes, have been suggested (Marley and Porco, 1993) as a source of particular waves observed in the inner C and D rings (Rosen *et al.*, 1991). Present application of this idea is hampered by an incomplete description of the waves in question and the ambiguity in the assignments of particular waves to particular f-modes. Cassini observations are planned to ascertain the nature of these features and test the acoustic oscillation hypothesis.

*2.3.1.5. Gaps, Embedded Moons and Ringlets.* Saturn's rings contain about a dozen true gaps, defined as regions with  $\tau \ll 0.01$ , with widths ranging from  $\sim 20$  to 400. As stated earlier, gaps may be opened by very strong resonances; e.g., the Mimas 2:1 resonance that sculpts the outer B ring edge is also responsible for the Huygens gap in the inner Cassini Division (Goldreich and Tremaine, 1978). But gaps may also be opened by an embedded moon, and the requirement for doing so, and the size of the resulting gap, depend on the balance between the torque imposed by the satellite and the ring's natural viscous torque. In the only case known so far, the 10-km-radius moonlet Pan clears the 325-km wide Encke Gap in the outer A Ring (Showalter, 1991); this configuration is consistent with the density of Pan being similar to that for Janus and Epimetheus ( $\sim 0.6 \text{ g/cm}^3$ ) and a viscosity found for the A ring by the examination of density waves:  $\sim 100 \text{ cm}^2/\text{s}$ .

Pan also causes the Encke Gap to have wavy edges (Cuzzi and Scargle, 1985) with a wavelength of  $0.7^\circ$ , and causes quasi-periodic optical depth fluctuations ("moonlet wakes") in the surrounding A ring (Showalter *et al.*, 1986; Lewis and Stewart, 2000). In fact, the presence, mass and separation of a small satellite can be deduced by detections of edge waves and wakes in a gap's edges, owing to the gravitational impulse that the satellite imparts to passing ring particles and consequent excitation of orbital eccentricities in the ring particles. Pan was, in fact, discovered by its perturbations on the edges of the Encke gap.

The Encke gap also contains unusual arc-like and contorted ring segments, one of which appears to be the same orbit as Pan and may even be gravitationally confined by it. There are few images of these rings; they may have a similar relation to Pan that the Neptune ring arcs have to the moon Galatea (Porco, 1991). ISS will undertake a survey the Encke gap to catalogue all edge-wave phenomena and characterize the unusual rings within the gap.

Edge waves were also detected in the 35 km wide Keeler gap (Cooke, 1991) at the outer part of the A ring but Voyager provided limited azimuthal coverage and no satellite has been detected in the gap. The Keeler gap is also more puzzling than the Encke gap because the observed edge waves appear to have varying wavelength

and the observed amplitude implies the presence of a satellite that should have been detected by the Voyager cameras. One possibility is that more than one satellite is involved.

A number of genuine narrow gaps in the Cassini Division, the Keeler Gap in the outer A Ring and a few in the C ring are presumably caused by small moonlets, but the putative bodies have not been observed. Narrow (and frequently eccentric) ringlets are found in many of the gaps and are in some cases close analogs of the Uranian rings (Porco, 1990). Numerical simulations show that ringlets like the Huygens ringlet in the inner Cassini Division or those in the C ring can form at isolated Lindblad resonances (Hänninen and Salo, 1994, 1995; Goldreich *et al.*, 1995; Rappaport, 1998). The Colombo Gap in the C ring is associated with the relatively strong Titan 1:0 apsidal resonance. This resonance dominates the kinematics of a narrow eccentric ring within the gap and may be an example of a resonance that simultaneously maintains a gap and shepherds a narrow ring (Porco *et al.*, 1984a). On the other hand, the Maxwell gap in the C ring and the narrow eccentric ringlet that resides in it are not associated with any resonance. Presumably a small so-far-undetected moonlet is both creating this gap and shepherding the ring. Moonlets in these gaps in the C ring, where the viscous stresses are likely to be smaller, could be on the order of a few kilometers in radius and still clear their host gaps. Other gaps throughout the rings, similarly bereft of any definite cause, may also host small moons.

The non-axisymmetric structures detected at the edges of the A and B rings and the Encke and Keeler gaps, and the narrow eccentric rings in the Maxwell and Colombo gaps, are all regular in nature and reasonably well understood. In contrast, the chaotic-looking structure in the F ring system has yet to be satisfactorily explained. The two so-called “shepherding” satellites, Prometheus and Pandora, are expected to produce wave-like structures on the various components of the ring but the Voyager images show a more confused picture, with strong evidence of variability in the F ring region on a variety of time scales. Some of the F ring strands appear to be intertwined in Voyager 1 images and then to be a series of parallel strands in Voyager 2 images 9 months later. Clump-like structures were observed in Voyager and HST images that apparently persist for no longer than 9 months. The ring is seen to brighten locally, perhaps due to meteoroid impacts (Showalter, 1998) or tidal breakup (Nicholson *et al.*, 1996). Some of these phenomena, such as strand alignment and the unusual azimuthal structure, suggest the presence of small satellites undetected by Voyager. What is lacking is complete, high-resolution, azimuthal coverage of the ring and its surrounding region at different epochs in order to determine the structure and monitor its evolution.

A major objective of the ISS ring imaging investigation, and one for which a substantial number of images is planned, is a search for moonlets in gaps in the main rings and outside the A ring in the F ring region, a search for their gravitational effects on nearby ring material and the determination of their orbital elements. (In the absence of direct detections of a satellite, the observations of edge waves and other

perturbing effects on surrounding ring material can be used as a diagnostic tool to infer a satellite's existence and, with sufficiently good data, its orbital and physical parameters.) These will be conducted by imaging over  $360^\circ$  of longitude when the spacecraft is at reasonably high latitude and has a more-or-less uninterrupted view of the rings. (Other supplemental observations directed towards this end, which will be less taxing on spacecraft resources, are movie sequences of the ansa of a ring feature or gap, generally at lower resolution, to observe material and possibly moons moving through the FOV.) Selected targets for the high-resolution azimuthal scans and the ansa movies are the F ring, the Keeler gap (which will also capture the outer edge of the A ring), the Encke gap, the inner and outer Cassini Divisions, several gaps in the C ring, and the D ring. Because the structure expected in these regions – either edge waves or narrow, eccentric ringlets or complex F ring structure – is expected to evolve with time, and because precise orbits for embedded moonlets are desired for investigations of their dynamical interactions with surrounding ring material, these azimuthal scans and movies are repeated at various times over the 4-year mission. For the F and Encke ringlets, observations are planned when the spacecraft is close to the planet and at high phase, where these dusty rings are brightest.

The same data sets will be used to delineate the orbits, and investigate the kinematics, of any eccentric rings or ring edges within or forming the gap. As a general rule, the kinematic behavior of such features is predominantly influenced by the planet's non-spherical gravity field, perturbations by both distant and nearby satellites and rings, and by the self-gravity of the constituent ring particles (Porco *et al.*, 1984a; Porco and Nicholson, 1987). The greater the accuracy to which the kinematics are known, the greater the degree to which these individual contributions may be separated. The addition of data collected during the ground-based 28 Sgr occultation by Saturn's rings to the pool of Voyager imaging and occultation data on the behavior of the narrow Huygens ring outside the B ring confirmed that the ring consists of a freely precessing, simple elliptical component (commonly observed in narrow eccentric rings of Saturn and Uranus) as well as a double-lobed component apparently forced by both the nearby Mimas 2:1 resonance and the double-lobed shape of the outer edge of the B ring itself (Turtle *et al.*, 1991). Cassini observations, in concert with Voyager and previous ground-based occultation observations, will permit the search for additional modes in other narrow rings. Finally, a slight, but as yet unmeasured, inclination to the F ring may account for many of the properties displayed by the system as a whole during the 1995–1996 ring-plane crossing (Nicholson *et al.*, 1996). Developing accurate shape and kinematical models for all of Saturn's eccentric and inclined ringlets is a high priority of the Cassini ISS investigation.

The observations of satellites in gaps, and the accurate determination of their orbital elements, are key to understanding the fundamental dynamical interactions between a body and its host particle disk, whether it be a moon in Saturn's rings or a proto-planet carving out a gap in the exo-solar disk from which it has formed. It is not clear whether or not, in the case of Saturn's rings, the body's orbit will

be circular or eccentric, and the outcome will decide the nature of the ring–moon interaction as well as guide interpretation of astronomical observations of exosolar disks and their phenomenology. To improve on the high-resolution azimuthal scans and lower-resolution ansa movies targeted to gap regions where moons are expected to be, retargetable observations are planned in which the target can be decided shortly before uplink of commands to the spacecraft. Any moon discovered in a gap and whose orbital parameters are known well enough to predict its location at a future time will be imaged again using these ‘place-holder’ opportunities. Multiple observations at different positions in an orbit of an embedded moon are essential to detect the anticipated radial excursions of any eccentric orbit: i.e., no larger than half the gap’s width. Relative precisions in orbital elements of  $\Delta n/n \sim 10^{-8}$  to  $10^{-9}$ , and  $\Delta e/e \sim \Delta i/i \sim 10^{-3}$  from both planned searches of gaps and follow-on retargetable observations are expected by the end of the nominal 4-year orbital tour.

### 2.3.2. *Ring Structure: Internal Causes*

In marked contrast to many of the non-axisymmetric structures described earlier for which some degree of success has been achieved in devising an explanation, almost all the fine-scale structure that is observed throughout the optically thick B ring (Figure 10) is still unexplained and not even fully characterized. This ring region exhibits large, radially irregular, axisymmetric variations in brightness

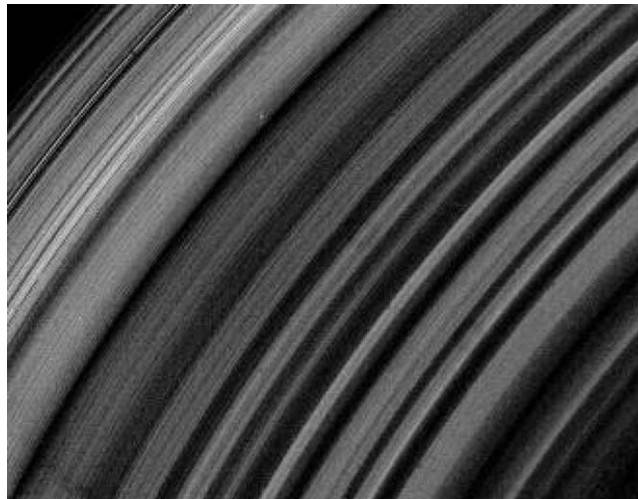


*Figure 10.* Voyager image of the lit face of Saturn’s B ring covering a region  $\sim 6000$  km across. The narrowest features here are 4 km wide. There are no gaps in this image: variations in brightness across the rings are due to a combination of differences in ring particle density and light scattering properties. All of the features in the image remain unexplained.

at the smallest scales observable in Voyager images (4 km), up to the dominant spatial scale of 100 km (Horn and Cuzzi, 1996); some of brightness variations appears to vary with ring longitude. There are few resonances in this region. There has been some suggestion that this structure represents not the usual radial variations in optical depth but in ring particle albedo, instead. The presence of this irregular structure, regardless of the cause, is surprising because the time scale on which such irregularities should be removed is shorter than the estimated age of the rings.

Various explanations for this irregular structure have been proposed since the early 1980's. Depending on the surface mass density of the ring, dynamical instabilities such as the diffusion instability (or 'viscous instability'; e.g., Ward, 1981), and the pulsation instability (or 'viscous overstability'; e.g., Schmit and Tscharnuter, 1999; Schmidt *et al.*, 2001) can be active and lead to the formation of axisymmetric structure. (The latter can also lead to non-axisymmetric structure.) A diffusion instability could occur in regions where the viscosity arises from the momentum transport associated with the random motions of the particles. A pulsation instability prevails when the viscosity is dominated instead by non-local momentum transport through a densely packed region of particles without particle transfer. In the case of the B ring, where the optical depth is large and the filling factor is high, the diffusion instability is unlikely to be a contender as the explanation of the irregular structure, and the pulsation instability apparently gives rise to sub-kilometer structure in dense rings, unlike the 100-km scale structure observed in the outer B ring (Schmit and Tscharnuter 1999; Salo *et al.*, 2001; Schmidt *et al.*, 2001). A third possibility is the presence of liquid–solid phase transitions in the B ring, and a suggestion has recently been made (Tremaine, 2002) that shear-dependent cohesive forces among the ring particles could lead to nested and narrow annuli of 'solid' and 'liquid' regions. In this case, the resulting irregular structure would depend on how the tensile strength responds to the Keplerian shearing motion.

Clearly, structure throughout the B ring has to be spatially and temporally characterized. The degree to which it is caused by albedo variations, perhaps due to random meteoroid impact events, needs to be determined. Radio and stellar occultations, together with high-resolution imaging observations, will be needed to determine the variation in optical depths across the region, as well as the character of the region at scales less than 4 km, the smallest that Voyager images were able to achieve. Models for the response of the ring to the Mimas 2:1 resonance and the effect of this ring region on the dynamics of the Huygens ring will also be valuable in providing an independent estimate of the surface mass density and viscosity in this region. Understanding how a dense ring, essentially left to itself, forms detailed structures like the one observed in the outer B ring will prove illuminating in understanding disk structures of much larger scale, like the proto-solar nebula, exo-solar disks around other stars and even the spiral galaxies.



### 2.3.3. *Photometric Studies of Saturn's Rings:*

#### *Particle Properties and Disk Structure*

The largest particles in Saturn's rings in any substantial number are of order 10 m in radius (Zebker *et al.*, 1985; French and Nicholson, 2000), and the ring thickness is likely to be of the same order. By contrast, even the images taken closest to the rings during SOI will have resolutions of  $\sim 100$  m/pixel. Thus, the ISS will not image the ring particles directly. In order to infer the nature and spatial distribution of the ring particles (e.g., the ring thickness), we must use indirect means.

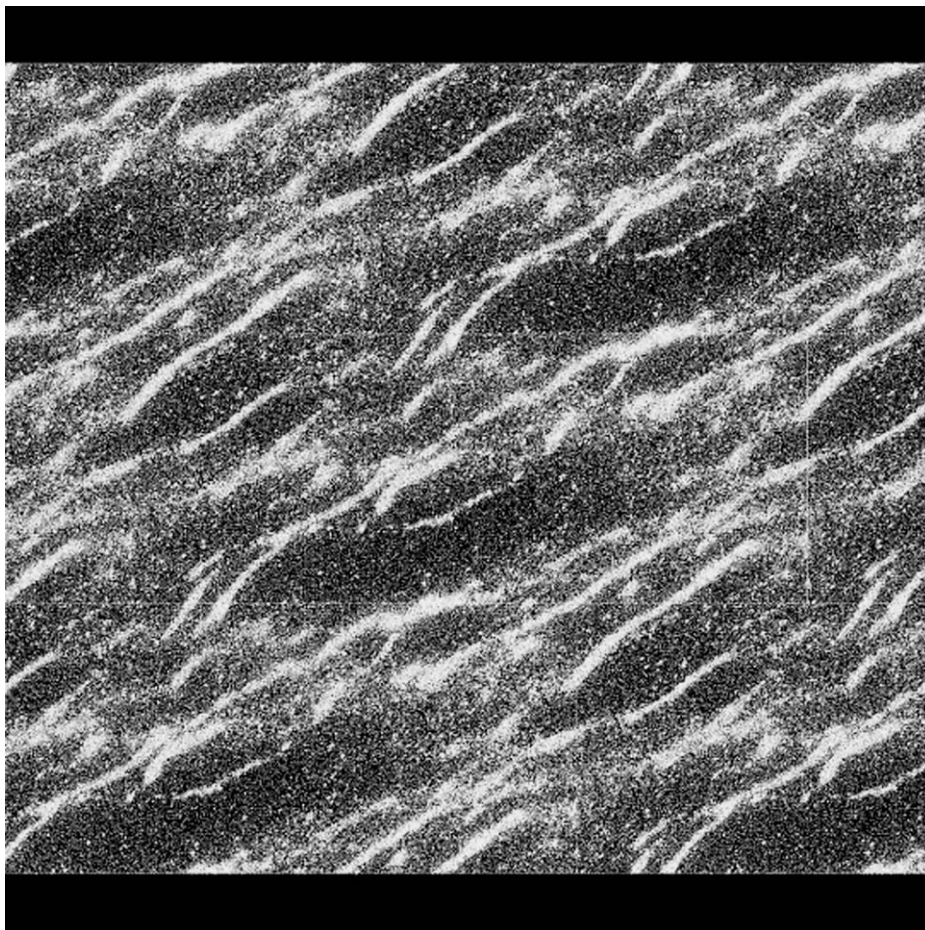
One such method is to measure the reflected or transmitted brightness ( $I/F$ ) of the rings in different geometries. Such geometries include the sunlit and unlit faces of the rings, and in backscatter (nearly "full" phase, i.e., opposition, or near-zero solar phase angle) and forward scatter (nearly "new" phase, or near  $180^\circ$  phase angle). As measured by cross-sectional area, or optical depth, most particles in the main rings are much larger than the wavelength of visible light. Such particles are strongly backscattering. At visual wavelengths, the reflectivity of the main rings is dominated by singly scattered sunlight in backscatter, and by multiply scattered sunlight and singly scattered "Saturn-shine" in forward scatter.

By contrast, the F ring and the tenuous D, E and G rings are dominated by microscopic "dust" particles, and these rings are brighter in forward-scattering geometries due to the diffraction of light by wavelength-sized particles. Multiple scattering is negligible for the D, E, and G rings (and generally for the F ring as well).

Many published photometric models of Saturn's rings (e.g. Cuzzi *et al.*, 1984; Dones *et al.*, 1993) use the formalism of classical radiative transfer, which in its simplest form assumes a vertically thick, horizontally homogeneous ring (Chandrasekhar, 1960). Such models are convenient because multiple scattering can easily be calculated using, for example, an adding-doubling code (Hansen and Travis, 1974). However, even if the rings were at first physically thick, collisions would rapidly flatten them until they were only a few particles thick (Jeffreys, 1947; Brahic, 1977; Wisdom and Tremaine, 1988). Dones *et al.* (1993) noted a number of discrepancies between classical models and the measured  $I/F$  of the A ring, such as its low brightness at large phase angles. More realistic models in which the rings are physically thin and/or clumpy have recently been formulated, and have gone a long way in resolving the disagreements between models and observations (Porco *et al.*, 2002; Salo and Karjalainen, 2002).

Specifically, the so-called "azimuthal asymmetry" in Saturn's A ring, a quadrupole variation of the ring's reflectivity seen in ground-based, Voyager, HST, and radar images (Thompson *et al.*, 1981; Smith *et al.*, 1981; Dones *et al.*, 1993; French *et al.*, 2000; Nicholson *et al.*, 2000) is thought to be caused by the presence of transient "wakes" of much-enhanced particle density in the rings that form due to local gravitational instabilities and then shear out (Figure 11; Colombo *et al.*, 1976; Franklin and Colombo, 1978; Dones and Porco, 1989; Salo, 1992, 1995; Richardson, 1994; for an animation, see <http://www.astro.umd.edu/~dcr/Research/ringpatch.mpg>).

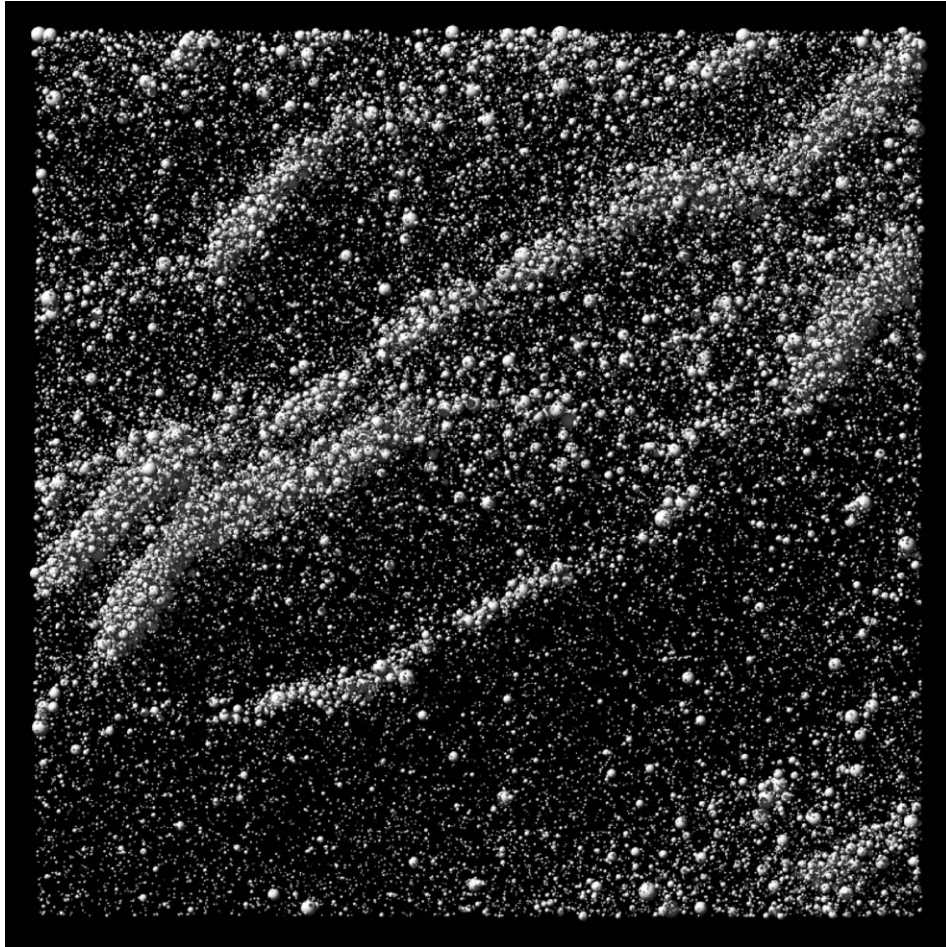
The separation and length of these wakes is of order 100 m; their long axis trails the direction of motion of the ring particles by some  $26^\circ$ . Because the number of particles contributing to the reflected light seen by an observer depends upon the orientation of the wake, the ring brightness has minima about  $26^\circ$  from the ring



(A)

*Figure 11.* (A) A snap-shot taken from a large-scale computer dynamical simulation (Porco *et al.*, 2005) showing 220,000 particles in Saturn's mid-A ring after 10 complete orbits. (The middle panel is  $230 \text{ m} \times 580 \text{ m}$ ; the panels above and below are the sliding patches which accomodate periodic boundary conditions.) Parameters for optical depth, particle size distribution, surface mass density and particle elastic properties characterizing the A ring were used in this simulation. The radial direction is up; orbital motion is to the left. At this stage, the evolution of the system is characterized by the rapid (one orbit) formation, dissolution and reformation of filamentary wake-like structures with a pitch angle of  $\sim 26^\circ$  to the azimuth and an average separation of 100 m, in agreement with theory. (B) The innermost  $190 \text{ m} \times 190 \text{ m}$  portion of (A) containing  $\sim 52,500$  particles, illustrating expected particle distribution. Figures courtesy D. Richardson, U. Maryland.

(Continued on next page)



(B)

*Figure 11. (Continued).*

ansae. Recently, two groups have performed realistic simulations of the asymmetry that incorporate both large-scale N-body simulations and ray-tracing photometric modeling (Porco *et al.*, 1999, 2001; Salo *et al.*, 1999, 2000). These simulations show broad agreement with the observed properties of the asymmetry, with the exception of the amplitude which has not yet been successfully modeled. The amplitude of the asymmetry depends upon several parameters, including the surface mass density of the rings and the coefficient of restitution, which measures the degree of elasticity during interparticle collisions. Further modeling of the asymmetry should provide an excellent probe of the properties of the rings, such as their viscosity (Daisaka *et al.*, 2001). By contrast, analysis of spiral density and bending waves, which thus far have provided much of our understanding of the rings' mass density and viscosity,

provides information on parts of the rings that have been strongly perturbed by external satellites. Wave regions typically have larger values of mass density and velocity dispersion, or viscosity, than unperturbed regions (Shu, 1984).

During SOI the putative wakes in the A ring may be marginally resolved by the NAC. Direct confirmation of their existence would provide an important test of dynamical models, as well as a measure of the surface mass density in the A ring (since the spatial scale of the wakes is determined by this quantity), and would help to remove ambiguities in modeling of the rings' reflectivity measured at grosser resolution throughout the main tour.

Ring color, in particular its variation across the rings, is also of interest as it may relate to ring origin and ongoing processes which alter ring particle surfaces like meteoroid bombardment and interaction with the magnetosphere. The particles in the C ring and Cassini Division are generally darker, less red, and smaller than those in the B and A rings (Cuzzi *et al.*, 1984; Esposito *et al.*, 1984; Estrada and Cuzzi, 1996; French and Nicholson, 2000). The significance of these differences and the presence of color differences on smaller spatial scales will be sought. Images taken on approach to Saturn in 2004 already show color variations across the B ring (Figure 1).

Another photometric phenomenon which is diagnostic of ring structure is the opposition effect in which the ring brightness increases dramatically very close to zero phase. This effect probably results from a combination of physical optics within the particle surfaces (coherent backscattering, Poulet *et al.*, 2002) and "shadow-hiding" between different particles. The angular width of the shadow-hiding effect depends on the thickness of the ring and the ring's particle size distribution, and provides one of our best diagnostics of the rings' vertical structure.

#### 2.3.4. *Spokes*

On approach to Saturn in 1980, Voyager 1 imaged faint, dark, nearly radial, wedge-shaped spoke-like features extending across Saturn's B rings. Observations of these features by both Voyager 1 and 2, taken over the course of each encounter and through a large range of phase angles and imaging resolutions (Smith *et al.*, 1980, 1981) indicated that spokes were typically 10,000–20,000 km long, ~2000–5000 km wide, occurred only in the B ring, and straddled the radial location where Keplerian ring particle motion is identical to the magnetic field motion. On short time scales (minutes), they orbit the planet with the Keplerian motion, resulting in shearing away from radial in the trailing sense. Spokes were most readily visible on the illuminated morning ansa of the rings, where ring particles have emerged from Saturn's shadow, and over long periods (many rotations) their appearance there was found to vary in contrast and areal coverage with the period of Saturn's magnetic field (Porco and Danielson, 1982). Also, greatest spoke activity occurred within the same northern magnetic field sector responsible for the emission of Saturn Kilometric Radiation. (There is a suggestion that spoke activity on the rings also varied with a period equal to that of the broad-band Saturn Electrostatic Discharges,

but this finding was less convincing (Porco and Danielson, 1984).) Spokes are likely composed of micron-sized particles elevated above the main ring particles (Smith *et al.*, 1981; Doyle and Grun, 1990), accounting for their reversal in contrast (with respect to the rings) between low- and high-phase viewing geometries. Only four spokes were observed to form by Voyager; the upper limit to the formation time was  $\sim 4$  min. Very few spokes have been observed from the ground (Colas *et al.*, 1995), and those observed by the HST (McGhee *et al.*, 2004) were visible only when the elevation angle of the Earth (Sun above or below the rings) was less than  $\sim 15^\circ$ . The latter authors attribute the difficulty in seeing spokes at other times to a photometric effect: low elevation angles producing long line-of-sight pathlengths through clouds of dust, making them more visible in those geometries. Others suggest that the appearance of spokes at some times and their absence at other times, and their observed orbital distribution, may be a seasonal effect related to the variable flux of meteors on the rings from heliocentric orbits during the Saturn year (Cuzzi and Durisen, 1990).

Models proposed for the origin of spokes have all invoked electromagnetic forces (which have their greatest effect on small, dust-sized particles) operating on clouds of dust debris generated by the impact of a meteoroid onto the rings (Goertz and Morfill, 1983; Goertz, 1984; Tagger *et al.*, 1991). Spoke formation times have been calculated under some of these scenarios to be as short as tens of seconds.

Cassini will provide the opportunity to gather far more information on these elusive and mysterious features. The hemisphere illuminated by the sun during the Voyager epoch was the northern Saturn hemisphere; the nominal Cassini orbital tour takes place during southern summer. If the appearance of spokes is related at all to seasonal effects, it should be discernible in Cassini data.

Ring imaging campaigns to capture spokes, either on the illuminated or unilluminated part of the rings, with imaging intervals of  $\sim 1.5$  h, are planned at various times throughout the orbital tour to confirm the periodicities and orbital phases observed by Voyager. Recent Cassini approach observations by the RPWS indicate an SKR period that is 1% longer than that observed in 1980–1981. Will the spoke periodicity also be longer? Will the SED period be confirmed? The capability of the ISS to acquire images with an interval as short as 11 s will be utilized in several observing sequences throughout the tour to capture spokes in the act of forming. As Voyager indicated significant modification in spoke activity when spokes pass through the shadow region, image sequences have been planned for observing ring material before and after shadow passage. Finally, to understand the details of the evolution of spoke morphology, spoke ‘tracking’ sequences are planned to follow spokes around the rings. As the spoke formation process is a stochastic one, there are no assurances that any of these observations will be successful. Spokes have not so far been observed on approach to Saturn from an spacecraft elevation angle of  $\sim -16^\circ$ , and a solar elevation angle of  $\sim -25^\circ$ .

### 2.3.5. Diffuse Rings

Diffuse, extensive clouds of dust encircle Saturn. These structures, reaching out as far as  $8 R_s$ , are of substantial scientific interest (Burns *et al.*, 2001) because, in some respects, the physics governing tenuous rings is simpler to understand than that of Saturn's more familiar rings where collisions are frequent. In addition, the widely separated particles comprising these rings concern some spacecraft engineers because Cassini will repeatedly traverse these diaphanous structures; the consequent impacts, occurring at high speeds, may jeopardize the entire spacecraft or its components (Burns *et al.*, 1989).

We define a diffuse ring as any with normal optical depth less than 0.001; this somewhat arbitrary separation means that collisional time scales in diffuse rings are less than orbital precession times. Saturn's diffuse rings then include the D ring, portions of the F ring, especially that lying radially interior to the main strands, the E ring, the G ring, and perhaps the contorted Encke ringlet (s).

Since the lifetimes of individual dust grains are brief, diffuse rings must be continually regenerated from source bodies (Burns *et al.*, 2001). General goals for the investigation of faint rings include (i) comprehensive photometric coverage to allow size distributions (indicative of dust origin and evolution) and particle shapes to be inferred; (ii) the search for sources (parent bodies, probably small moons) and sinks (satellite surfaces, Saturn's main rings and atmosphere, as well as particle destruction); and (iii) signatures of the symbiosis between the dusty rings and ambient plasma as well as the effects of circumplanetary dust on the coating of satellites through orbital photometry.

By their very nature, diffuse rings are difficult to study observationally: they are faint and often three-dimensional, meaning that lines of sight may pierce the structure in several places, confounding a simple interpretation. Long exposures, especially when taken along shallow slant paths through the ring in order to increase the signal, have proven effective. Unfortunately, light from nearby bright sources scattered into the optical imaging device has complicated interpretations (Throop *et al.*, 2004). Images taken at shallow elevations can be effective in determining ring thicknesses. The boundaries of the planet's shadow across these rings were used by Voyager scientists to selectively demarcate very faint rings from the blackness of the sky background; similar techniques will be used on Cassini, employing the shadows of the planet and perhaps large satellites.

Faint rings usually contain primarily small particles, which effectively forward-scatter optical light into narrow cones of a few degrees. Cassini observations of the jovian ring taken alone (Porco *et al.*, 2003) and in combination with other spacecraft and Earth-based observations of the ring (Throop *et al.*, 2004) have indicated that irregularly shaped, small ( $\mu\text{m}$ -sized) particles are more likely than spherical Mie scattering particles, at least for the rocky jovian ring particles. Because of the small particle size, diffuse rings are often most visible at high phase angles. Voyager images of Saturn's spokes and of abrupt brightness clumps in the F ring

(Showalter, 1998) indicate that features may be time-variable; charged-particle absorption signatures surrounding the F ring (Cuzzi and Burns, 1988) and ground-based images of transient events in the E ring (Roddier *et al.*, 1998) also imply that clouds may develop rapidly and then fade. To document and then to understand its causes, this time variability will require repeated imaging of some features throughout the mission.

Saturn's E ring, an extensive diaphanous cloud encircling Saturn and spanning the orbits of Mimas to Rhea, has two distinctive properties: its distinct brightness peak at Enceladus and its narrow size distribution, dominated by particles near a micron (Showalter *et al.*, 1991). Hamilton and Burns (1994) claim that, owing to resonance effects, E-ring particles move along elongated orbits; this hypothesis can be tested with measurements made by Cassini's dust detector. The same authors maintain that the resultant high-speed collisions into Enceladus sustain the ring. A corollary is that regions adjacent to other nearby moons should have enhanced ring intensity. The E ring's photometry and broad-band color need to be refined in order to tie down its unique and peculiar size distribution. Particles which are nearly spherical, mono-dispersed ice grains (as believed for the E ring constituents) will exhibit a strong polarimetric signature, which can be sought in images acquired through the ISS polarizing filters.

Saturn's G and D rings were discovered by Voyager but were the least studied by that mission. The former is tenuous, localized, and centered on orbital radius 168,000 km, far from any other known ring or moon. Its source is uncertain; small satellites in the vicinity will be sought. The particle size distribution is disputed (Showalter and Cuzzi, 1993; Throop and Esposito, 1998) and its firm identification will require broad phase coverage, with the diffraction lobe emphasized; polarimetry may also be useful. Saturn's innermost D ring was scarcely observed by Voyager (Showalter, 1996). The ring contains wave-like faint ringlets as well as two narrow rings. The ring's photometric properties are poorly constrained.

The band between the F ring and the outer edge of the A ring contains faint material whose optical properties vary with distance to Saturn (Murray *et al.*, 1997; Showalter, 1998), possibly giving clues to ring sources and sinks. Good photometry and color can clarify the causes. (Cuzzi and Burns, 1998) believe that the region immediately exterior to the F ring may have faint transient clumps, while others claim that it contains several small moons; it should be surveyed carefully. Cassini should target the region surrounding Atlas's orbit to seek a faint ring formed from the satellite's ejecta as Jupiter's gossamer rings seem to be (Burns *et al.*, 1999). Faint rings may also trail from the Lagrangian satellites of Tethys and Dione, especially following the controversial claim (Roddier *et al.*, 1998) of a time-variable cloud near one of Enceladus's triangular points.

Gaps in the main system, particularly across the Cassini Division and in the C ring, should be scrutinized to set upper bounds on the presence of any material, with the goal to understand the mechanism(s) that evacuate gaps.

### 2.3.6. *Proposed Observations*

Most investigations aimed at addressing these important issues require the highest imaging resolution possible. Outside the period of time immediately following the SOI, when Cassini is closest to the rings and cruising above them on the dark side at a distance only tens of thousands of kilometers (yielding a smear-limited resolution of  $\sim 100$  m), the highest imaging resolution obtainable on the rings anytime during the Cassini tour is  $\sim 1.0$  km. (For most of the tour, the NAC resolution on the rings ranges from  $\sim 1.0$  to 15 km/pixel; in the WAC, the range is 10–150 km/pixel.) Imaging the entirety of Saturn's rings at this resolution would present an impossible task: the total surface area of the rings, including both illuminated and unilluminated sides, is  $\sim 1200$  times the surface area of Titan. Consequently, high-resolution imaging observations have been carefully chosen and focused on regions expected to yield the greatest fundamental science. (The highest-resolution “clear filter” images of the rings taken by Voyager had a pixel scale of 4 km.)

Other investigations that require variable lighting and viewing geometries and only modest resolution have been planned either with the NAC taken at larger distances, or the WAC taken in close. Though not significantly different than Voyager's best resolution color images, with a scale of 25–30 km/pixel, Cassini's camera system has much broader spectral coverage, particularly in the UV and the near-IR, and its CCD is much more sensitive, with a larger dynamic range, than was Voyager's vidicon.

Thus, in all types of investigations – either those requiring relative or absolute, high-precision positional measurements or those requiring sensitive photometric and color measurements – we anticipate that Cassini images of Saturn's rings, with  $\sim 100,000$  planned over 4 years, will provide dramatic advances in our understanding of planetary rings.

Planned observations include the following:

- Approximately a dozen high-resolution (1–2 km/pixel) radial scans of the main rings taken at low-to-moderate solar phase angles will provide our best signal-to-noise imaging data on the finest-scale structure of the rings available to the ISS, including the irregular structure in the outer B ring.
- The radial variation of the amplitude of the opposition effect, a rapid brightening of the rings near zero phase angle, will be measured in several colors as the opposition spot passes diametrically across the rings.
- Observations taken during SOI may marginally resolve the “wakes” that are believed to produce the azimuthal asymmetry in the A ring (Figure 11) and will provide the highest resolution views of the rings during the whole tour.
- Moderate-resolution multicolor imaging of at least one complete ring ansa will be carried out in a wide range of viewing geometries in order to map out the way in which the rings' reflectivity ( $I/F$ ) varies with solar phase angle and with tilt angle (i.e., high or low elevation above the lit or unlit face of the rings). These observations, diagnostic of the nature of the particle surfaces and the particle



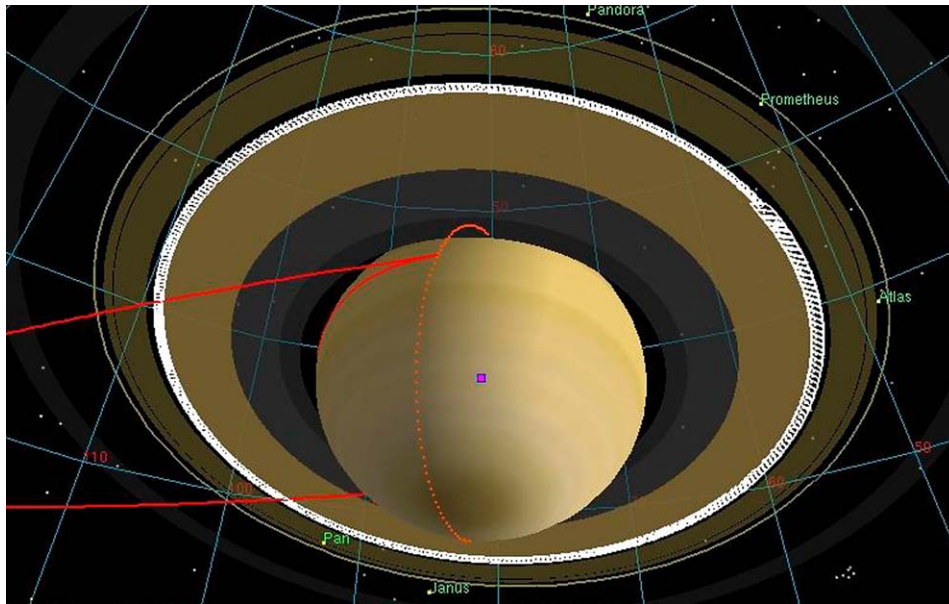


*Figure 12.* A typical azimuthal scan of a ring edge and gap (in this case, the outer B ring edge and inner Cassini Division) at moderate phase and high spacecraft latitude,  $-35^\circ$ . ISS will acquire observations like this on a dozen or so features in Saturn's rings for the purpose of searching for new moons, detecting edge waves and, in some cases, fully sampling the circumference and shape of eccentric rings.

disk characteristics, will also be used to characterize the azimuthal asymmetry in the A ring, search for its presence in other rings, and to probe the internal structure of the rings and the ring particle properties.

- Moderate-resolution radial scans using up to 15 filters to complement the higher spectral, but poorer spatial, capabilities of VIMS and CIRS in the composition of the ring particles, particularly the abundance and nature of the non-icy contaminants in different regions.
- Approximately a dozen or more high-resolution ( $\leq 3.5$  km/pixel)  $360^\circ$  scans of select features in the rings: the F ring, the Encke gap, the outer A and B rings edges, the Cassini Division, the major gaps in the C ring, the D ring, and select density waves in the rings to search for embedded moonlets and/or the small-scale signatures of their gravitational perturbations on surrounding ring material (Figure 12).
- Search for unseen satellites between the rings and the orbit of Hyperion.
- Imaging observations to measure the positions of, and refine the orbits of, satellites in the Saturnian system.
- Retargetable observations for orbit refinement and/or high-resolution morphology of newly discovered moons.

- Rapid ( $\sim 11$  s interval) time-lapse, moderate-resolution imaging sequences of the morning ansa of the rings in the hopes of capturing spoke formation; Movie sequences of the rings at low resolution to determine the periodicities in the appearance of spokes on the rings; Moderate-resolution spoke-tracking imaging campaigns to follow spokes to investigate spoke evolution.
- Imaging of the main rings at phase angles higher than those observed by Voyager will map out the abundance of sub-micron “dust” in the rings.
- Imaging of the diffuse rings (E, G and D), as well as some of the ring gaps (such as Encke) over a wide range of phase angle, including high phase, to constrain particle size and shape distributions.

### 2.3.7. *Combined Studies with Other Cassini Instruments*

Several dozen stellar (VIMS and UVIS) and radio (RSS) occultations by the rings will occur, spread over the 4-year mission, with a resulting radial resolution of 100 m. Many of these will penetrate and measure the optical thickness of the deepest portions of the B ring at these resolutions, something that Voyager was unable to do.

While occultations will provide the highest radial resolution available from Cassini at specific and limited longitudes on the rings, images can capture a continuous sweep of longitude. In this regard, these data sets are complementary. The combination of stellar/radio occultation data with imaging data will provide a powerful collection of information about the kinematical behavior of perturbed ring features, and their deviations from circularity, down to a precision of tens of meters for occultations, and down to  $\sim 1/4$  km for images.

Also, as with investigations of the surfaces of satellites, VIMS and ISS provide complementary results. Where VIMS can acquire high spectral resolution with low spatial resolution, determining far more precisely the composition of the material, ISS will provide the high-resolution context. Once the mapping of composition to ISS colors has been done by using the two instruments together, subsequent ISS color observations can be used to push compositional studies to higher resolution than is available with VIMS.

## 2.4. TITAN: SURFACE AND ATMOSPHERE

What we know of Titan today, on the threshold of Cassini’s orbital tour of Saturn, comes from more than a century of telescopic observations from the ground and low Earth orbit and from the Voyager encounters with Titan in the early 1980s. Owing to the ubiquitous haze enveloping the satellite and obscuring the surface and lower atmosphere to visible wavelength observations, most Voyager-era results were derived from the other spectroscopic and occultation experiments and not the imaging investigation.

Relevant to the Cassini ISS investigation are the facts that Titan has a thick, largely  $\text{N}_2$  atmosphere (mole fraction of  $\sim 95\%$ ) with a few percent  $\text{CH}_4$  and trace

amounts of other simple and some complex organics; surface temperature ( $\sim 94$  K), pressure ( $\sim 1.4$  bar) and near-surface lapse rate consistent with the presence of methane–ethane liquid surface reservoirs; a troposphere with a methane mixing ratio and lapse rate likely to produce methane clouds a few kilometers above the surface; a 200 km thick haze layer with a lower boundary in the stratosphere,  $\sim 100$  km above the surface; an upper atmosphere (with wind speeds  $\sim 100$  m/s which is believed to rotate faster than the surface, possibly giving it a super-rotator-like general circulation pattern like that of Venus; methane photolysis in the upper atmosphere likely to result in polymerized organics which rain down and coat the surface, collecting in depressions (such as craters). With such a complex environment, dominated by a thick atmosphere with a condensable material, it is possible that the Titan terrain exhibits geologic features produced by wind, rain, and fluvial erosion – channels, gullies, ‘waterfalls’, lakes, shorelines, etc. – as well as the usual tectonic and impact-produced morphologies seen on the other icy satellites.

Though Voyager images of Titan were unsuccessful in revealing the details of its surface – (however, see Richardson *et al.*, 2004) – we are hopeful that major and seminal scientific advances will result from the Cassini ISS investigation of Titan’s surface and lower atmosphere for two primary reasons. First, it has been demonstrated from both ground-based and HST imaging investigations, and now Cassini ISS approach observation of Titan (Figure 2), that the surface and troposphere of Titan can be remotely sensed in the near-IR spectral regions in between the methane absorption bands that dominate its spectrum (Lemmon, 1994; Smith *et al.*, 1996). In these inter-methane-band ‘windows’, the dominant source of opacity is scattering by stratospheric haze, which decreases in strength with increasing wavelength in the near-IR. Second, the Cassini ISS has been equipped with special capabilities for penetrating the hazy atmosphere, among them IR filters and filter combinations specially designed to match the inter-methane-band windows, and IR polarizers to cut down the light scattered by the overlying haze. Use of these polarizers will have the effect of increasing (in the relative sense) the percentage of photons reaching the cameras that were last reflected from the surface and unattenuated by the overlying atmosphere. None of these circumstances guarantees success in completing the imaging investigations that are described later (some of which are aimed at very high resolution of the Titan surface which may be hampered by overlying haze). But as Cassini makes its way towards Saturn, optimism remains high.

#### 2.4.1. Meteorology

Titan’s 16-day rotation period appears to place its atmosphere into the same slowly rotating dynamical regime that characterizes the general circulation of Venus (Del Genio *et al.*, 1993, 1996; Allison *et al.*, 1995). The dominant features of Venus’ atmospheric circulation are its surprising zonal super-rotation and extensive cloud-level Hadley circulation. Similar features are expected on Titan (Hourdin *et al.*, 1995), but no wind measurements exist to date because (a) prior to Huygens, Titan’s atmosphere has not been probed in situ; (b) to date, imaging of Titan’s clouds,

primarily at wavelengths sensing its stratospheric haze, has revealed no features suitable for tracking winds. Nonetheless, indirect evidence from Voyager IRIS brightness temperature profiles (Flasar *et al.*, 1981) and stellar occultation estimates of oblateness (Hubbard *et al.*, 1993; Sicardy, 1992) strongly suggest the presence of super-rotation at and above the tropopause.

A primary objective for Cassini ISS at Titan, therefore, is to map Titan's global wind field at the tropospheric levels where its atmosphere interacts with the surface angular momentum source. Such measurements would provide a global context for the local vertical profile of wind to be measured by the Huygens Probe Doppler Wind Experiment (Bird *et al.*, 2002), and if sufficiently extensive, might shed light on the mechanism(s) sustaining the super-rotation. On Venus, planetary-scale transient waves due to barotropic instability (Rossow and Williams, 1979), solar-fixed thermal tides (Ingersoll and Pechmann, 1984), and small-scale gravity waves (Young *et al.*, 1987) have all been hypothesized as significant contributors to the super-rotation; evidence for any of these processes operating on Titan would greatly advance our understanding of the slowly rotating regime. Specifically, knowledge of the latitudinal profile of zonal wind would constrain the efficiency of lateral angular momentum and potential vorticity mixing on Titan.

To track Titan cloud features, we must see below the featureless stratospheric haze into the troposphere, where methane clouds may exist in regions of rising motion. At the longest ISS wavelengths, we expect to see through the haze and view Titan's troposphere and surface (see Section 2.4.3). We therefore plan to image Titan in the near-IR using filters IR2/IR1 (827 nm), CB3 (938 nm), IR4 (1002LP nm), and IR5 (1028LP nm). To improve tropospheric visibility, the NAC carries an IR polarizer that can be used in combination with CB3 (938 nm), while the WAC carries two orthogonal IR polarizers that can be used with CB3 (938 nm), IR4 (1001LP nm), or IR5 (1028LP nm). We will image Titan, initially at intervals of a few hours, within 1 day of closest approaches to allow for detectable cloud displacements. In the event that small-scale features can be seen, we also plan to image at shorter time intervals to capture the evolution of these features.

Although there is uncertainty in Titan's methane abundance and the availability of condensation nuclei, ground-based observations have detected possible methane clouds (Griffith *et al.*, 1998) and transient clouds have been imaged in Titan's south polar region (Roe *et al.*, 2002; Brown *et al.*, 2002). Given sufficient methane abundance at the surface, Titan's temperature profile is steep enough to be unstable to moist convection and thus we anticipate that upper troposphere methane cirrus, created from the outflow of convective updrafts, might be the most common type of cloud feature, but visible only on the small spatial scales that ISS will be able to resolve. If convection does exist, its presence may be difficult to detect because infrequent convection is probably sufficient to remove the required energy from Titan's surface. Indirect evidence for methane convection might exist in the form of lightning. If lightning occurrence can be detected and mapped, it effectively will serve as a tracer for large-scale vertical motions such as the upwelling branch of the

Hadley cell. The H-alpha filter (HAL) on the NAC may be used to detect lightning flashes associated with methane ( $\text{CH}_4$ ) dissociation in long-exposure night-side images taken several hours before or after Titan closest approach; the clear filter may also be used to detect faint lightning flashes. In addition, we will seek lightning signatures of NII at 820 nm by overlapping the IR1 and IR2 filters.

#### 2.4.2. *Photometric and Polarimetric Studies of Titan's Atmosphere*

Deposition of solar radiation in the atmosphere and radiative interaction with tides or other wave phenomena is thought to be at the root of the mechanism that drives circulation. It is therefore important to understand radiative heating and cooling. The Descent Imager Spectral Radiometer (DISR) on the Huygens Probe will provide the sole Cassini direct measurement of the internal radiation field, but at only one location on the planet. The ISS can provide information on the radiation field at other locations on Titan in the same manner it will do for Saturn: by using photometry and polarimetry to infer the optical and physical properties, and the vertical and horizontal distributions, of aerosols, and using these parameters in studies of radiative energy balance. Photometry and polarimetry of Titan will also be important for understanding other microphysical processes at work in the stratosphere.

The measurements to be made to infer particle properties and distributions are listed in Tables III–V. Only the first two techniques (limb profiling and methane-band imaging) listed in Table V will be used at Titan. (The others techniques in Table V utilize the molecular Rayleigh scattering contribution to optical depth, which is negligible for Titan.)

Titan's disk nearly fills the NAC frame at a distance of  $10^6$  km, and that is approximately the range from which the ISS will image Titan for haze studies. The spatial resolution of the NAC at that distance is 6 km/pixel, which is significantly smaller than a scale height. Aerosol profiling can be done over the entire illuminated limb of Titan in a single image. Images at different wavelengths will yield the wavelength dependence of the haze as a function of location. As for Saturn we will target special opportunities such as times when a bright star is near the limb. Images of Titan in which the dark limb can be seen against the bright disk of Saturn can be used to profile optical depth on the night side. As for Saturn, images at many phase angles and many wavelengths and with polarizing filters will be used together to provide new and powerful constraints on particle size, shape, and distribution, and in turn on microphysical models of haze production and in studies of energy balance.

#### 2.4.3. *Visibility of the Surface*

It was long believed that Voyager ISS did not see the surface of Titan, but recent work (Richardson *et al.*, 2004) has shown that the surface was detected in the orange filter. The Voyager surface detection is very marginal, perhaps 2:1 SNR, but gives us reason for guarded optimism for the capabilities of Cassini ISS. The Voyager orange filter, centered at about 590 nm, covers the first (shortest wavelength) of nearly

six inter-methane-band windows from 600 to 1000 nm (Section 3). Optical depth in these windows, due to stratospheric haze scattering, decreases with increasing wavelength (Lemmon, 1994), so each of the other methane windows (accessible to Cassini ISS but not Voyager) should provide improved images of the surface. Furthermore, the total S/N of the Voyager image (at the top of Titan's atmosphere) is only  $\sim 50:1$  rather than  $\sim 200:1$  expected from Cassini ISS. Finally, Cassini ISS includes IR polarizer filters, which reduce the effects of haze at moderate phase angles. Based on the Voyager results and the spectrum of Titan, we expect to be able to detect the surface of Titan through the RED (650 nm), IR1 (752 nm), IR2 (862 nm), IR3 (930 nm), CB2 (750 nm), CB3 (938 nm), IR4 (1002LP nm), and IR5 (1028 nm) filters. However, major uncertainty persists as to the quality and resolution of these surface detections.

We are most optimistic that surface details will be visible to ISS in the continuum filter centered at 938 nm (filter CB3), especially since surface features on Titan have been seen on approach to Saturn with the Cassini ISS utilizing this particular filter (Figure 2). HST has shown that contrast from the surface of Titan can be seen through a broad-band filter similar to IR3 (Smith *et al.*, 1996), but CB3 is centered in the middle of the methane window and should be superior. Lemmon (1994) used constraints from observations of Titan's geometric albedo as well as spacecraft observations of reflected intensity and polarization to estimate haze optical depth at many wavelengths. In order to fit the weak methane bands in the near-infrared, he included a plane-parallel cloud in the lower atmosphere with optical depth 0.46, independent of wavelength. The overlying stratospheric haze in his model has an optical depth that decreases with wavelength. The sum of the two optical depths in the 938 nm methane window region is close to 1.0.

Although there are uncertainties associated with the model, it is reasonable to ask how well ISS can expect to see contrast features in the lower atmosphere or on the surface with an overlying cloud and haze optical depth of 1.0. We are most interested in features with small spatial scales (the NAC pixel spacing corresponds to about 6 m for the closest passes,  $\sim 950$  km above the surface. The contrast at large spatial scales seen in Voyager images and HST images (Smith *et al.*, 1996) can be carried by the diffuse radiation field. However, at small spatial scales (smaller than the vertical distance of the scattering layer from the surface, roughly 200 km), the contrast must be carried by photons that traverse the atmosphere without suffering a scattering event.

The fraction of the light leaving the surface which emerges at the top of the atmosphere without suffering a scattering is  $e^{-1/\mu}$ , ignoring atmospheric curvature, where  $\mu$  is the cosine of the emission angle. The critical question is: how much contrast is seen at the top of the atmosphere for a given surface contrast? Here, contrast is defined as (maximum intensity – minimum intensity)/maximum intensity. The problem is exceedingly difficult if one is trying to estimate contrast induced by topographic slopes. Here, we take the easier route and assess contrast at the top of the atmosphere for a given albedo contrast on the surface.

A plane-parallel model atmosphere would probably suffice for an estimate of contrast near the center of the disk. However, some of the close approaches to Titan will be near the terminator where the atmospheric curvature is important. Therefore, we have constructed multiple-scattering radiative transfer models with the appropriate curvature of Titan's atmosphere. The multiple-scattering model takes full account of multiple scattering in a spherical shell atmosphere containing particles with the asymmetric phase functions thought to be appropriate for Titan (from Lemmon, 1994). It does not take into account polarization except for single scattering. We were able to estimate the effects of Titan's strongly polarizing haze layer by calculating the radiation field carried by singly scattered photons that polarize the light in the way that fractal aggregates do: highly positively polarizing at  $90^\circ$  scattering angle (West and Smith, 1991; Lemmon, 1994). Our estimate of how much the contrast is improved by the use of a polarizing filter is conservative in the sense that light from photons scattered more than once is assumed to be unpolarized. We consider the surface to depolarize the light and to diffusely reflect according to Lambert's law.

In order to estimate contrast at the top of the atmosphere we performed two calculations, each having a spherically symmetric surface and atmosphere. The first calculation had a surface albedo of 0.1; the second, a surface albedo of 0.4. The emerging contrast for the small-scale features was then given by the contrast in the directly transmitted beam divided by the average of the total reflected light from the two runs.

The calculations can be summarized as follows. For nadir viewing near the sub-solar point a surface contrast of 30% at small spatial scales will produce top-of-atmosphere contrast of 6.3% for an average surface albedo of 0.1. The same surface contrast will produce a top-of-atmosphere contrast of 12% if the average surface albedo is 0.4. The light is unpolarized for nadir viewing of the sub-solar point so the contrasts reported above apply to the polarizing filters and non-polarizing filters equally. Near the terminator the top-of-atmosphere contrasts would be 2.6 and 7.1% for the non-polarizing filters and average surface albedos 0.1 and 0.4, respectively. With a polarizer filter the contrast increases to 3.3 and 8.4%. The signal/noise ratio in a single pixel exposed to 70% full well is expected to be 260. The Modulation Transfer Function of the Cassini ISS at the Nyquist frequency is approximately 15%, which reduces the contrast over a few pixels by a factor of 0.15. If the atmospheric model is correct, we expect to detect features at the Nyquist frequency (corresponding to two pixels or 20 m per cycle at the closest Titan flybys) with S/N greater than 10 if the top-of-the atmosphere contrast is 25%. The corresponding surface contrast would need to be near 100%. Features with larger scales or features near the top of the tropospheric cloud level can be detected at lower contrast. Features with horizontal scales larger than  $\sim 5$  pixels should be detectable at surface contrast levels near 30%.

Although Cassini provides an extremely stable platform for long-exposure images, smear remains a significant concern during the very close 'targeted' satellite

flybys, including the close flybys of Titan. Cassini's on-board Inertial Vector Propagation (IVP) system can precisely track a target on Titan from any range greater than  $\sim 1500$  km, but the changing range to Titan introduces significant smear in long exposures ( $> 10$  s) when the range is less than  $\sim 10,000$  km (within  $\sim 30$  min of closest approach). Long exposures are needed to ensure a high S/N at the top of the atmosphere, especially in the CB3 filter, in order to achieve an adequate S/N on the surface. Use of  $2 \times 2$  pixel binning and nearly four times shorter exposure times alleviates this problem, but with a halving of pixel scale. Given the low contrast expected on scales of a few pixels,  $2 \times 2$  binning should result in little loss of available information, and may provide our best imaging mode for Titan's surface. Another option is to image at shorter wavelengths where we can use shorter exposure times than with the CB3 filter. Most promising is the IR1/IR2 combination, which produces a medium-width band center on the 825-nm inter-methane-band window (Section 3). Exposure times for the IR1/IR2 filter combination can be a factor of  $\sim 10$  shorter than for the CB3/Clear combination. However, we cannot combine this two-filter bandpass with an IR polarizer filter. The IR1 filter covers several methane windows and could enable imaging of the surface with exposure times  $\sim 100$  times shorter than with CB3, but with even less contrast on small-scale surface features.

#### 2.4.4. Titan Surface Science

As for all the other satellites of Saturn, a major objective of the ISS for Titan is a determination of its geologic and thermal history. Titan may have initially been largely melted in its outer several hundred kilometers by accretional heat (Schubert *et al.*, 1981), producing a deep global ocean of water ( $\text{H}_2\text{O}$ ) or a water–ammonia mixture ( $\text{H}_2\text{O}$ – $\text{NH}_3$ ). The deep interior initially may have been a largely undifferentiated mass of ice and rock. With the cessation of accretion, an outer layer would have cooled and solidified. Simultaneously, the interior would have warmed due to radio nuclides in the silicates, and perhaps differentiated to form a rocky core and an icy mantle. Based on the evidence for subsurface water in the icy Galilean satellites (Kivelson *et al.*, 2004), most workers now expect a mantle of liquid  $\text{H}_2\text{O}$  to have persisted on all large icy satellites such as Titan (Schubert *et al.*, 2004).

If methane ( $\text{CH}_4$ ) clathrate was present initially, it could be expected to dissociate in the deep interior, releasing methane, which would subsequently tend to rise towards, and possibly extrude out onto, the surface, where it might have formed bodies of liquid and/or evaporate into the atmosphere. (The presence of ammonia ( $\text{NH}_3$ ) might provide a source of material that could also rise to the surface cryovolcanically (Kargel *et al.*, 1991).) A reasonable model for the present internal structure of Titan, then, has a silicate core, a deep mantle of water–ammonia ( $\text{H}_2\text{O}$ – $\text{NH}_3$ ) ice, a subsurface “ocean” of  $\text{H}_2\text{O}$ – $\text{NH}_3$  liquid, upper mantle of  $\text{H}_2\text{O}$  ice that may contain  $\text{CH}_4$  clathrate, and a thin uppermost layer that could be rich in liquid methane and other hydrocarbons (Stevenson, 1992; Lunine *et al.*, 1998; Grasset *et al.*, 2000).



Geologic activity seems likely on Titan. Ganymede shows evidence for tectonism and resurfacing and Callisto does not (Smith *et al.*, 1979a,b); Titan probably contains more volatile material than either and is correspondingly more likely to have been active. Evidence for geologic activity comparable to or more extensive than that on Ganymede would suggest significant tidal heating sometime in Titan's history. Indeed, many of Saturn's small inner satellites, which may contain lower concentrations of volatiles than Titan have been active (Smith *et al.*, 1981, 1982). On most icy satellites, extensional features appear to dominate the resurfacing (Squyres and Croft, 1986). The primary sources of stress are probably internal phase changes and solid-state convection – both likely on Titan.

Evidence for resurfacing on icy satellites ranges from flat, smooth, crater-poor regions (on Enceladus (Squyres *et al.*, 1993) and Ganymede (Parmentier *et al.*, 1982)) to thick, lobate flows indicating emplacement of fluid with a high viscosity or yield stress (on Ariel (Jankowski and Squyres, 1988) and Triton (Smith *et al.*, 1990)). This variety results from a range in the rheologic properties of materials, which may have been extruded in solid, partially molten, or liquid form. Liquid or slush is favored on the small Saturnian satellites because of their low gravity and small buoyant forces (Stevenson, 1982), but extrusion of warm ice on a satellite as large as Titan is possible. Constraints may be placed on the rheology and extrusion state of flows if their thickness can be determined (Jankowski and Squyres, 1988; Melosh *et al.*, 1989; Schenk, 1991), either by observation of topography or by measurement in subsurface profiles. Resurfacing on Titan could lead to unusual effects. For example, buoyancy caused by extrusion beneath liquid could lead to enhanced flow thicknesses. Also, extrusion in the presence of ongoing sedimentation could produce a sequence of interbedded ice and organic layers.

Of the many organics produced in Titan's atmosphere (Raulin and Owen, 2002), most are slightly to negligibly soluble in any surface liquid that may be present. Under the physical conditions present on Titan's surface, they are also generally solid, with the exception of propane ( $C_3H_8$ ), and more dense than a liquid mixture of ethane–methane–nitrogen ( $C_2H_6$ – $CH_4$ – $N_2$ ). One can therefore expect a slow accumulation of solid organic sediment at Titan's surface. If no liquid is present, this solid material will cover Titan's icy surface; if liquid is present, the material might accumulate as sediment in topographic basins. The most abundant insoluble molecules produced by atmospheric chemistry are acetylene ( $C_2H_2$ ), hydrogen cyanide (HCN), methyl acetylene ( $C_3H_4$ ), methyl cyanide ( $CH_3CN$ ), and other alkynes and nitriles. The  $C_2H_2$  alone should accumulate to form a layer  $\sim 100$  m thick (Yung *et al.*, 1984; Sagan and Thompson, 1984). Other solids expected include polyacetylene (Allen *et al.*, 1980; Yung *et al.*, 1984) and complex nitrogenous organic polymers.

Impact craters are probes of satellite crusts, indicators of surface ages and thermal history, and provide information on impactor populations and atmospheric properties over time. Titan's atmosphere should shield the surface from small projectiles and decelerate and ablate larger comets (Ivanov *et al.*, 1997; Engel *et al.*,

1995; Lorenz, 1997; Artemieva and Lunine, 2003). A first-order question to be answered by Cassini is whether Titan's surface is heavily cratered and old or whether there has been extensive resurfacing since an early period of heavy cratering. If Titan's surface is as old as that of Rhea and Hyperion, there should be  $\sim 200$  craters larger than 20 km diameter per  $10^6$  km<sup>2</sup>, close to a saturation density (Engel *et al.*, 1995; Lorenz, 1997). If all of Titan's surface has such a spatial density of large craters similar to Callisto's, then it may have experienced little differentiation and endogenic geologic activity. Observation of terrains with substantially fewer craters will be our first indication that Titan has experienced an extended period of geologic activity, perhaps similar to Ganymede or Triton. The morphologies of the large craters and multi-ring structures may provide clues to the presence or depth to subsurface water (Turtle and Pierazzo, 2001; Schenk, 2002).

Titan's cold temperatures would tend to inhibit the crater relaxation observed on Ganymede and Callisto, while NH<sub>3</sub> hydrate, if present, could soften the ice and enhance relaxation (Durham *et al.*, 1989). An impact regolith on Titan might be coarser grained than on other satellites because small impactors responsible for most near-surface comminution and mixing will be stopped by the atmosphere. With continuous deposition of organic solids, cratering could lead to a sequence of interbedded icy ejecta and organic sediment layers. If liquid is present on the surface, the effects on cratering could be substantial. Normal regolith formation would not be expected. A liquid layer with a depth more than about 40% of the depth of a normal transient cavity should be sufficient to inhibit formation of a crater on its floor (Gault and Sonett, 1982). Even much shallower liquid should be adequate to produce unusual crater forms, with shallow floors and little or no rim (Gault and Sonett, 1982).

If liquid is present on Titan, it could promote erosion. One possible mechanism arises from the solubility of H<sub>2</sub>O in liquid CH<sub>4</sub>–C<sub>2</sub>H<sub>6</sub>–N<sub>2</sub> (Rebiai, 1984). Dissolution of ice over long periods could alter immersed topography (Lunine, 1985b). Dissolution could, of course, be limited by saturation, so one would expect it to be most effective where there is flow of unsaturated fluid, perhaps as tidal currents (Sagan and Dermott, 1982). On the order of 100 m of erosion, could occur in 10<sup>9</sup> years if not inhibited by sediment accumulation. Patterns of erosion and deposition could be complex, influenced by circulation patterns, saturation conditions, and sediment distribution. Dissolution could be promoted by fracturing and zones of weakness in the ice, and it is even possible that caverns, like those formed by aqueous dissolution of carbonates on Earth, could develop. Also, if methane rain occurs (Toon *et al.*, 1988) and falls onto a dry surface we could see physical erosion, development of drainage systems, and even a true 'hydrological cycle'. A number of workers have speculated that the bright region on Titan's leading hemisphere may be a high-standing area of water ice washed clean of dark atmospheric sediment by methane rain. Multi-spectral observations suggest that the leading hemisphere has a purer and/or finer-grained ice surface than the darker hemisphere (Griffith *et al.*, 2003).

Evidence for smooth surfaces with specular reflections have been detected from Earth-based radar (Campbell *et al.*, 2003). If lakes or rivers of liquid organics are present on Titan's surface and if the overlying particle optical depth is not greater than about 2, ISS will be able to image the glint pattern in the specular direction. The size of the glint pattern is diagnostic of the amplitude of capillary waves driven by wind. The relationships between surface slope and wind velocity derived by Cox and Munk (1954) are often used for the Earth. The relationship between wind and surface slope will be different for Titan because of the differences in gravity and viscosity of the liquid and air. Glint reflection is typically much stronger than reflection from diffuse surfaces. Even very small bodies of water were easily detected as specular bright spots in Galileo images of the Earth's land surface. Polarization measurements of specularly reflected light may constrain the refractive index of the liquid. Information to be obtained in this way will depend on the surface coverage of liquid and on our ability to disentangle the effects of atmospheric scattering – a much more severe problem than for the earth.

Finally, even if no liquid is present on the surface, eolian redistribution of sediment or ice might occur. The wind regime at the surface of Titan is unknown. Calculated meridional winds are small, but zonal winds of 25 m/s have been estimated in the lower troposphere (Flasar *et al.*, 1981). Given the high atmospheric density, low gravity, and likely small size of sediment particles, eolian transport may be common. Eolian redistribution could result in an uneven surface distribution of organic sediment, perhaps like that produced by eolian transport of fine dust on Mars.

According to models by Tokono and Neubauer (2002), Saturn's gravitational tide on Titan's atmosphere has a large influence on the meteorology down to the surface. The surface pressure oscillates up to 1.5 Pa through the orbit, with strong temporal and spatial variation in the atmospheric flow near the surface. The superposition of annual thermal latitudinal pressure gradients produces a surface wind pattern of equatorward flow and high-latitude whirls. Meridional tidal winds can be as fast as 5 m/s, perhaps sufficient to produce streaks of fine-grained materials on the surface with a unique global pattern.

#### 2.4.5. *Strategy for Titan Imaging*

For planning purposes, we have placed Titan observations by ISS into the following seven categories:

- Movies or time sequences will be acquired when Titan fills from half to all of the FOV (NAC when distant; WAC at lesser range), to monitor atmospheric features. Low phase angles are favored.
- Photometry observations are planned to image Titan at a range of phase angles through many filter combinations to study atmospheric properties.
- Full-disk mosaics ( $3 \times 3$  to  $5 \times 5$  images) will be taken in several colors for surface and atmospheric studies.

- Global surface mapping at medium resolution (500–1000 m/pixel) is planned from many passes. We expect to achieve  $\sim 70\%$  global coverage at 500–1000 m/pixel, and can fill most gaps at resolutions of a few kilometers/pixel.
- Regional mapping (200–500 m/pixel) will cover areas of interest, including repeat coverage from different viewing angles for stereo imaging of the topography.
- High-resolution imaging will sample terrains at scales of 12–200 m/pixel, covering  $\sim 10\%$  of Titan's surface. Low phase and emission angles are favored for the global, regional, and high-resolution observations. Because the surface of Titan is almost unknown, we are planning 'retargetable' mosaics at regional and local scales to be repositioned after we have mapped the surface at scales of a few kilometers or better. A set of WAC images with filters for atmospheric studies will be acquired along with NAC surface observations to model and remove atmospheric effects.
- Night-time observations will be acquired to search for lightning and aurorae.

In addition to these categories, we will also have observations that ride along with other experiments such as VIMS, CIRS and UVIS.

#### 2.4.6. *Combined Studies with Other Instruments*

Synergistic studies of Titan by Cassini/Huygens experiments will be especially important for the study of Titan (Lunine and Lorenz, 1996; Lunine and Soderblom, 2002). Combined observations and analyses between the orbiter instruments ISS and VIMS, CIRS, UVIS, and RADAR, as described earlier for other satellites, will be especially important because of the challenges presented by the presence of a dense atmosphere. The atmospheric haze will limit ISS to imaging the surface and lower atmosphere in only a few bandpasses but its capabilities for high spatial resolution and global mapping dovetail nicely, for example, with those of VIMS which observes farther into the near-IR where stratospheric haze optical depth is less. Simultaneous imaging of Titan in regions of methane cloudiness should enhance both experiments' ability to place local cloud events on Titan into a large-scale perspective, as well as allow ISS to model the effects of the atmosphere on surface images through retrieval of atmospheric structure from VIMS data.

In surface imaging, ISS will provide primarily morphologic and albedo/contrast information, while VIMS will add compositional mapping of the surface. RADAR altimetry can help to control regional tilts in ISS stereo models. Imaging by ISS will be important to place the narrow RADAR imaging strips into regional context, and to image these locations at higher spatial resolution. The subsurface information returned by RADAR could be especially interesting, combined with the high-resolution ISS images and VIMS spectral image cubes. The most accurate maps of Titan will require a joint solution utilizing Radar (SAR) and ISS images.

We expect that ISS images of Titan will be important for the choice of targets by other experiments, especially VIMS. Likewise, observations by VIMS, RADAR,

and perhaps CIRS will influence targeting by ISS. There will be particular challenges if the lower atmosphere is patchy and variable, or if the surface is geologically active and temporally variable.

The DISR on the Huygens probe will make extensive and detailed measurements of a very small region on Titan as it descends through the atmosphere (Tomasko *et al.*, 2002). It will image the surface and atmosphere from near-nadir to above the horizon. Its solar aureole cameras will measure light scattered from the sun at forward angles to within a few degrees of the sun and in horizontal and vertical polarization states. Its visible and near-infrared spectrometers will provide information on the spectral content of the internal radiation field and surface. These measurements will be invaluable to ISS. The DISR observations can be used as ‘ground truth’ for ISS retrievals of surface features, aerosol optical depth and aerosol properties as a function of altitude. They will help the ISS team assess the information content and quality of the retrievals which will be carried out on a global scale with the help of other orbiter data as mentioned earlier. Orbital imaging at the highest possible spatial resolution of the region observed by DISR is a high priority.

### 3. Instrument Characteristics and Capabilities

#### 3.1. HISTORY OF THE CASSINI ISS DESIGN

The origin of the Cassini camera dates back to the NASA/JPL Mariner Mark II program that called for the development of a series of common spacecraft to explore the outer solar system in the post-Voyager era. One main feature of this design, relevant to imaging investigations, was a high-precision scan platform (HPSP) for supporting the optical remote sensing instruments. In the early 1980s, the now extinct Comet Rendezvous/Asteroid Flyby (CRAF) mission and Cassini were identified as the first two missions of this program.

In 1984, an Instrument Development Team (IDT), led by Dr Joseph Veverka of Cornell University, was appointed by NASA to help define an imaging system for CRAF and subsequent Mariner Mark II missions. In 1988, this task was expanded specifically to include Cassini and the emphasis of the IDT became the definition of an imaging system that would meet *all* of the scientific requirements of both missions. The IDT recommended the following system characteristics:

- Dual focal lengths: A NAC for high-resolution studies with a maximum focal length consistent with the projected pointing stability of the Mariner Mark II platform, and a WAC, like Voyager but unlike Galileo, for context and broad spatial coverage with a FOV six to eight times larger than the NAC.
- Broad and identical spectral range in *both* cameras from 1100 nm down to the near-UV at 200 nm (compared to 300–650 nm on Voyager, and 350–1100 nm on Galileo).

- Improved filter wheel design to accommodate more than the traditional (Voyager and Galileo) eight filter slots, in order to exploit the increased spectral range and the known richness of cometary emission spectra for CRAF, and compositional diagnostics of near-IR spectra of ices in comets and at Saturn.

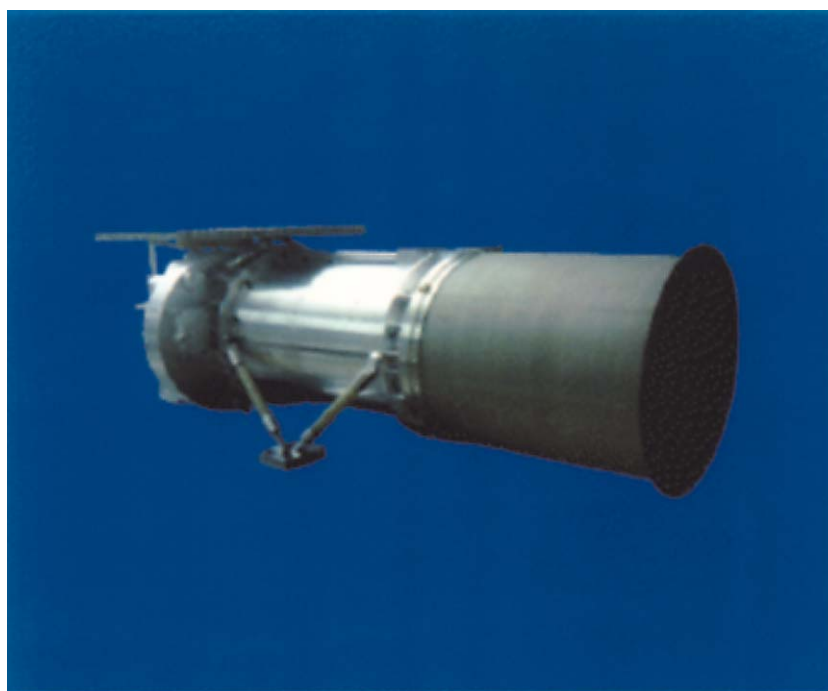
The narrow-angle design, essentially the Cassini NAC of today, evolved into a 2-m focal length,  $f/10.5$  Ritchey-Chretien telescope, extending from 200 to 1100 nm with a dual filter wheel system similar in design to that used in the HST's Wide Field Planetary Camera (WFPC) and capable of carrying 24 filters. To date, this is the longest focal length framing camera flown on a planetary mission. Both Voyager and Galileo had 1.5 m focal length cameras. The longest focal length to date (3.5 m) belongs to the MOC camera on Mars Global Surveyor (Malin *et al.*, 1992). MOC is a "push-broom" system with a single-line CCD, rather than a two-dimensional array, having a linear FOV that is 'pushed' along the target by the translational motion of the spacecraft.

The complementary wide-angle design initially developed for Mariner Mark II was to be a  $f/2.5$  Schmidt-Cassegrain reflector with a 0.3 m focal length, a  $2.3^\circ$  square FOV (compared to  $0.35^\circ$  for the NAC), and designed to utilize a dual filter wheel system carrying 14 filters covering the spectral range from 200 to 1100 nm. Although this original WAC design met *all* the scientific requirements of CRAF and Cassini, it was deemed too complex, heavy, and costly. By the time the Cassini Announcement of Opportunity was published in 1989, the Cassini WAC had evolved into a less expensive  $f/4$  refractor, with a 0.25 m focal length, a  $2.8^\circ$  FOV and a less desirable lower wavelength limit of 350 nm (unfortunately sacrificing the near-UV response).

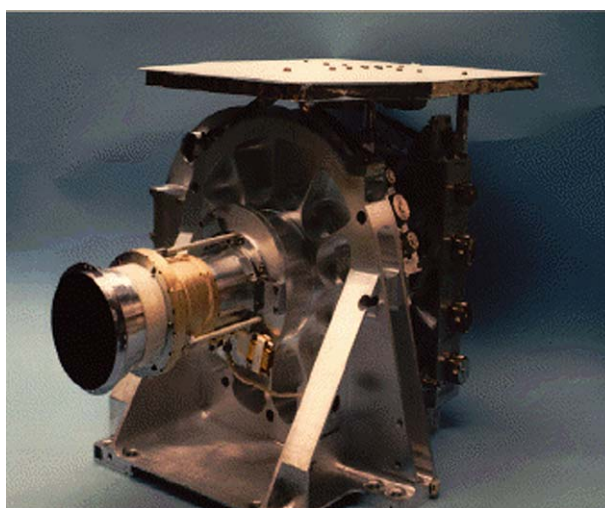
In November 1990, the Cassini Imaging Science team was selected (Table I) and it was left to this group to oversee and participate in the development of the ISS by JPL. As part of a serious cost reduction to the CRAF/Cassini program in 1992 that resulted in the termination of CRAF as well as the deletion of the Cassini HPSP and the placement of all Cassini remote sensing instruments directly onto the body of the spacecraft, the Imaging Team, in collaboration with the JPL instrument engineers, decided to abandon the WAC optical design to save money and replace it with spare Voyager-era wide-angle optics. The instrument, which is the present Cassini WAC, became an  $f/3.5$  color-corrected refractor, with a 200 mm focal length and a  $3.5^\circ$  square FOV, fronting a new dual filter-wheel assembly and focal plane. The spectral range was limited to 380–1100 nm, spanned by 18 filters.

### 3.2. GENERAL INTRODUCTION TO CAMERA CHARACTERISTICS

The Cassini ISS consists of two fixed focal length telescopes called 'cameras' (Figure 13). The NAC is 95 cm long and 40 cm  $\times$  33 cm wide; the WAC is 55 cm long and 35 cm  $\times$  33 cm wide. Both camera systems together have a mass of 56.9 kg. They sit on the Remote Sensing Palette (RSP) (Figure 14), fixed to the body



(A)



(B)

*Figure 13.* Photographs taken of the flight models of the Cassini (A) Narrow-Angle Camera Head Assembly and (B) Wide-angle Camera Head Assembly.

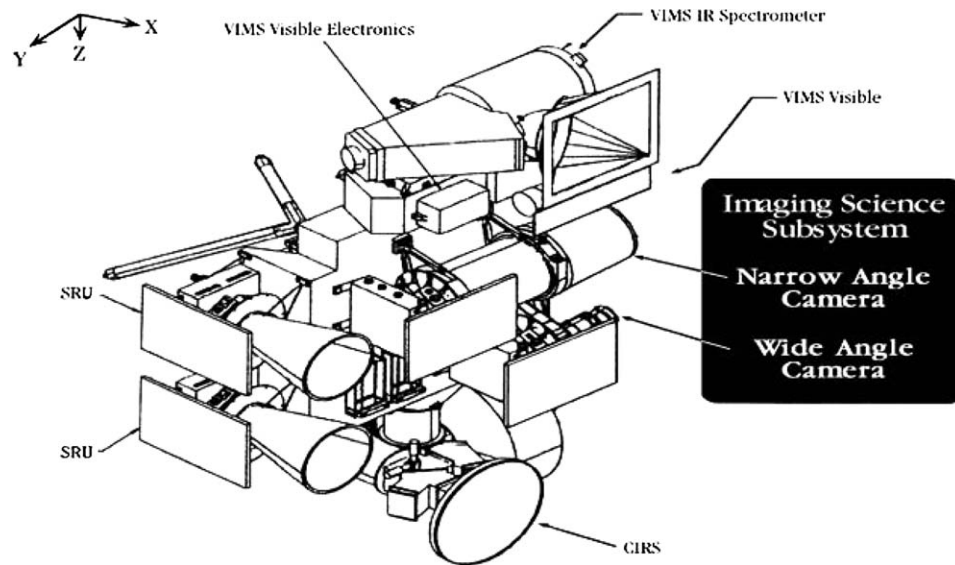


Figure 14. The layout of the optical remote sensing instruments, including the narrow and wide-angle cameras of the ISS and the Stellar Reference Units (SRU), on the Remote Sensing Palette of the Cassini Orbiter spacecraft. The spacecraft coordinate system ( $X$  s/c,  $Y$  s/c,  $Z$  s/c) is also indicated in the upper left (Section 3.6.1).

of the Cassini Orbiter, between the VIMS and the CIRS, and above the Ultraviolet Imaging Spectrometer. The apertures and radiators of both telescopes are parallel to each other. Figure 15 illustrates the FOVs of the NAC and WAC and those of the other remote sensing instruments on the palette.

The cameras are identical, except in the design of the optics and the number of filters. Each has its own set of optics, mechanical mountings, CCD, shutter, filter wheel assembly, temperature sensors, heaters, various control electronics, Engineering Flight Computer (EFC), and Bus Interface Unit (BIU) to the central spacecraft Command and Data System (CDS) (Figure 16). The electronics that control each camera consist of two parts: sensor head subassembly and the main electronics subassembly. The Sensor Head electronics supports the operation of the CCD detector and the preprocessing of the pixel data. The Main Electronics provide the power and perform all other ISS control functions, including generating and maintaining internal timing which is synchronized to the CDS timing of 8 Hz, control of heaters, and the two hardware data compressors. The Cassini EFC is a radiation-hardened version of IBM's standard, general purpose MIL-STD-1750A 16-bit computer and is the ISS processor that controls the timing, internal sequencing, mechanism control, engineering and status data acquisition, and data packetization.

The NAC is an  $f/10.5$  reflecting telescope with an image scale of  $\sim 6\mu$  rad/pixel, a  $0.35^\circ \times 0.35^\circ$  FOV, and a spectral range from 200 to 1100 nm. Its filter wheel



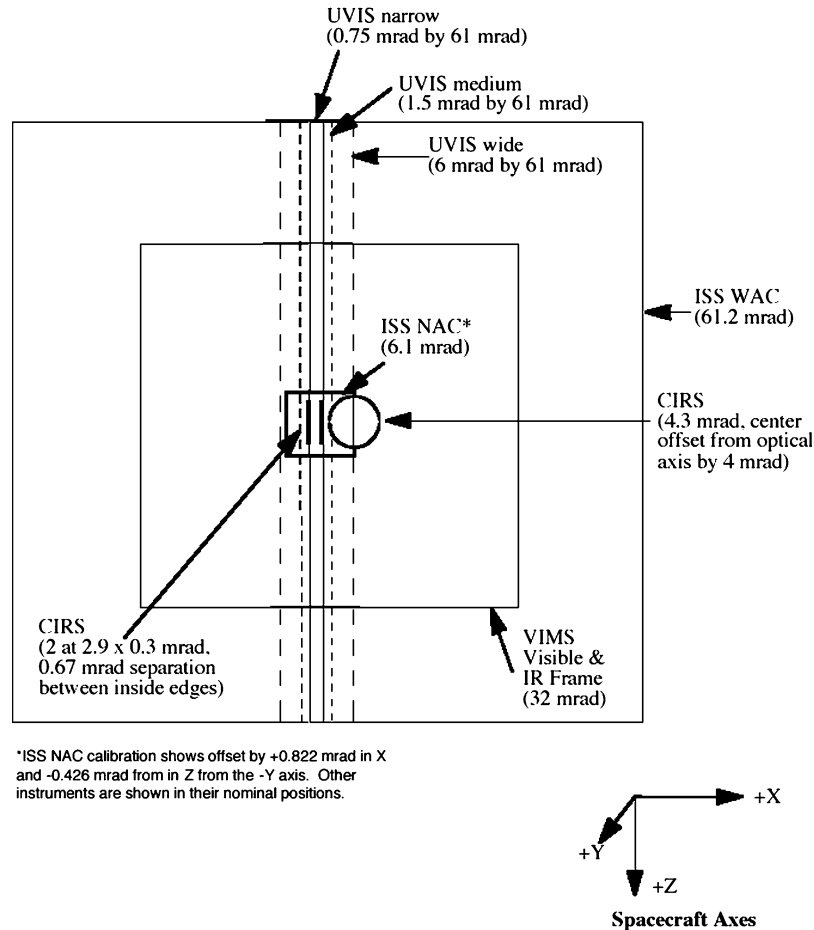
**PROJECTION ON SKY (ALONG Y-AXIS)**

Figure 15. A diagram illustrating the fields of view of the optical remote sensing instruments (Ultra Violet Imaging Spectrometer (UVIS), Composite Infrared Spectrometer (CIRS), and Visual and Infrared Mapping Spectrometer (VIMS), Imaging Science Subsystem (ISS) narrow (NAC) and wide-angle (WAC) cameras.

subassembly carries 24 spectral filters: 12 filters on each of two wheels. The optical train of the WAC, a Voyager flight spare, is an  $f/3.5$  refractor with a  $\sim 60 \mu$  rad/pixel image scale and a  $3.5^\circ \times 3.5^\circ$  FOV. The refractor design limits the lower end of the spectral range on the WAC which is 380–1100 nm. The WAC filter subassembly carries nine filters in each of two filter wheels, for a total of 18 filters. In both cameras, images are acquired through two filters, one on each wheel, allowing in-line combinations of filters for greater flexibility: i.e., polarizers in line with other spectral filters, new bandpasses created by the overlap of two spectral filters, etc.

Narrow Angle Camera

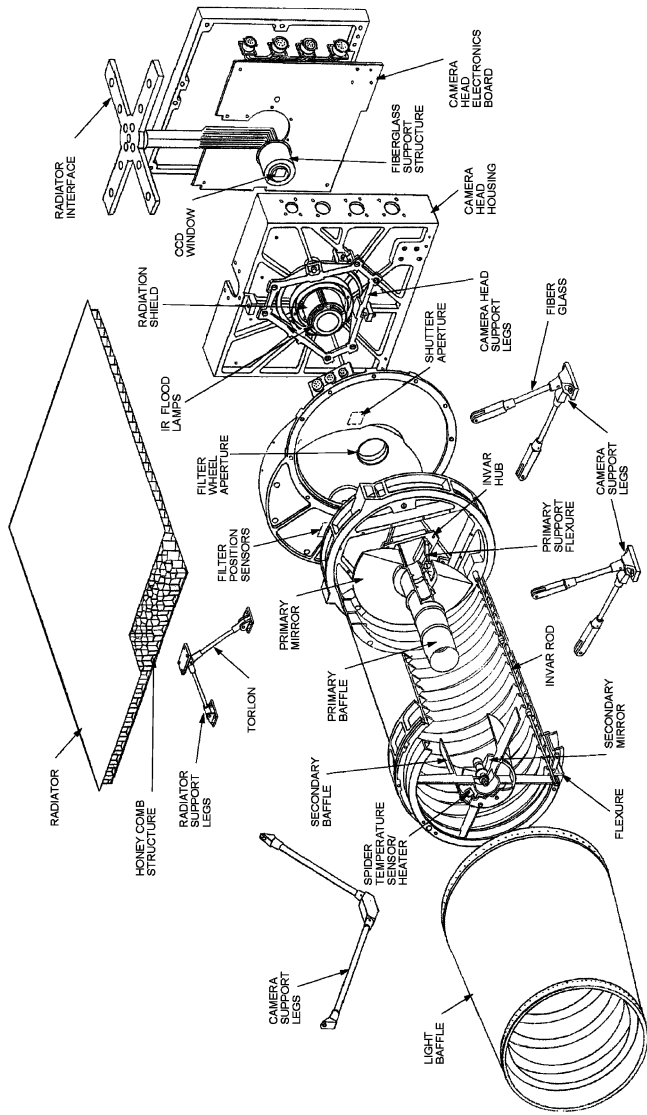


Figure 16. (A) A diagram showing the various components in the Cassini Narrow-Angle Camera Head Assembly. (B) Similar diagram for the Cassini Wide-angle Camera Head Assembly.

(Continued on next page)

Wide Angle Camera

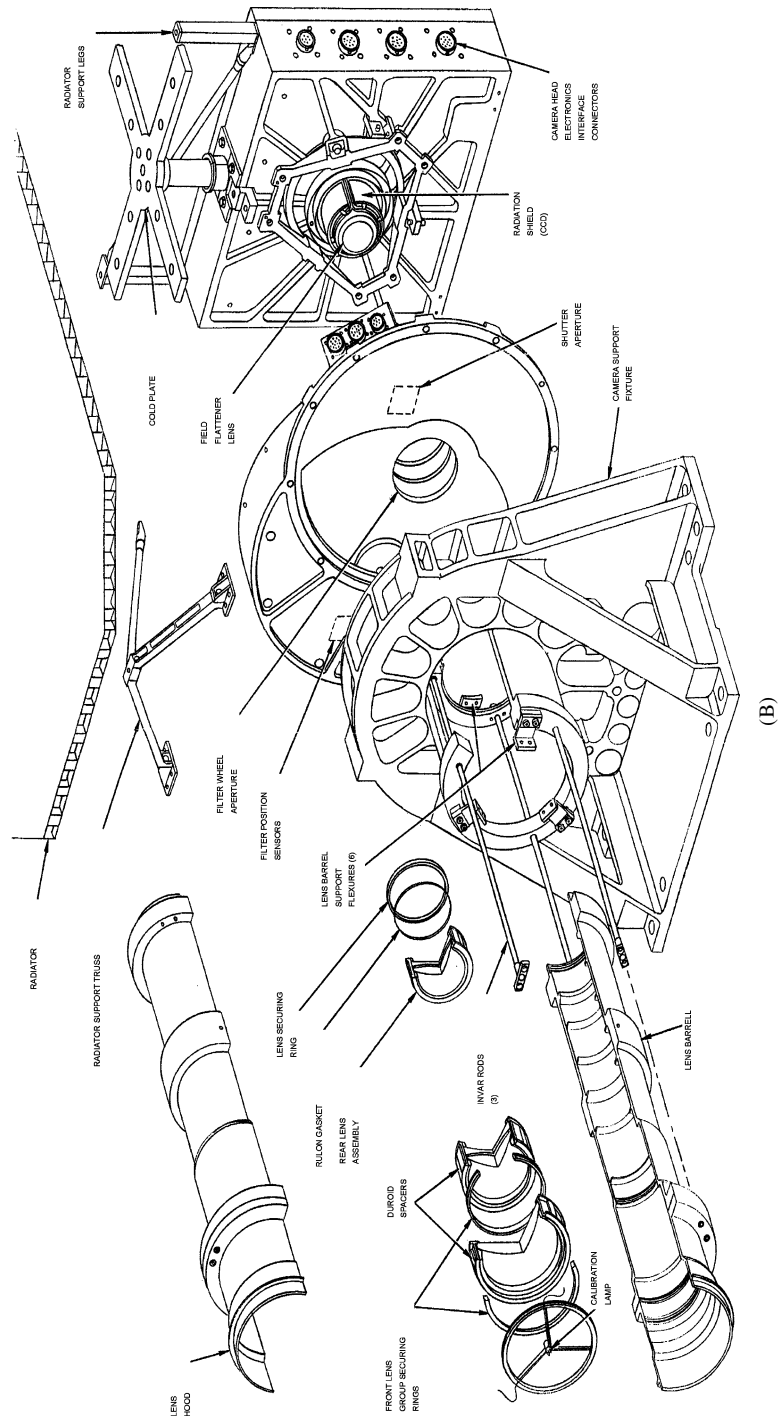


Figure 16. (Continued).

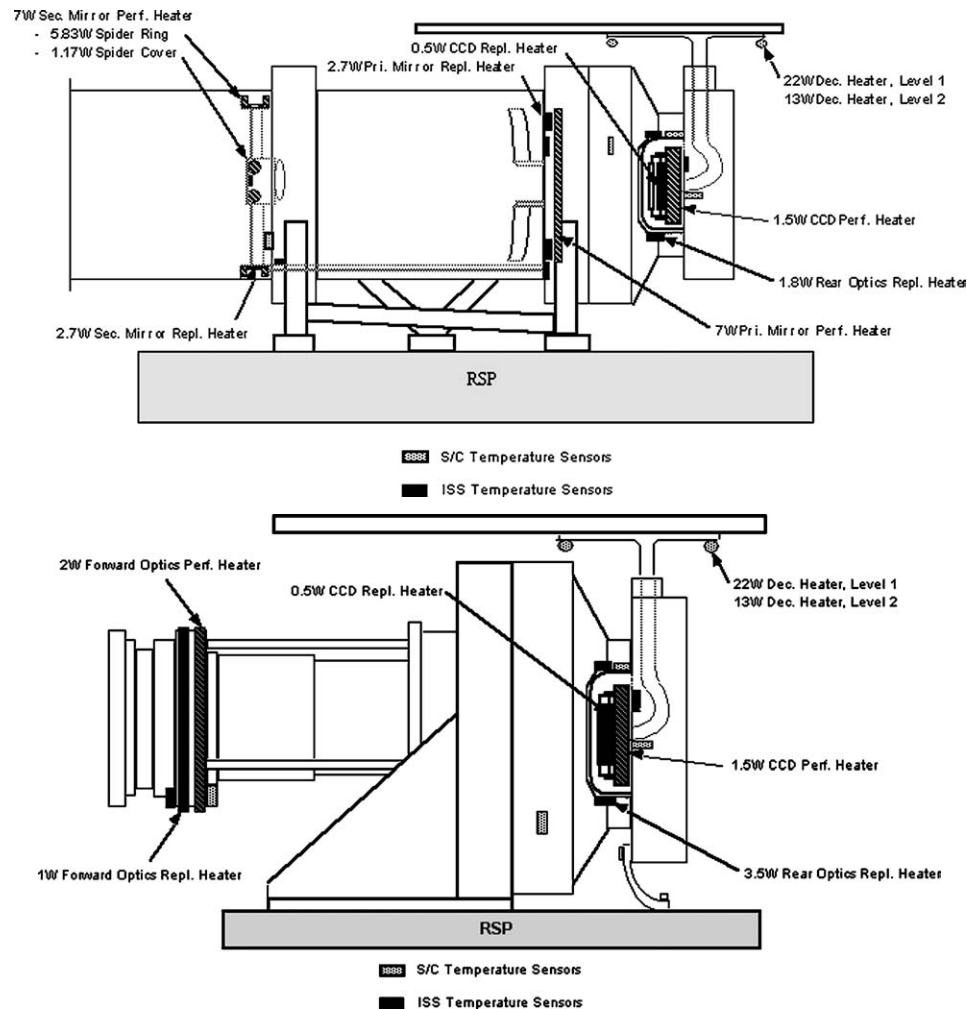


Figure 17. A diagram illustrating the placement of the ISS-controlled replacement and performance ('active') heaters and spacecraft-controlled heaters which thermally stabilize the ISS and keep it within flight-allowable operating limits.

The NAC is thermally isolated from the RSP in order to minimize the effects of RSP thermal transients on the NAC image quality. Unlike the NAC, the WAC has less stringent image quality requirements and its bulk temperature control is provided by the pallet. Figure 17 illustrates the placement of heaters within the ISS.

The temperature of the CCD is controlled by a passive radiator, directly connected to the focal plane, along with an active 'performance' heater on the CCD to adjust the temperature. The temperature of the optical elements is con-

trolled by active ‘performance’ heaters positioned along the optical path. The radiator subassembly also includes two sets of spacecraft-controlled decontamination heaters, which are used to minimize deposition of volatile contaminants on either the detector or radiator and to minimize radiation damage to the CCD. All heaters are commandable (On or Off) during flight.

The ISS has three operational power states: On, Sleep and Off. In the On state, the cameras are Active or Idle. In this state, both the spacecraft replacement heaters and ISS decontamination heaters are Off. The camera software has active control over the performance heaters to set appropriate operating temperatures for the optics and CCD detector. The Active sub-state is entered to collect science data as well as for calibration and maintenance activities. Command execution in the Active state includes science data readout, filter wheel movement, shutter movement, activation of light flood and calibration lamps, and other high power-consuming activities. Idle is a background state in which no commands are executing. When the camera is in Idle state, uploads can be processed, real-time and ‘trigger’ commands can be accepted from the CDS (Section 3.7), and macros can be stored. The execution of any command sends the camera into the Active state. The camera always returns to Idle state after completing a command sequence. Peak power consumption during active imaging is 26.2 W in the NAC and 19.4 W in the WAC (Table VI).

The ISS Sleep state is a non-data-taking low power state that is used when no activity is planned for an extended period. During this state, the sensor head and main ISS electronics are drawing power, and the optics and CCD heaters are On to maintain operating temperature limits. Spacecraft controlled replacement heaters are Off. The decontamination heaters may be used, if necessary. In Sleep, the NAC consumes 22.3 W, and the WAC consumes 16.4 W.

In Off, no power is drawn by the ISS in either the NAC or WAC. The spacecraft controlled replacement heaters and ISS decontamination heaters may be turned

TABLE VI  
Power states of the ISS.

Camera state	Estimated power for NAC (W)	Estimated power for WAC (W)
Off (includes replacement heat)	8.4	4.5
On/Sleep	22.3	16.4
On/Idle	22.3	16.4
On/Active	26.2	19.4
Off/Decon Level 1 (includes replacement heat)	25.7	21.4
Off/Decon Level 2 (includes replacement heat)	35.0	30.7

Currently, Decon 1 draws 20 W, and Decon 2 draws 10 W for both NAC and WAC. The average operating power is 45.6 W during Cruise when NAC and WAC are turned on.

On when necessary. The replacement heaters keep the ISS within allowable flight non-operating temperature limits and the decontamination heaters can be used to provide for CCD protection from the radiation environment and from the condensation of volatiles. In this state, the NAC consumes 8.4 W and the WAC, 4.5 W.

### 3.3. OPTICS

#### 3.3.1. *Design*

The essential difference between the narrow and wide angle camera lies in the design of the optical train. The NAC optics were specially designed to improve on the quality and resolution of images of the bodies in the Saturn system returned by Voyager. It is based on a Ritchey-Chretien reflector design. The focal plane fields of view for both cameras are limited by the size of the CCD. The NAC point spread function (PSF) was designed to be approximately the same physical size as a pixel in the near-IR. Because of the Voyager optics, the same is not true for the WAC, whose PSF is somewhat larger than the pixel size. The full width at half maximum (FWHM) of the PSFs of the NAC and WAC through the clear filters are 1.3 and 1.8 pixels, respectively. The in-flight measured characteristics of the optics of both the NAC and WAC as well as other characteristics are given in Table VII.

All the reflective optical elements within the NAC (the primary and secondary mirrors) are manufactured of fused silica; all refractive NAC elements (such as the field correctors and the window on the sealed CCD package) are made of either fused silica or single-crystal vacuum-UV-grade calcium fluoride. The optical elements in the WAC are composed of radiation-hardened optical glass (BK7 or lithium fluoride) or fused silica. Antireflection coatings consisting of single layer  $\text{MgF}_2$  were deposited on all optical elements (except the NAC mirrors) in both cameras, such as the field correctors in the NAC and the primary optics in the WAC; a multi-layer  $\text{MgF}_2$  coating was applied to the primary and secondary aluminum-coated mirrors in the NAC to enhance reflectivity. A fused silica quartz plug is placed immediately in front of each CCD package to protect the detector against radiation damage and to minimize radiation-induced noise in the images. The spectral transmissions of the NAC and WAC optics are shown in Figure 18.

#### 3.3.2. *Geometric Fidelity*

The use of a CCD ensures that the image geometry is not affected by the brightness, or gradients in brightness, across the scene as it is in a vidicon detector, like Voyager's, with a particle beam readout. Any departure from geometric fidelity in the Cassini cameras is expected to come from the optical elements and/or thermal effects thereon. The long focal length of the NAC makes optical image quality especially vulnerable to temperature changes and gradients along the barrel of the camera. Both cameras were designed to remain in focus without an active focus

TABLE VII  
Cassini ISS characteristics.

General		
CPU	IBM MIL-STD-1750A 16-bit processor	
CCD	Three-phase, front-side illuminated	
Pixel size	12 $\mu\text{m}$	
Format	1024 $\times$ 1024	
Available exposures	64 commandable settings, 5 msec–1200 s	
Minimum framing time	11 s (4 $\times$ 4 sum, highest CDS pickup rate)	
Signal digitization	12 bits, 4095 DN	
Summation modes	1 $\times$ 1, 2 $\times$ 2, 4 $\times$ 4	
Pixel full well	120,000 e <sup>−</sup> (normal); 1,000,000 e <sup>−</sup> (low gain, 4 $\times$ 4)	
Data conversion (12:8)	‘Square Root Encoding’ (LUT), Least-Significant 8 Bits (L58B)	
Data compression	Lossless; Lossy	
Read noise level	12 e <sup>−</sup> (high gain state)	
	NAC	WAC
Type	Reflector	Refractor
Mass	30.5 kg	26.4 kg
Dimensions	95 cm $\times$ 40 cm $\times$ 33 cm	55 cm $\times$ 35 $\times$ 33 cm
$F/N$	10.5	3.5
Focal length	2002.70 $\pm$ 0.07 mm	200.77 $\pm$ 0.02 mm
Pixel angular size	5.9907 $\mu\text{r}$ /pixel	59.749 $\mu\text{r}$ /pixel
FOV	6.134 mrad	61.18 mrad
FWHM of PSF	1.3 pixels	1.8 pixels
Peak power (active)	26.2 W	19.4 W
Spectral range	200–1050 nm	380–1050 nm
Filter positions	12 $\times$ 2 filter wheels	9 $\times$ 2 filter wheels
Gain state	0: 1: 2: 3	0: 1: 2: 3
Gain values (e-/DN)	233: 99: 30: 13	211: 85: 28: 12
Gain state factors	0.13: 0.31: 1.0: 2.36	0.13: 0.31: 1.0: 2.36
Limiting magnitudes (in $t_{\text{exp}}$ = 1 s, gain state 2, 12-bit data)	$M_v \sim 14$	$M_v \sim 11.6$

mechanism. Instead, heaters have been placed in both cameras at various locations (Figure 17) to (i) maintain the temperatures of the optical elements within 1 °C in the NAC and 5 °C in the WAC of the nominal temperature, and (ii) maintain the temperature difference along the barrel within 2 °C in the NAC and 10 °C in the WAC. Low expansion invar spacers help maintain focus in the NAC.

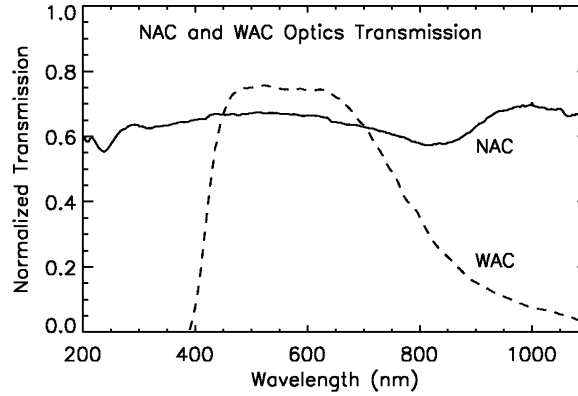


Figure 18. The transmission of the optics of the NAC and the WAC as measured pre-flight. The WAC optics are Voyager-era spare optics which were used in order to reduce costs.

In an ideal camera, the position of an object in the image plane is linearly proportional to its angular distance from the optical axis. Departure from this ideal is expressed as geometric distortion. The larger FOV of the WAC makes it more susceptible to such distortions. Measurements of distortion and its dependence on temperature and spectral bandpass in the NAC and WAC were made on the ground and in flight.

If  $R_{\text{obs}}$  is the observed radial distance of a point from the optic axis, and  $R_{\text{id}}$  the ideal radial distance, the relation can be expressed as  $R_{\text{obs}} = R_{\text{id}} \div (1 + k * R^2)$ . The ground-based measurements suggested distortions up to about  $R_{\text{obs}} - R_{\text{id}} \sim 3.6 \pm 0.2$  pixels in the corners of the CCD in the WAC, independent of spectral bandpass, over the optics temperature range of  $-10^\circ$  to  $+25^\circ\text{C}$ . (Nominal operating optics temperature is  $5^\circ\text{C}$ ). Ground-based measurements were not made on the NAC since analytical calculations indicated distortions less than 1 pixel.

During the cruise from launch to Jupiter, observations were made of the Pleiades and on the open cluster M35 in Gemini in both cameras to determine focal length and distortion, as these observations are capable of far greater accuracy than the ground measurements and also apply to the flight state of the cameras. These images demonstrated a consistent distortion parameter for the WAC of  $k = -6.27 \pm 0.25 \times 10^{-5} \text{ mm}^{-2}$ , and slight changes in focal length as a function of filter combination. The WAC focal length in the clear filter is  $200.77 \pm 0.02 \text{ mm}$ . Focal lengths in other filter combinations range from 200.71 to 201.22 mm, yielding a range in image radius of 1.27 pixels for a nominal 500-pixel radius object. Thus, individual filter combinations need to be fully calibrated to determine specific focal length. The distortion parameter remains essentially constant in the different filters. In-flight distortion measurements for the WAC are consistent with those taken from the ground: 3.36 pixels in the corners.



In the NAC, in-flight measurements from M35 yielded a distortion parameter of  $k = -8.26 \pm 0.23 \times 10^{-6} \text{ mm}^{-2}$ , 0.45 pixels of distortion in the corners, and a clear filter focal length of  $2002.70 \pm 0.07 \text{ mm}$ . NAC focal lengths in different filters range from 2002.13 to 2003.09 mm, yielding a range in radius of a nominal 500-pixel target of 0.24 pixels.

The resulting nominal pixel scale for the NAC is  $5.9907 \text{ } \mu\text{rad/pixel}$ ; for the WAC it is  $59.749 \text{ } \mu\text{rad/pixel}$ .

(It was found that the pixels are systematically rectangular, and not square, at a level  $9\times$  the measurement error in the NAC and the  $25\times$  the measurement error in the WAC, and that they are slightly smaller in the line direction, yielding a different scale in one direction than in the other. However, the difference from square is only 0.01% of the pixel size (or image scale) and is not likely to affect either spatial or photometric measurements in any significant way.)

#### 3.4. SPECTRAL FILTERS: SCIENCE JUSTIFICATION, CHARACTERISTICS AND PLACEMENT

The selection of filters for the Cassini ISS and their distribution between the two cameras were determined by the scientific objectives to be addressed by each camera, the cameras' spectral range and capabilities, and even the orbital tour itself. The fundamental nature of an outer planet orbiter mission like Cassini, which is required to examine many targets at close range at various distances from the planet and is therefore characterized by highly eccentric planet-centered orbits and very fast flybys, mandates coverage of a wide range of viewing and phase angles in very short time intervals. Viewing and phase angle coverage is required for all photometric science, including major Cassini objectives such as characterizing the nature of the icy satellites' terrains, the nature of the ring particles and their size and vertical distributions, and the scattering behavior and vertical distribution of hazes and clouds in the atmospheres of Saturn and Titan. It is during the periods nearest closest approach to Saturn, Titan and the icy satellites that the largest variation in viewing and phase angles occurs. These geometries are not, in general, duplicated at other times during the tour, yet these intervals around closest approach do not allow sufficient time to cover the necessary territory with the NAC. While the NAC will be used for spectrophotometric observations on approach to a target when sequencing time is generally not a contentious issue, this task will be handed over to the WAC during the times nearest closest approach.

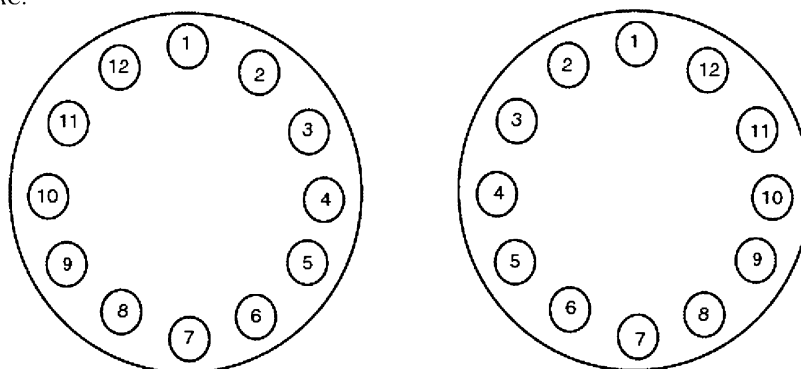
To this end, more than half of the NAC filters are duplicated in the WAC. Seven medium/broad-band filters from the blue to the near-IR for spectrophotometry, two methane and two continuum band filters for atmospheric vertical sounding, two clear filters, and a narrow band Ha filter for lightning observations are all carried on both cameras. For these common filters, the bandpasses are actually shifted a

little (up to 15 nm) because of the differing spectral transmissions of the WAC and NAC optics. These common filters will also enable a cross-check on radiometric calibrations.

The ISS filter assembly design – consisting of two filter wheels and a filter changing mechanism – is inherited from the HST WF/PC camera. Each wheel is designed to move independently, in either the forward or reverse direction, at a rate of two filter positions per second in the WAC and three positions per second in the NAC. A homing sensor on each wheel defines a home wheel position: wheel positioning can be commanded absolutely or relatively.

(The layout of the filters in each filter wheel in each camera is illustrated in Figure 19; filter characteristics are listed in Table VIII; the spectral transmissions are plotted in Figures 20–22.)

A. NAC:



#### NAC Filters

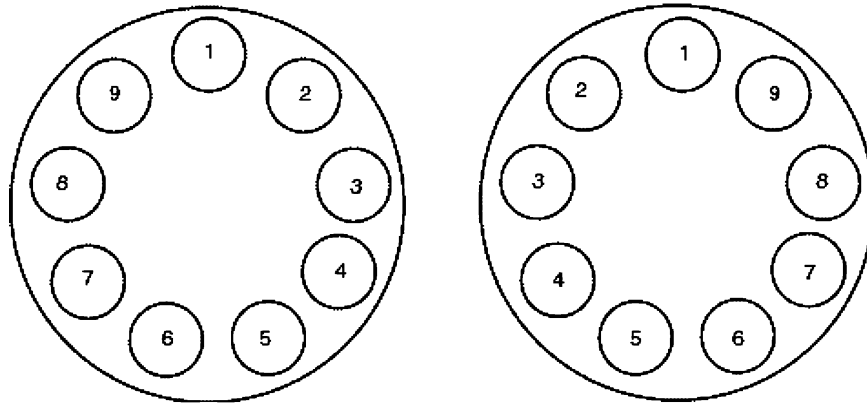
(Wavelengths, in nm, are central wavelengths computed using the full system transmission function.)

Filter Wheel #1	Filter Wheel #2
1) CL1 (611W)	1) CL2 (611W)
2) Red (650W)	2) GRN (568W)
3) BL1 (451W)	3) UV3 (338W)
4) UV2 (298W)	4) BL2 (440M)
5) UV1 (258W)	5) MT2 (727N)
6) IRP0 (746W)	6) CB2 (750N)
7) P120 (617W)	7) MT3 (889N)
8) P60 (617W)	8) CB3 (938N)
9) P0 (617W)	9) MT1 (619N)
10) HAL (656N)	10) CB1 (619N)
11) IR4 (1002LP)	11) IR3 (930W)
12) IR2 (862W)	12) IR1 (752W)

Figure 19. The distribution of the Cassini spectral filters in the two filter wheels in the NAC and WAC. The numerical values quoted for each filter are the central wavelengths computed using the full system transmission function (Table VIII) and are the numerical ‘names’ by which the filters are referenced.

(Continued on next page)

B. WAC:

**WAC Filters**

(Wavelengths, in nm, are central wavelengths computed using the full system transmission function.)

**Filter Wheel #1**

- 1) CL1 (635W)
- 2) IR3 (918W)
- 3) IR4 (1001LP)
- 4) IR5 (1028LP)
- 5) CB3 (939N)
- 6) MT3 (890N)
- 7) CB2 (752N)
- 8) MT2 (728N)
- 9) IR2 (853W)

**Filter Wheel #2**

- 1) CL2 (635W)
- 2) RED (648W)
- 3) GRN (567W)
- 4) BL1 (460W)
- 5) VIO (420SP)
- 6) HAL (656N)
- 7) IRP90 (705W)
- 8) IRP0 (705W)
- 9) IR1 (742W)

*Figure 19. (Continued).*

Specific scientific considerations that dictated filter choices included the following.

1. Achieving the highest possible sensitivities for imaging faint targets as well as allowing short exposure times to minimize smear during close flybys. There are clear filters in each filter wheel, sensitive to the full spectral range of the CCDs. The clear filter is in the “home” slot of each filter wheel, since it was deemed that sticking of a filter wheel, should it occur, was most likely to occur in the home position. Typically, a clear filter in one wheel is combined with a color filter in the other wheel. Because of the use of Voyager refractive optics, the CL1 filter in the WAC is a special thin filter designed to improve focus across the entire spectral range of the WAC when used in combination with the filters on the second WAC filter wheel (Figure 19).
2. Covering the spectral range of the CCD for color imaging of a wide range of targets. These are a set of medium- and broad-band color filters and include the

TABLE VIII  
ISS filter characteristics.

Filter	$\lambda_{\text{cen,NAC}}$	$\lambda_{\text{eff,NAC}}$	$\lambda_{\text{cen,WAC}}$	$\lambda_{\text{eff,WAC}}$	Science justification
UV1	258W	264	–	–	Aerosols
UV2	298W	306	–	–	Aerosols, broad-band color
UV3	338W	343	–	–	Aerosols, broad-band color, polarization
VIO	–	–	420SP	420	Broad-band color
BL2	440M	441	–	–	Medium-band color, polarization
BL1	451W	455	460W	463	Broad-band color
GRN	568W	569	567W	568	Broad-band color
MT1	619N	619	–	–	Methane band, vertical sounding
CB1	619N	619	–	–	Two-lobed continuum for MT1
CB1a	635	635	–	–	
CB1b	603	603	–	–	
RED	650W	649	648W	647	Broad-band color
HAL	656N	656	656N	656	H-alpha/lightning
MT2	727N	727	728N	728	Methane band, vertical sounding
CB2	750N	750	752N	752	Continuum for MT2
IR1	752W	750	742W	740	Broad-band color
IR2	862W	861	853W	852	Broad-band color; ring absorption band
MT3	889N	889	890N	890	Methane band, vertical sounding
CB3	938N	938	939N	939	Continuum for MT3; see thru Titan haze
IR3	930W	928	918W	917	Broad-band color
IR4	1002LP	1001	1001LP	1000	Broad-band color
IR5	–	–	1028LP	1027	Broad-band color
CL1	611	651	635	634	Wide open, combine with wheel 2 filters
CL2	611	651	635	634	Wide open, combine with wheel 1 filters
P0	617	633	–	–	Visible polarization, 0°
P60	617	633	–	–	Visible polarization, 60°
P120	617	633	–	–	Visible polarization, 120°
IRP0	746	738	705	705	IR polarization; see through Titan haze
IRP90	–	–	705	705	IR polarization; see through Titan haze

All wavelengths in nm. Central wavelengths ('cen') are computed using the full system transmission function (i.e., item (12) given in Section 3.13.1). These numbers are taken to be the numerical name assigned to the filter. Effective wavelengths ('eff') are computed using the full system transmission function convolved with a solar spectrum (Figure 23). Bandpass types: SP: short wavelength cutoff; W: wide; N: narrow; LP: long wavelength cutoff.

BL1, GRN, RED, IR1, IR2, IR3, and IR4 filters on both cameras, and the UV1, UV2, and UV3 (NAC only) and VIO and IR5 (WAC only) (Figure 20).

Because of its reflecting optics and its unique ability to see in the UV, only the NAC carries filters for UV observations. The lumogen coating on the CCDs

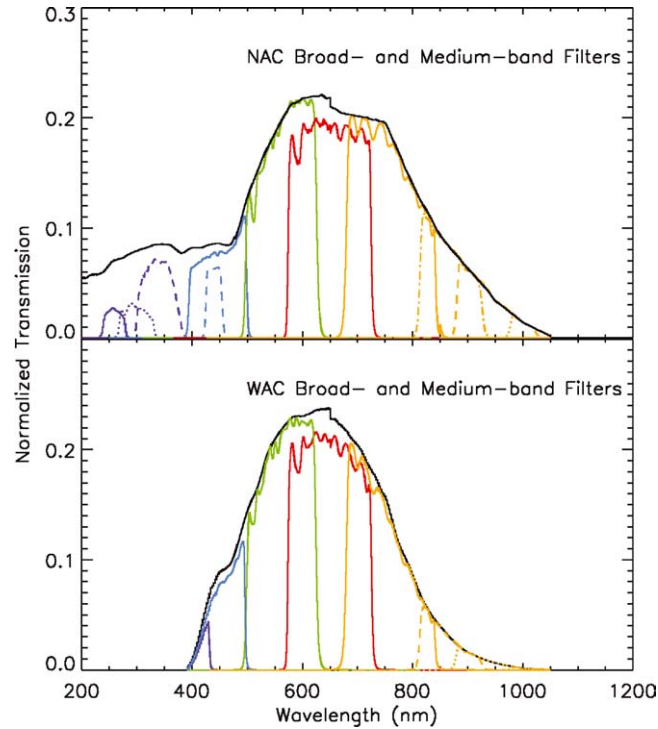


Figure 20. System transmission functions for NAC and WAC broad- and medium-band filters. Filters for the NAC are as follows: UV1, UV2, UV3 (purple: solid, dotted, and dashed); BL1, BL2 (blue: solid and dashed); GRN (green); RED, (red); IR1, IR2, IR3, and IR4 (orange: solid, dot-dash, dashed, and dotted). For the WAC: VIO (purple), BL1 (blue), GRN (green), RED (red), IR1, IR2, IR3, IR4 and IR5 (orange: solid, dashed, dotted, and the latter two not shown). The CL1/CL2 filter combination is given by the solid black line in both plots.

(Section 3.6) provides a unique spectral capability, unavailable on either the Voyager or Galileo imaging systems, which Cassini carries to the outer solar system for the first time. It enables spectral response down to 200 nm. To take advantage of this capability, the range from 230 to 390 nm is spanned by three UV filters: UV1, UV2, and UV3. These provide the best visibility of stratospheric aerosols and potential UV auroral phenomena (as observed at Jupiter; Porco *et al.* 2003), and may aid discrimination of satellite and ring surface materials of special interest such as carbonaceous materials (Wagner *et al.*, 1987). However, the solar spectral irradiance at Saturn is extremely low in the UV, especially at 255 nm (UV1) (Figure 23) so long exposure times will be needed and  $2 \times 2$  or  $4 \times 4$  summation modes may be used to increase the signal to noise ratio at these wavelengths. The demonstrated stability of the spacecraft on reaction wheels enables investigations of Saturn system targets in the UV not previously possible with Voyager.

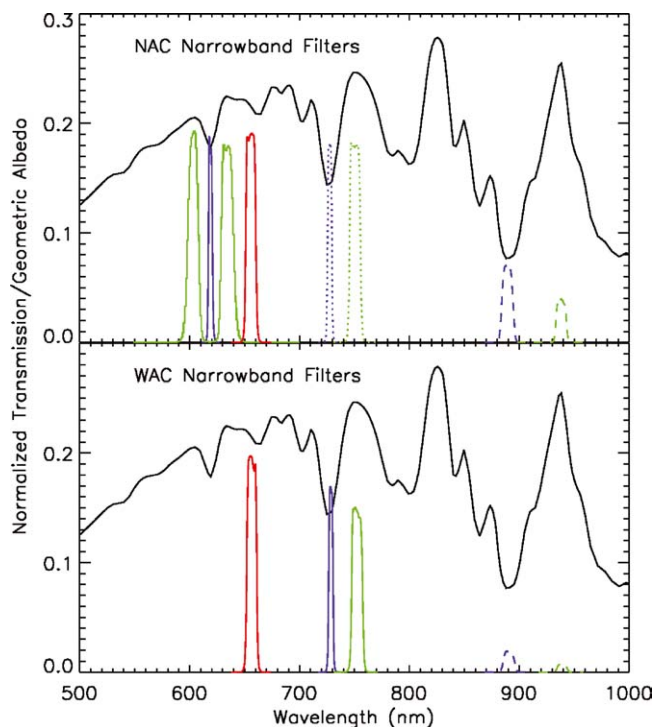


Figure 21. System transmission functions for the NAC and WAC narrow-band filters. NAC filters are as follows: MT1, MT2, MT3 (purple: solid, dotted, and dashed); CB1, CB2, CB3 (green: solid, dotted, and dashed); and HAL (red). WAC filters are HAL (red), MT2, MT3 (purple: solid and dashed); CB2 and CB3 (green: solid and dashed). The geometric albedo of Titan is also given (solid black) to illustrate the placement of the methane band and continuum filters relative to the methane features in the spectrum of Titan.

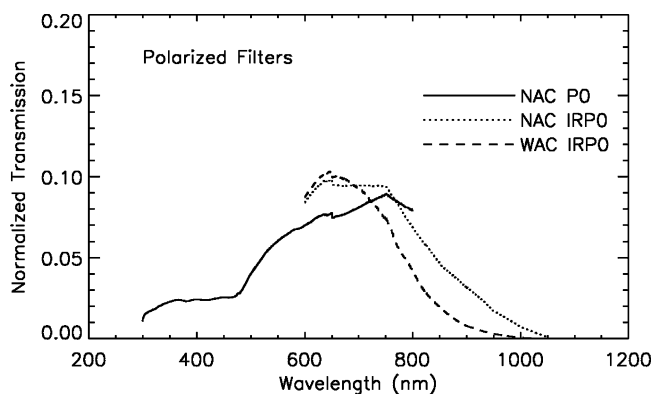


Figure 22. System transmission functions for the NAC visible and infrared, and the WAC infrared, polarizers.

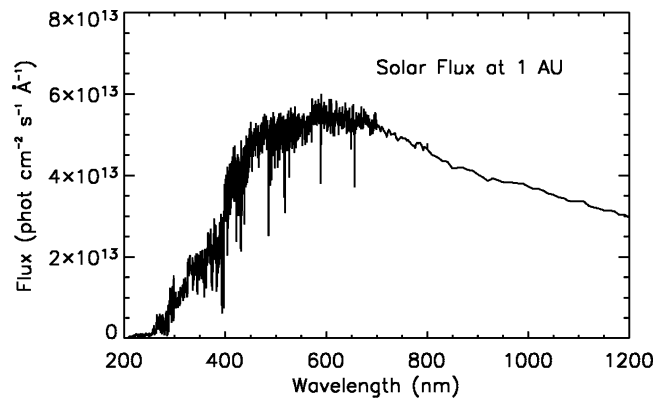


Figure 23. The solar spectrum that has been used in performing calibrations of the ISS (Tobiska *et al.*, 2000).

3. The need for narrow band filters for atmospheric studies. Methane absorption bands and continuum wavelengths are available for studying the vertical structure; these include MT1 and CB1 (NAC only), MT2 and CB2, and MT3 and CB3. (CB1 is a two-lobed continuum filter, with lobes on each side of the methane absorption band.) The HAL filter is included on both cameras for Ha emissions from lightning on Saturn (Figure 21).

Though both cameras are capable of seeing into the near-IR at  $\sim 1.0 \mu$ , the WAC is nine times faster for a given exposure than the NAC. It is consequently better equipped to sense this spectral region for either broad-band color imaging or atmospheric sounding where the CCD quantum efficiency and solar flux are declining and a large camera throughput is desired. (This benefit is reduced somewhat by the Voyager optical coatings.)

4. Polarization filters, for the study of the scattering properties of atmospheres, rings, and satellite surfaces. Three polarizers with principal transmission axes separated by  $60^\circ$  are sufficient to measure intensity and the degree and direction of linear polarization regardless of camera orientation, and so provide the greatest viewing versatility. Three such polarizers, useful only in the visible spectrum are carried in the NAC: P0, P60 and P120 (Figure 22). Given the reduced number of filter slots in the WAC, it does not include the visible polarizers. However, the WAC carries two orthogonal infrared polarizers, IRP0 and IRP90, which can provide intensity and the Stokes parameter,  $Q$ , referenced to the principal axes of the polarizers. If the polarizers are oriented parallel or perpendicular to the scattering plane, the information provided by  $Q$  is in most cases as informative as that provided by three polarizers because the polarized electric vector is usually aligned parallel or perpendicular to the scattering plane. Estimates of  $Q$  referenced to the scattering plane can be made for other orientations but with diminishing precision as the angle between the scattering plane and the polarizer axis approaches  $45^\circ$  at which point the measurement of  $Q$  is not useful.

TABLE IX  
Two-filter bandpasses.

Camera	Filters	$\lambda_{\text{cen}}$ (nm)	$\lambda_{\text{eff}}$ (nm)
NAC	UV2-UV3	316	318
NAC	RED-GRN	601	601
NAC	RED-IR1	702	702
BOTH	IR2-IR1	827	827 (NAC)
		826	826 (WAC)
NAC	IR2-IR3	902	902
NAC	IR4-IR3	996	996

The NAC has only one infrared polarizer, IRP0. By measuring the intensity in this polarizer and also in the clear filter, we can measure  $Q$  although with less accuracy than is achieved with two orthogonal polarizers.

The polarizers are, of course, to be used in combination with other spectral filters and so filter placement was important. In the NAC, the three visible polarizers and the one IR polarizer can all be used in conjunction with a suite of spectral filters on the opposite wheel covering the UV to the near-IR. In the WAC, two broad-band filters IR2 (853 nm) and IR4 (1002LP nm), and the four narrow-band filters – the two strong methane filters MT2 (728 nm) and MT3 (890 nm) and the accompanying continuum band filters CB2 (752 nm) and CB3 (939 nm) – are all placed in the same wheel opposite the wheel containing the two IR polarizers. The polarizers on both the NAC and WAC will be used to reduce contributions from scattering by atmospheric haze. In particular, the IR polarizers on both cameras will aid in imaging the surface and lower atmosphere of Titan, especially when used in combination with near-IR filters such as CB3. The ability to reduce scattering from haze is most effective near 90° solar phase angle.

5. The requirement to image in particular absorption bands. Although the common filter choices involve use of either a clear or polarizing filter in one filter wheel and a spectral filter in the other, we have designed spectral overlap into the broad-band color filters to create a series of two-filter bandpasses to be used primarily in the NAC (Figure 24; Table IX). The two-filter bandpasses were, when possible, designed to cover potential absorption bands of candidate materials, such as weak bands of ammonia (NH<sub>3</sub>), methane (CH<sub>4</sub>), and water (H<sub>2</sub>O) ices. There is also a weak band at 600 nm, of unknown origin, in the spectra of several satellites, which can be mapped out with the RED/GRN combination. The IR1/IR2 two-filter bandpass (available on both NAC and WAC) may permit detection of nitrogen emission lines on Titan. A reasonable job of identifying and mapping the 800–1100 nm region, where silicates and oxides containing Fe<sup>2+</sup> and Fe<sup>3+</sup> produce absorption bands, can be done via use of the following



filter combinations: CL1/CB2 (750 nm), IR2/IR1 (827 nm), IR2/IR3 (902 nm), CL1/CB3 (938 nm), IR4/IR3 (996 nm), IR4/CL2 (1002LP nm) or IR5/CL2 (1028LP nm).

On the WAC, with the spare Voyager refractive optics, we encountered difficulty in achieving a sharp focus in filter combinations that did not utilize the thin CL1 filter. As a result, the only useful two-filter bandpass in the WAC is IR1–IR2.

#### 3.4.1. Filter Fabrication

With the exception of the clear filters and the polarizers, the filters are all interference filters manufactured using an ion-aided deposition (IAD) process which makes the filters temperature and moisture tolerant and resistant to de-lamination. Conventional interference filters have passbands that shift with temperature. The shift can be significant for narrow-band filters such as those targeted to methane absorption bands or the H $\alpha$  line. Temperature shifts for IAD filters are typically an order of magnitude or more smaller than for conventional filters and are insignificant

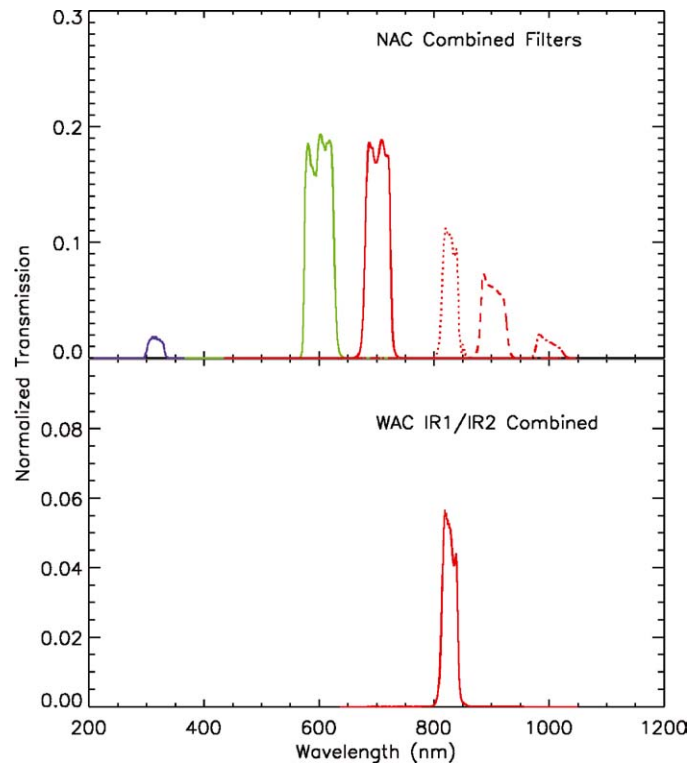


Figure 24. System transmission functions for selected filter combinations in the NAC and WAC. NAC filter combinations are as follows: UV2/UV3 (purple), RED/GRN (green), RED/IR1 (red: solid), IR1/IR2 (red: dotted), IR2/IR3 (red: dashed), and IR3/IR4 (red: dot-dashed).

over the temperature range (room temperature to 0° C) relevant to calibration and operation of the Cassini cameras.

The NAC visible polarizers consist of a thin film (less than 1  $\mu\text{m}$  thick) of a polarizing polymer deposited between two fused silica plates. Ideal polarizers block only photons whose electric vector is orthogonal to the principal axis of the polarizer. The visible polarizers fall short of this ideal behavior in two ways. They transmit too little of either polarization in the ultraviolet, and too much of the light polarized orthogonal to the principal axis in the near-infrared. Their performance is best between 450 and 650 nm, where the principal axis transmission is between 0.45 and 0.65 and the orthogonal transmission is less than 1%. The useable range of the visible polarizers extends from the UV3 filter near 350 nm to the CB2 filter at 750 nm.

The infrared polarizers have a 1 mm thick layer of Polarcor (trademark Corning) cemented between two slabs of BK7-G18 glass. Polarcor is a borosilicate glass impregnated with fine metallic wires. The infrared polarizers have much better performance over their range (700–1100 nm) where the principal transmission is greater than 0.9 and the orthogonal transmission is 0.001 or less.

### 3.5. SHUTTER

Between the filter wheel assembly and the CCD detector is the shutter assembly, a two-blade, focal plane electromechanical system derived from the one used on Voyager, Galileo and WFPC. To reduce scattered light, the shutter assembly was put in the optical train ‘backwards’, with the unreflective side towards the focal plane, unlike its positioning in the Voyager and Galileo cameras. Each blade moves independently, actuated by its own permanent magnet rotary solenoid, in the sample direction: i.e., keeping the blade edge parallel to the columns of the CCD (see Section 3.6.1). The shutter assembly is operated in three phases: open (one blade sweeps across the CCD), close (the other blade sweeps across the CCD to join the first), and reset (both blades simultaneously sweep across the CCD in the reverse direction to the start position).

There are 64 commandable exposure settings which can be updated during flight if so desired. These correspond to 63 different exposure times, ranging from 5 ms to 20 min, and one ‘No Operation’ setting. (The shortest non-zero exposure is 5 ms.) In the ISS flight software, the time tag on the image is the time of the close of the shutter. Because of mechanical imperfections in the shutter mechanism, there is a difference between the commanded exposure time and the actual exposure time, and a gradient in exposure time across the CCD columns. At an operating temperature of 0°C, the mean differences in the NAC for commanded exposure times of 5, 25 and 100 ms were measured to be 0.98, 1.52 and 0.97 ms, respectively. In the WAC, the differences are 0.15, 0.39 and 0.07 ms. In all cases, the actual exposure times

are less than the commanded times. There is also a small temperature dependence to these shutter offsets.

The 1024th column is illuminated first in both cameras. In the NAC, this column is illuminated for  $\sim 0.3$  ms longer than the first column; in the WAC, the 1024th column is illuminated  $\sim 0.1$  ms longer than the first. These values are independent of exposure time and reasonably independent of temperature. The expected precision or repeatability of an exposure (equal to the standard deviation of actual exposure durations measured at any one location on the CCD in ground tests) is  $\leq 0.03$  ms for the NAC and  $\leq 0.04$  ms for the WAC. Corrections for the mean and the spatially dependent shutter offsets are incorporated into Cassini ISS calibration software (CISSCAL). The shutters were tested for light leak. None was detectable in the NAC at a fluence level of 12,000 times full well exposure on the closed shutter. A small signal was detected in the WAC. It produced 1 DN (12 electrons) or less at a level of 10,000 times full well incident on the closed shutter.

### 3.6. DETECTOR

The CCD detector used in the Cassini ISS was manufactured by Loral, packaged by JPL, and employs three phase, front-side-illuminated architecture. The imaging area – the region on which light is focused – is a square array of  $1024 \times 1024$  pixels, each  $12 \mu$  on a side. The CCDs on both cameras were packaged, hermetically sealed and fronted by a fused silica window.

The CCD's response to light is determined by the spectral dependence of each pixel's quantum efficiency: i.e., the number of electrons released in the silicon layer for each photon incident on it. In front-side-illuminated CCDs (like that in the Cassini ISS), the overlying polysilicon gate structures do not transmit UV light. To achieve the required UV response, a UV-sensitive organic fluorescent material called lumogen was vacuum-deposited onto the CCD at  $+80^\circ$  C after it was bonded. In this  $0.6 \mu$  layer, UV photons are converted into visible photons in the range 540–580 nm that readily penetrate the silicon below. Under vacuum conditions, the lumogen layer would tend to evaporate when CCD temperatures reached  $+60^\circ$  C. For this reason, the CCD sealed packages were back-filled with inert argon gas to a half atmosphere pressure. All flight candidate CCDs were coated with lumogen before the two flight CCDs were chosen and assigned to each camera. Hence, despite the fact that the WAC optics do not transmit in the UV, the WAC CCD is also coated with lumogen.

The efficiency of a CCD in the near-IR depends on its thickness, or more precisely on the thickness of the very thin, high-purity silicon layer which is epitaxially grown over a thicker ( $\sim 500 \mu$ ) substrate. It is the photons absorbed in the epitaxial layer that are converted into the signal electrons that are subsequently collected and sampled. Nearly all of the near-IR photons actually penetrate beyond the 'epi' layer and create charge in the substrate. However, the purity contrast between the

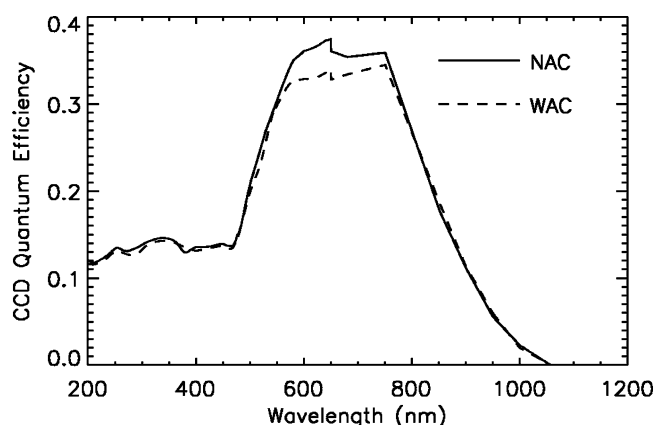


Figure 25. The quantum efficiency of the CCDs in the NAC and WAC, as measured during the ground calibration. Despite the fact that the WAC optics are opaque in the ultraviolet, the WAC CCD was also coated with lumogen and consequently has significant response in the UV.

substrate and the epi layer prevents substrate-generated charge from entering the epi layer and being collected. Thus, the 1100 nm quantum efficiency is essentially the fraction of incident flux which is absorbed in the thin layer of pure silicon: the thicker the 'epi' layer, the higher the infrared sensitivity.

However, the thicker this layer, the lower the spatial resolution. A compromise was made in the manufacture of the CCD to yield some response near 1100 nm while maintaining high spatial resolution. The 'epi' layer is 10–12  $\mu\text{m}$  thick on Cassini and results in a quantum efficiency (QE) of  $\sim 1\%$  at 1000 nm.

Figure 25 shows the quantum efficiency versus wavelength of the CCDs carried in Cassini ISS.

A compromise involving the near-IR response was also made in choosing the CCD operating temperature. At Saturn, this temperature is  $-90^\circ \pm 0.2^\circ \text{C}$  and is a compromise between yielding an acceptably low dark current ( $\leq 0.3 \text{ e}^-/\text{sec/pixel}$ ) and maintaining a reasonable near-IR response (which is diminished at low temperatures). CCD thermal control is achieved by means of balance between passive radiation to space, which alone would maintain the CCD below its operating temperature at Saturn, and active heater control. The radiator of each camera also supports a decontamination heater (35 W in all) that can heat the CCD to  $+35^\circ \text{C}$  to reduce the deposition of volatile contaminants on either the detector or the radiator. (Because damage to the CCD due to cosmic rays can be annealed at elevated temperatures, the CCD operating temperature during cruise, when data were not being collected, was maintained at  $0^\circ \text{C}$  to minimize such damage.)

The CCD has the capability of being commanded to operate in full mode (i.e.,  $1 \times 1$ ) or either  $2 \times 2$  or  $4 \times 4$  on-chip pixel summation modes. The latter two modes are used for either enhancing signal to noise and/or decreasing the data volume and/or readout time at the expense of spatial resolution. The full well of the

TABLE X

Gain values (electrons/DN) and Ratios (Relative to Gain 2) for the different gain States in the ISS.

Gain state		NAC (e-/DN)	Ratio	WAC (e-/DN)	Ratio
0	Designed for $4 \times 4$	$233 \pm 29$	0.134	$211 \pm 16$	0.134
1	Designed for $2 \times 2$	$99 \pm 13$	0.314	$85 \pm 7$	0.311
2	Used in $1 \times 1$	$30 \pm 3$	1.000	$28 \pm 1$	1.000
3	Used in $1 \times 1^*$	$13 \pm 2$	2.36	$12 \pm 1$	2.36

\*The highest gain state was chosen to match the read noise.

CCD is roughly  $120,000 \text{ e}^-/\text{pixel}$ . Four gain states are available: for imaging faint objects (high gain, Gain 3) and bright objects (normal gain, Gain 2), and to match the output of the  $2 \times 2$  (Gain 1) and  $4 \times 4$  (Gain 0) full wells. The summation well can hold only  $1.6 \times 10^6$  electrons; this corresponds to full well with  $4 \times 4$  summing. However, the relation between number of electrons in the signal and the digital data numbers (DN) into which the signal is encoded starts to become nonlinear above  $10^6$  electrons because at this signal level, the on-chip amplifier becomes nonlinear. For this reason, in the lowest gain state (Gain 0), the full-scale signal is set to correspond to  $\sim 10^6$  electrons at 4095 DN. The array of summation and gain state options as well as the uncertainties in each gain are given in Table X.

The capability also exists within the ISS to reduce the effect of blooming, the phenomenon whereby a highly overexposed pixel can spill electrons along an entire column of pixels, and sometimes along a row, when the full well of the CCD is exceeded. The default camera setup has anti-blooming On, with the option to turn it Off. Anti-blooming mode is achieved by applying an AC voltage to the chip, forcing excess electrons into the silicon substrate. An undesirable side effect of this action is to pump electrons into traps in the silicon at the expense of electrons in adjacent pixels. For long exposures (longer than about 20 s) this produces bright/dark pixel pairs. These were initially present in nearly all the NAC flat-field files obtained during calibration in the thermal vacuum chamber. Corrected flat-field files with these pixel pairs removed have been created.

### 3.6.1. Coordinate System and Readout Scheme

There are two ISS coordinate systems in use: the one officially used on the Cassini Project to describe camera orientation ( $X \text{ cm}$ ,  $Y \text{ cm}$ ), which is directly related to the readout directions of the CCD samples and lines, and another used in general by imaging scientists ( $X \text{ im}$ ,  $Y \text{ im}$ ) to describe images which are rotated from the target being imaged. There is also the spacecraft coordinate system ( $X \text{ s/c}$ ,  $Y \text{ s/c}$ ,  $Z \text{ s/c}$ ). Figure 26 indicates the relationships among all these systems.

The cameras and other instruments on the RSP are pointing in the  $-Y \text{ s/c}$  direction. The positive  $Z \text{ s/c}$  axis points towards the spacecraft's main engines; the

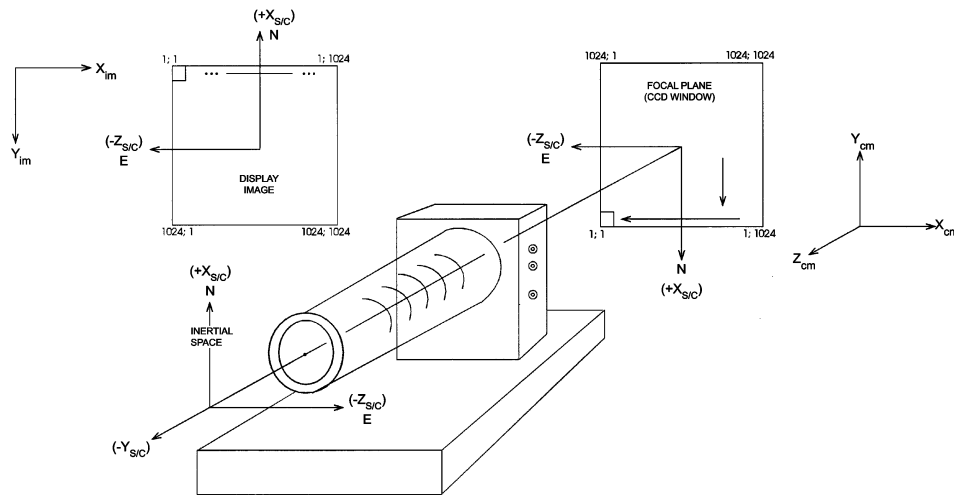


Figure 26. An illustration of the relationships among the three main coordinate systems involved in the analysis and interpretation of image geometry: the spacecraft coordinate system ( $X$  s/c,  $Y$  s/c,  $Z$  s/c), the JPL/ISS coordinate system ( $X$  cm,  $Y$  cm,  $Z$  cm) (which is determined by the readout of the CCD, indicated by arrows drawn in the CCD Window (ie, the physical sample and line directions,  $(s, l) = (X$  cm,  $Y$  cm)), and the coordinate system generally used in the display and examination of an image, ( $X$  im,  $Y$  im). In this diagram, the spacecraft  $+X$  s/c is aligned with inertial north; celestial (or astronomical) east is indicated. The optics rotates the image of the target, as well as the image of the spacecraft's orientation in inertial space,  $180^\circ$ , from their true inertial space orientations.

$-Z$  s/c points towards the High Gain Antenna; the  $+X$  s/c axis is up. In Figure 26, the CCD readout proceeds as follows.

The bottom line of the CCD is shifted down (i.e., toward the remote sensing palette, toward  $-X$  s/c) into a vacant one-line serial register. This line is then shifted to the left (in the  $+Z$  s/c direction), pixel by pixel, to the signal chain until the entire line is readout. The pixels are numbered by the order in which they proceed to the signal chain. Thus, the first has sample =  $X$  cm = 1, the last has sample =  $X$  cm = 1024. That is, the readout proceeds in the  $-X$  cm direction. After this line is completely readout, the next line is shifted down into the serial register and readout, and so on until all 1024 lines have been shifted into the register and then along to the signal chain.

This results in the following relationship between the spacecraft and the physical ISS/CCD coordinate systems: (sample, line) =  $(+X$  cm,  $+Y$  cm) =  $(-Z$  s/c,  $+X$  s/c).

The images of celestial bodies taken by the ISS are inverted up/down and flipped left/right (i.e., rotated  $180^\circ$ ) by the optics in both cameras. The relationships between targets and inertial space, as well as the relationship between the target and the orientation of the Cassini spacecraft, are all maintained through this rotation. Thus, the *image* of a celestial target, as well as the *image* of the spacecraft coordinate system in the focal plane, are rotated from their physical orientations. A celestial

target with its North pole aligned with the spacecraft  $+X$  s/c axis would appear inverted and flipped on the CCD: that is, *in the focal plane and display image plane* (Figure 26), the North pole of the target and the  $+X$  s/c axis would point in the direction of decreasing line ( $-Y$  cm and  $-Y$  im); the target's western limb (or, astronomical East) and the  $-Z$  s/c axis would point towards decreasing sample ( $-X$  cm and  $-X$  im).

The Cassini C-Kernel contains information that is used by the Navigational Ancillary Information Facility (NAIF) SPICE toolkit to derive a matrix which transforms a vector in inertial coordinates into the spacecraft coordinate system ( $X$  s/c,  $Y$  s/c,  $Z$  s/c). The Cassini Frames kernel describes a transformation matrix that transforms a vector from the camera coordinate system ( $X$  cm,  $Y$  cm,  $Z$  cm) into the spacecraft frame. The proper combination of the two describes the orientation of the physical camera/CCD system relative to inertial space. To compute the correct orientation of inertial space, and the targets in it, in the image plane, which is where anyone handling an image will work, one must apply an additional  $180^\circ$  rotation about the center of the image.

The detector system includes an unilluminated region eight samples wide – the ‘extended pixel region’ – extending into the negative sample direction in the serial register. These pixels get readout first. Moreover, once an entire row of 1024 pixels is readup into the serial register and out to the signal chain, the readout continues for eight more clock cycles, or over-clocked ‘virtual’ pixels, to provide a measure of the offset bias, the DN value that corresponds to zero signal level. The extended pixel region and the over-clocked pixels in principle provide two independent measures of offset bias and a sample of the horizontal banding pattern (Section 3.11.1.1) that may be used to remove the pattern from images lacking dark sky.

In the NAC, the extended region of the readout register, and the first 13 columns into the serial register – i.e., samples 1–12 of the register – are corrupted by a grounding problem with the epoxy that bonds the pure silicon layer to the substrate. This causes spurious swings in the voltage during the initial ‘clockings’ of data out of the CCD into the signal chain. Consequently, the first 13 columns of NAC CCD data are unreliable, and the NAC's extended pixel region cannot be used to monitor the camera's bias or noise state (see Figure 27).

### 3.7. CAMERA COMMANDING AND TELEMETRY

The ISS accepts from the CDS blocks of commands which are then stored in camera memory to be executed at a later commanded ‘trigger’ time. Each block can be expanded in the ISS into commands to the camera electronics specifying camera modes, timings, and other data taking parameters. The internal ISS commands are executed within 5 ms of the start of the second following the arrival of a trigger command from CDS.

The acquisition of images can be accomplished in several ways. Individual NAC or WAC frames may be acquired, or the NAC and WAC can be used in simultaneous

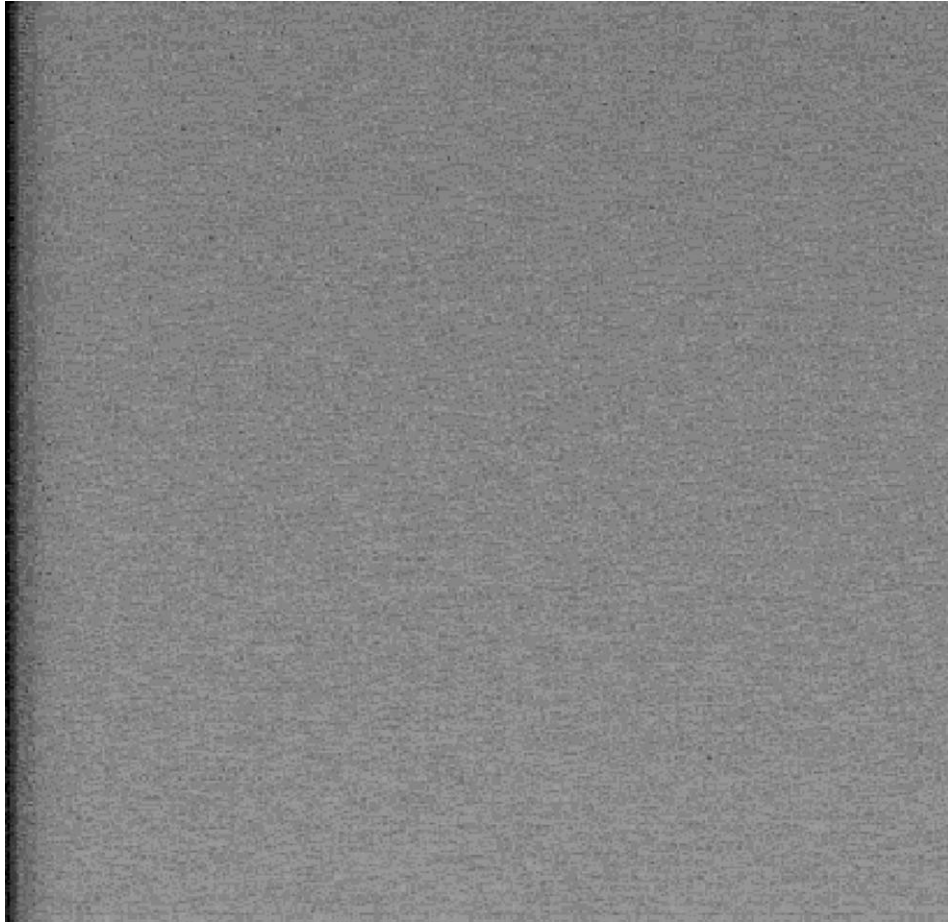


Figure 27. The dark band on the left of this NAC dark frame illustrates the lack of response in the first ~13 columns of the NAC CCD due to a grounding problem caused by improper bonding of the silicon epitaxial layer to the substrate of the CCD.

N A C W A C	Prepare Cycle							Read-out Cycle		
	Shutter Reset & 200 ms Pad	NAC Filter Wheel	Wait	Pad 325 ms	Wait	Flood & Erase	Exposure	NAC Read-out	Pad 262 ms	Wait
	Shutter Reset & 200 ms Pad	Wait	WAC Filter Wheel	Pad 325 ms	Wait	Flood & Erase	Exposure	Wait	WAC Read- out	Pad 262 ms

Figure 28. Diagram illustrating the breakdown of the ISS prepare and readout windows for a BOTSIM imaging mode into the various sub-windows and the activities that occur within each one. Note that the shutter close occurs at the same instance for the NAC and WAC, regardless of the exposure duration of each, and that the NAC is read out before the WAC. The NAC and WAC filter movement windows are also each segmented into sub-windows for separate movement of each of the two sets of filter wheels.



mode, called BOTSIM (for ‘both simultaneous’). The entire event, which is called a framing event and requires a total duration called a ‘framing time’, is broken down into two steps: the prepare cycle and the readout cycle.

The prepare cycle is used to alter the state of the ISS, step the filter wheels, perform heater operations, light flooding, and other functions required to prepare for an exposure. It also includes the exposure time. The prepare cycle is constructed from a series of quantized windows of time in which specific functions are assigned to occur. A simplified timing diagram is given in Figure 28.

During the prepare cycle, the shutter blades are reset from the previous exposure and the filter wheels are moved into position. Because simultaneous motion of each filter wheel requires more power than the ISS was allocated for peak operation, all filter wheels – NAC and WAC – are moved separately. Windows of quantized duration are set aside for the motion of each filter wheel. Next, the CCD is prepared for exposure to light. This preparation begins with a wait; the duration of the wait is chosen to ensure that the shutter will close exactly at the end of the quantized prepare window. After the wait, a light-flood fills the wells of the CCD to many (~50) times saturation, followed immediately by a readout. The entire light-flood/erase event takes 950 ms and has the effect of erasing any residual image of previous exposures from the CCD. Within 5 ms of the end of the light-flood/erase event, the shutter is opened for the commanded duration. (For dark frames, this duration is set to zero.) (Simultaneous imaging between NAC and WAC during a BOTSIM results in shutter close in each camera to within 10 ms of each other.) The image is tagged with the time of shutter close.

During the following readout window, the CCD is read out in the manner described in Section 3.6.1, the data are encoded and/or compressed, and the results are packetized.

(During a BOTSIM, the prepare cycle is lengthened to include time to prepare both NAC and WAC. The NAC is prepared first; then the WAC is prepared so as to avoid simultaneous movement of any of the four filter wheels. If the NAC and WAC exposure times are different, the exposures begin in a staggered fashion so that the NAC and WAC shutters are closed simultaneously. There are 63 discrete commandable exposure times which are accommodated within 13 discrete prepare cycle windows. This table is updatable in flight.)

For any of the six individual CDS pickup rates, there are four discrete readout windows for each camera. The readout window is scaled by the CDS pickup rate giving 24 actual readout windows per camera and 96 actual BOTSIM readout windows.

Prepare times and readout times are chosen before uplink. The prepare cycle is completely determinate; the readout time required to fully readout an image is not. The required readout time during the image event will depend on the amount of data being readout of the CCD, and the CDS pickup rate or on the line readout rate from the CCD, whichever is slowest (Section 3.9.4). If the data volume in the image was underestimated and the required readout time exceeds the commanded readout

time, the camera will cease reading out part way through an image and lines will be lost. For this reason, a great deal of effort has gone into estimating the amount of data returned for different scenes and choices of compression parameters. In-flight data, including data acquired during the Jupiter flyby, has proven essential in honing these estimates for Saturn tour planning.

The ISS can collect pixel (image) data, engineering data and status data, and packetize them with appropriate header information as either science telemetry packets (which include all types of data) or housekeeping packets (which only include engineering and status data). The latter are returned alone when ISS is in an ON power state but not actively taking images. The frequency with which housekeeping packets are collected is one packet per second and is programmable in flight. The amount of housekeeping data that gets sent to the ground is determined by the rate at which CDS picks up such packets and is currently one housekeeping packet every 64 s.

### 3.8. DATA PATHS

The analog-to-digital (A/D) conversion happens right as the analog signal is read-out from the chip, after it has passed through the on-chip amplifier. Data from the analog-to-digital converter (ADC) are encoded to 12-bit data numbers (DN), giving a dynamic range of 4096. However, they are stored as 16 bits: the upper 4 bits are all 1's. The ISS flight software masks the upper 4 bits when doing calculations. Compression and conversion functions are performed after the electrons are converted to DN. The next juncture is a choice of data conversion (from 12 to 8 bits) or no data conversion. Unconverted data can then proceed to a lossless compressor or undergo no compression at all. Converted data can undergo no compression or lossless or lossy compression. From there, the data are placed on the BIU, where they are ultimately picked up by the CDS and sent to the SSR where they are stored as 16-bit data. (Although each camera has its own BIU, CDS only listens to science packets from one address value for ISS. Thus, the ISS has the ability to switch the addresses between cameras so that the one being readout has the proper, CDS-recognizable value.)

### 3.9. DATA COMPRESSION

Serious constraints are imposed on imaging of the Saturn system by the limited data storage volume on the spacecraft's SSR, and by the limited communication bandwidth back to Earth. In order to make the most effective use of these resources, the Cassini imaging system includes the capability to convert the data from 12 to 8 bits (called data conversion), and also to perform either "lossless" or "lossy" image compression. Data conversion, and both lossless and lossy compression, are implemented in hardware.

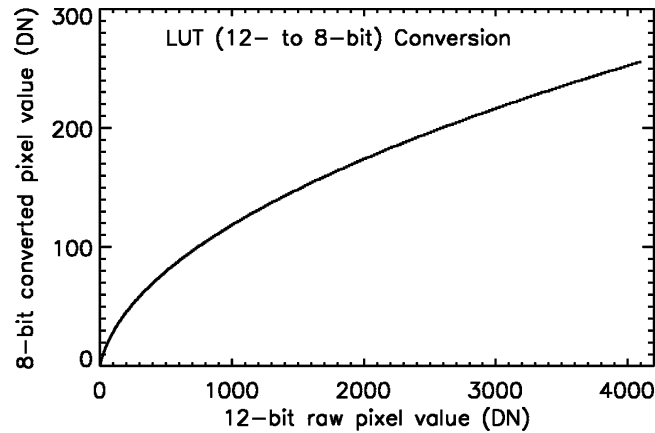


Figure 29. Diagram illustrating the function used to convert 12-bit data numbers into 8-bit values when the look-up table (LUT) conversion is used. The function is close to that of a square root function, and is often called the ‘square root encoder’.

### 3.9.1. Data Conversion to 8 Bits

Two sub-options are available for 8-bit conversion. One is a variant on conventional “square root” encoding. In such encoding, a look-up table (LUT) is used to convert the original data values to 8-bit values. The output 8-bit values are related to the input values in a nonlinear fashion, typically scaling with the square root of the 12-bit value. This nonlinear scaling more closely matches the quantization level to the photon shot noise so that the information content is spread more evenly among the 256 levels. The Cassini 12-to-8-bit conversion table is shown graphically in Figure 29. It differs somewhat from pure square root encoding, having been designed for the known noise properties of the Cassini cameras to distribute quantization-induced errors uniformly across the dynamic range of the system. The LUT is stored in ROM within the cameras’ memory and cannot be altered in flight; choice of ON or OFF is commandable in flight.

The other sub-option is conversion from 12 bits to the least-significant 8 bits (LS8B). This type of conversion is useful for reducing the data volume of images taken of very faint targets, such as diffuse rings or the dark side of Iapetus, which generally do not yield large signal levels and can be encoded to the lowest 8 bits. (This strategy is applicable only if there is no significant background or scattered light in the image.)

### 3.9.2. Lossless Compression

Both converted (8-bit) and unconverted (12-bit) data can be losslessly compressed. The ISS lossless hardware compressor is based on Huffman encoding, a high-efficiency, numerical encoding scheme in which the length of the bit sequence used to encode a given number is chosen based on the frequency of occurrence of that number. In ISS lossless compression, each compressed image can be reconstructed

on the ground with no loss to the information content of the image, provided the image entropy does not exceed the threshold where 2:1 compression is achieved. Scenes with low entropy will have compression ratios higher than 2:1; scenes with high entropy will never compress greater than 2:1, but the ends of lines will be truncated so that the total amount of data returned in a pair of lines of the image never exceeds the total number of bits for a single uncompressed line. The truncation scheme has been designed so that the truncation alternates – i.e., every other line – from one line to the next, on the right (large sample number) side of the image. If the data loss is great, it can in principle result in the complete loss of every other line. In either case, with this scheme information (though reduced in spatial resolution) can be retained across the image, even at the edges.

### 3.9.3. *Lossy Compression*

Imaging sequences requiring larger compression ratios than can be achieved with the lossless compressor may instead be more strongly compressed using the camera's lossy compression circuitry. This capability requires that the data have been converted to the 8-bit form. Consequently, data conversion must be employed first before the data are sent to the lossy compressor. Compression is implemented by a pair of specialized signal-processing chips manufactured by Matra Marconi Space and provided to Cassini by the French Centre Nationale D'Etude Spatiale (CNES). These chips perform a variation on the familiar Joint Photographic Experts Group (JPEG) compression algorithm used in many image transfer and storage applications.

The JPEG algorithm operates by selectively removing information from an image, particularly at high spatial frequencies, thus decreasing the amount of information that must be encoded, while retaining the most visually important details. The basic JPEG algorithm has four steps.

1. The image is subdivided into  $8 \times 8$  pixel blocks. Each pixel is "level shifted" by subtracting 128 from it.
2. The blocks are each subjected to a discrete cosine transform (DCT). This is analogous to the more familiar Fourier transform, in that it breaks the  $8 \times 8$  pixel block into spatial frequency components. The result is an  $8 \times 8$  array of cosine transform coefficients.
3. Information is selectively removed by dividing each array of transform coefficients by the values in a "quantization matrix". This is an integer divide operation, so the coefficients with the lowest values (usually at the highest spatial frequencies) tend to suffer the greatest information loss. The values in the matrix may be uniform, or may be weighted so as to preferentially eliminate information at chosen frequencies. An adjustable "scale factor" is used as a multiplier to the matrix. The scale factor determines the overall degree to which spatial frequency components are attenuated, and hence the compression ratio.

TABLE XI

The contents of the four Cassini compression parameter memory (PMEM) pages.

MALGO	TB	Page	Quantization Matrix	Huffman Table
0	0	0	Flat	Busy
1	0	1	Scaled	Busy
0	1	2	Flat	Sky
1	1	3	Flat	Atmospheric

The two parameters called MALGO and TB are single bits that are used in a camera command to specify the desired page.

4. The information remaining in the blocks is Huffman encoded and formatted for transmission. The overall reduction in data volume results from the very efficient Huffman coding that is possible for the requantized transform coefficients.

The Matra implementation of the JPEG algorithm makes use of four-parameter memory, or PMEM “pages”, numbered 0–3. Each PMEM page contains a quantization matrix, a table of scale factors, and a Huffman coding table. For any given image, a single page can be selected for image compression.

The four PMEM pages in the Cassini imaging system have been designed in the following fashion. In pages 0, 2, and 3, the quantization matrix is “flat”; i.e., each element has the same value. For page 1, the matrix is scaled to discard more high-frequency information. The table of scale factors is identical for pages 0, 1, and 3 but is different for page 2 (the ‘dark sky’ page). The Huffman tables for pages 0 and 1 are identical, and have been optimized for compression of “busy” images. This optimization was performed using a collection of real and synthetic CCD images of cratered surfaces and Saturn’s rings. The Huffman table for page 2 was optimized for images that are mostly black sky, and the Huffman table for page 3 was optimized for images of planetary atmospheres. Again, this optimization was performed using actual CCD images of black sky and atmospheric targets. Table XI summarizes the contents of the four Cassini PMEM pages.

In order to specify compression for a Cassini image, three choices must be made. The first is selection of the PMEM page, done by specifying two bits named MALGO and TB. The second is selection of the value of a parameter called  $B$ . The  $B$  values may range from 0 to 15, and are used to select the value from the scale factor table on the specified PMEM page. High  $B$  values yield higher compression ratios. A given  $B$  value generally selects a different scale factor when used with page 2 than it does with the other pages.

The final parameter that must be specified for compression is the “group of blocks”, or GOB, length. GOB length is a parameter that can range from 0 to 255, and that determines how frequently error correction headers are placed in the data

stream. If GOB length is 0, no headers are inserted. For other values, a GOB length  $L$  will cause error correction headers to be placed after each group of  $L$  image blocks. These headers allow an image to be largely recovered if there are noisy data but introduce some overhead in the bit stream, reducing the compression ratio with no improvement in image quality if no bit errors are present. Choice of GOB length must balance the desire for a high compression ratio against a desire for protection against bit errors. (In the event of transmission errors, all packets downstream of a lost packet are not recoverable in lossy compressed data.) GOB length is almost always chosen to be 41 for lossy-compressed Cassini images. Figure 30 illustrates the effect that lossy compression has on Cassini images.

#### 3.9.4. Readout Times

In the analysis of images, the time it takes the image data to be readout of the CCD is of interest because it relates to the buildup of dark current in the image. It is also of interest in the sequencing of images because, along with the duration of the prepare cycle, it determines the framing time, the time it takes to acquire an image and be ready for the next one.

The process of readout includes: (i) moving CCD lines into a 344,064 (16-bit) pixel image memory or buffer; (ii) moving CCD lines from image memory, converting them into science packets; (iii) moving science packets to the BIU memory; and (iv) CDS picks up packets at the BIU at the CDS pickup rate.

Imaging packets consist of 476 16-bit words or 7616 bits each, including headers. Twelve-bit (12-bit) pixels are placed in the least-significant end of a 16-bit word, so that each word represents a single pixel and a full-size ( $1 \times 1$ ), '12-bit' image consists of  $1024 \times 1024$  words = 2277 packets.

The CDS has various Science and Engineering Readout (S&ER) modes, each having a different rate of packet pickup by CDS. The cameras' rate of transmission of data to the CDS is synchronized to these rates. They can vary from 8 (S&ER2), 16 (S&ER1), 24 (S&ER3), 32 (S&ER6), 40 (S&ER5a) and 48 (S&ER5) data packets/s, defined by the CDS requirement for an integer number of packets during the unit of time, 1/8 s, employed by the CDS.

This translates into the following table of readout times, for *non-compressed images*, for the various summation and conversion modes in the cameras.

If CDS pickup rate were the sole factor in the CCD readout, Table XII would give accurate values of the readout times for uncompressed images; for compressed images, one could merely calculate the number of packets in the compressed image and divide by the CDS pickup rate to determine the readout time. However, there are other factors that come into play, making Table XII only partially correct.

In most cases – for example, a  $1 \times 1$  unconverted '12-bit' image – the CDS pickup rate is the rate-limiting factor in the data transfer to the spacecraft's SSR and the data must be buffered (or even wait on the chip before it is readout if the buffer is full) before the image is entirely picked up by the CDS. In such cases, the readout time from the buffer is merely the data volume divided by the CDS pickup rate.

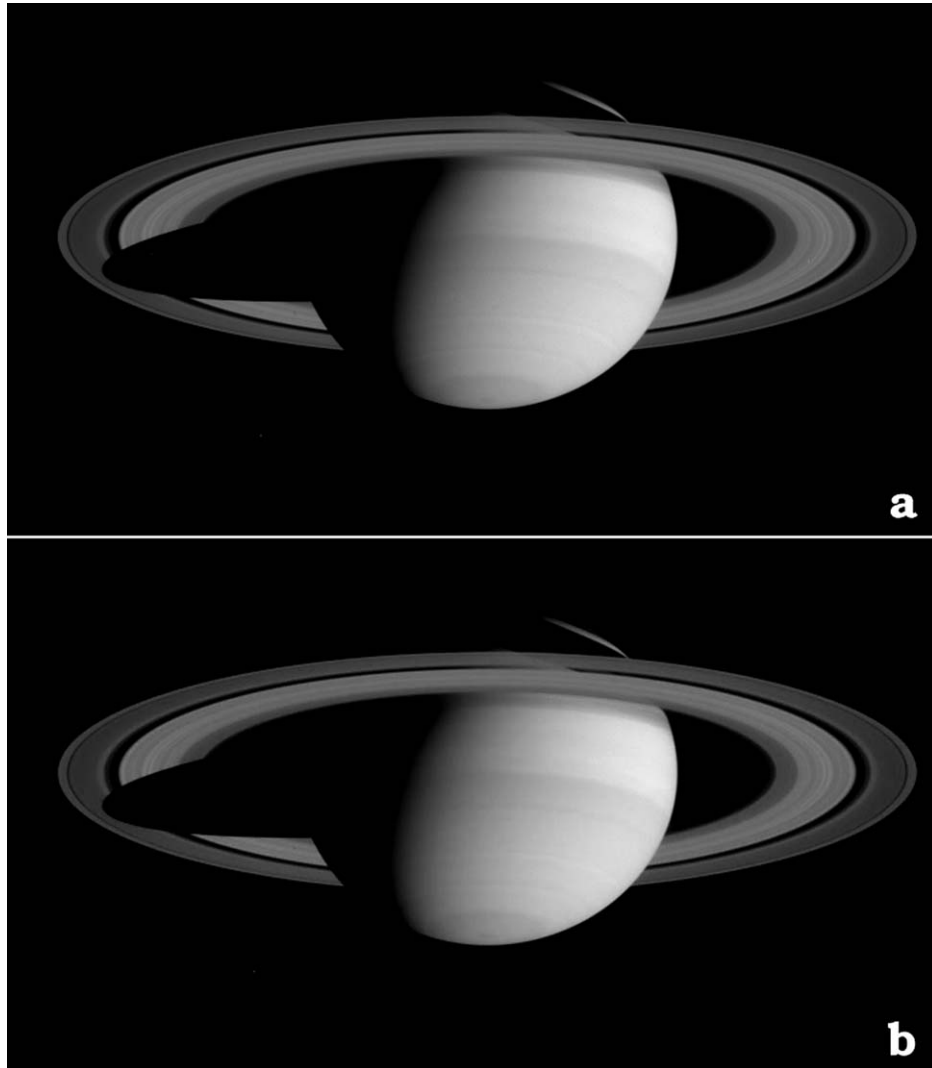


*Figure 30.* A set of two Saturn NAC images in the GRN filter showing both the planet and rings: (a) image acquired using lossless compression; (b) one taken with lossy compression. The lossy parameters chosen were  $B = 0$ ,  $PMEM = 0$ , and  $GOB = 41$ . The  $B = 0$  setting produces the least amount of compression. The full-disk images are linearly stretched between 40 and 180 DN. There is little obvious difference in the full-disk images. The next two images are a close up of a region south of the equator, stretched between 100 and 160 DN, in (c) the lossless compressed image (a), and (d) the lossy image (b). Note the presence of a dark atmospheric spot or storm near the left edge and its degradation under compression. Compression significantly reduces the quality of the image when viewed at this scale, and most scientific objectives (photometry, cloud tracking) would be hampered by use of lossy compression. The final two images are a zoomed view of the right ring ansa, stretched between 20 and 110 DN: (e) the lossless version (a), and (f) the lossy version (b). Here the  $8 \times 8$  pixel boxes (artifacts) are obvious especially in the bland areas. The other filters show very similar artifacts.

(Continued on next page)

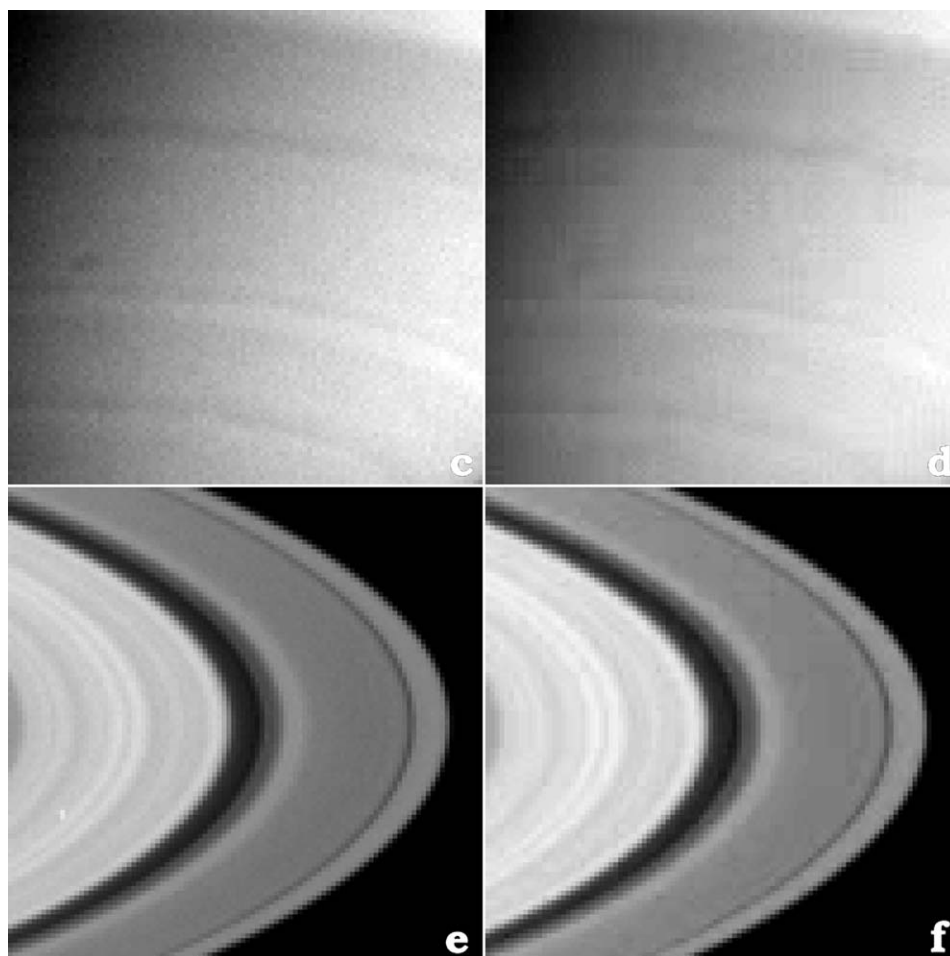


Figure 30. (Continued).

However, under certain circumstances, such as large compression factors (i.e., low data volume images) and fast pickup rate (48 packets/s), the CCD line readout rate into the camera buffer, which varies with summation, conversion, and compression modes, is the limiting factor in the data transfer and it is possible for the CDS data pickup to outrun the data stream from chip to buffer. For example, a  $1 \times 1$  losslessly compressed image cannot readout faster than approximately 12 s; a  $2 \times 2$  losslessly compressed image cannot readout faster than 6 s. In other words, the factor of 4 decrease in data volume in the latter case is not translated into a four times smaller readout time because of the limiting CCD line readout rate.

Finally, in the sequencing of images, a cardinal factor is the framing time: i.e., the sum of the prepare window duration plus the readout window duration. In the operation of the camera, both of these intervals come in quantized values. No matter



how fast the readout of the CCD, the shortest readout window available is 6.525 s. The shortest prepare cycle is 4.475 s. Thus, the shortest possible framing time in the Cassini ISS is 11 s (see Section 3.7).

### 3.9.5. Image Reconstitution

Once an image is telemetered back to the DSN and then sent on to JPL, it is reformatted from a series of data packets back into a two-dimensional image. In the reformatting process, the upper 1's in 16-bit unconverted, uncompressed data are converted to 0's. Images that had been compressed, either losslessly or lossily, are automatically decompressed in the reconstitution process before being sent to the Cassini Imaging Central Laboratory for Operations (CICLOPS) where they are ingested into the Archive Database (from which the Imaging Archive will be built). If they had been converted down to 8 bits by the LUT, a reverse LUT can be applied to them to restore them to their approximate full 12-bit values. (This will be an option in the Cassini ISS Calibration (CISSCAL) software that will be supplied to the PDS along with the Imaging Archive.) There is no way to restore an image previously converted to the eight lowest bits back to 12 bits unless one is confident of smooth gradients throughout the image. Further modifications can take place to clean them and convert them to physical units in the process of calibration (see Section 3.13).

## 3.10. RANDOM NOISE

There are several sources of noise in the ISS. Read noise is the electronic noise added to the signal as it is readout of the CCD and passes through the on-chip amplifier before it is converted to DN. In the Cassini ISS, great care was taken to

TABLE XII

The image readout times (in seconds) for uncompressed images and various choices of summation mode ( $1 \times 1$ ,  $2 \times 2$ , or  $4 \times 4$ ) and data conversion: i.e., no conversion or 12:8 conversion (either LUT or LS8B), under the assumption that the rate-limiting factor is the CDS pickup rate.

Summation	Conversion	Total no. of packets	Data pickup rate (kbits/s (packets/s))					
			365.6 (48)	304.6 (40)	203.1 (32)	182.8 (24)	121.9 (16)	60.9 (8)
$1 \times 1$	None	2277	47.44	56.93	71.16	94.88	142.31	284.63
$1 \times 1$	12:8	1143	23.81	28.58	35.72	47.63	71.44	142.88
$2 \times 2$	None	572	11.92	14.30	17.88	23.83	35.75	71.50
$2 \times 2$	12:8	288	6.00	7.20	9.00	12.00	18.00	36.00
$4 \times 4$	None	144	3.00	3.60	4.50	6.00	9.00	18.00
$4 \times 4$	12:8	74	1.54	1.85	2.31	3.08	4.63	9.25

minimize this noise. Its value is equal to  $\sim 12 \text{ e}^-/\text{pixel}$ , and in the highest gain state with  $13 \text{ e}^-/\text{DN}$ , is equal to 1 DN by design.

Shot noise, or Poisson or photon noise, is the noise in the photon stream hitting the detector and has the usual characteristics: the noise is equal to the square root of the signal. It is reduced to  $\sim 1$  DN in data converted with the LUT converter (Section 3.9.1), regardless of signal strength, because of the design of the LUT. The final outcome is that the bits that are lost in the conversion are the bits devoted to encoding the noise; the process is a lossless one.

### 3.11. DARK CURRENT

Dark current accumulates on the CCD in a manner that is dependent on many factors: readout rate, camera mode (BOTSIM versus single camera), summation mode, etc. Traditionally, dark current is thought to be the result of a defect in the sensor that produces a quasi-constant current which is sensitive to temperature but not to illumination. At the detector operating temperature of  $-90^\circ \text{ C}$ , most pixels have very low dark currents and so another source of electrons, called Residual Bulk Image (RBI), dominates the signal for dark (shutter-inhibited) frames. For practical reasons, we lump the electrons produced by both processes into a conceptual ‘dark current’ signal which must be subtracted before other calibration procedures can be applied.

RBI results from the leakage of trapped electrons. At the CCD operating temperature of  $-90^\circ \text{ C}$ , the time scale for the liberation of RBI electrons into the potential wells ranges from several seconds to several hundred seconds. This produces a latency effect. The chip has a memory of past illumination. To reduce the sensitivity to a negligible level of RBI to prior exposures, a procedure of light flood and erase is used whereby infrared LEDs ringing the CCD in each camera, centered in wavelength on 900 nm, saturate the CCD by approximately 50 times prior to every image to fill the traps. An erase cycle follows the light flood to remove any untrapped charge prior to the start of the next exposure. The light flood/erase cycle is the same for every exposure. By filling all traps, this procedure reduces sensitivity to prior exposures, but the RBI from the light flood itself must be removed. The resulting distribution of light-flood RBI electrons depends on many factors (including readout time) and this complicates the process of dark current removal.

The dark current (now defined to be the combination of the conventional dark current and RBI from light flood) will increase with the length of time that charge remains on the CCD. Because potential wells pickup charge as they are clocked down the chip, the dark current buildup is greater at large line (i.e.,  $y$ ) values than at smaller line values, resulting in a gradient across the chip. This is most important for pixels upstream of hot pixels or for short exposures when the charge leaking from RBI is greatest. If the data must be buffered (as in the  $1 \times 1$  mode), clocking is temporarily suspended, leaving the later lines of pixels on the chip. The result

is a discrete jump in dark current level at a particular line location, depending on the compressibility of the image (if compression was chosen). A much larger effect is the higher level of dark current in the potential wells that are halted at the two edges of the chip because of the large number of defects produced at those edges by the manufacturing process. Also, the number of hot pixels increases with time as cosmic ray damage increases so calibration dark frames need to be obtained and updated periodically.

This is sufficiently complex, and the various possibilities for dark current buildup and the number of different camera modes that determine dark current signal levels are sufficiently large, that it is impractical to do what many other imaging investigators have done and attempt to acquire dark current frames for every different scenario. Instead, an algorithm has been designed to estimate dark current buildup for every pixel on the CCD, using actual ground calibration and in-flight dark frames to determine, via standard least squares fitting, the parameters of the algorithm.

$$DN(t) = C + \alpha t + \sum \beta_I (1 - e^{-t/\tau_I}), \quad I = 1, 2, 3$$

where  $C$  is a constant which is negative for a few pixels at the left edge of the CCD,  $\alpha$  accounts for the true dark current, and the other six terms  $-\beta_I$  and  $\tau_I$ , with  $I = 1, 2$  and  $3$ —account for electrons produced by the light-flood which leak from traps during the readout. For the light-flood-trapped charge, three terms with different amplitudes and decay times are needed to simulate a distribution of trap sizes and decay rates. These eight terms must be determined separately for each pixel by a least-squares fit to dark images at a variety of exposure times.

This algorithm will be used to create a matrix of simulated dark frames that will be used to remove dark current buildup from real data.

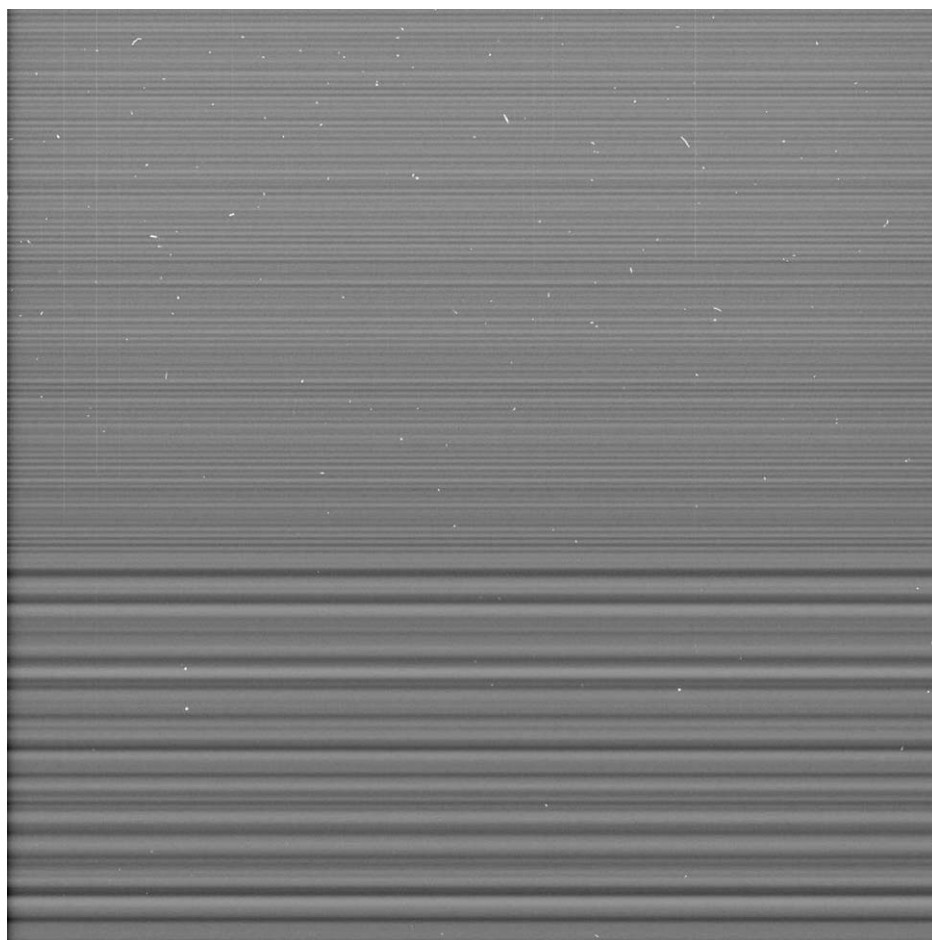
### 3.11.1. Coherent Noise

**3.11.1.1. Horizontal Banding.** Both NAC and WAC images exhibit a low-amplitude, coherent noise characterized by horizontal banding with significant power concentrated in a few spatial frequencies (Figure 31). The spatial frequencies present in the images depend on the readout rate from the CCD. The cameras did not show this problem until they were connected to the spacecraft in the Spacecraft Assembly Facility. The pattern is not fixed on the chip and is highly correlated with the over-clocked pixel value, indicating a fluctuation in the video bias level of the CCD. The changing amplitude of the banding (measured in DN) in various gain states is consistent with a constant amplitude in electrons; the dependence of the frequency content on readout rate is consistent with a constant temporal frequency. The source is unknown but is likely a ground-loop somewhere on the spacecraft.

Measurements indicate that the banding in the NAC has an amplitude of  $\sim 2.5$  DN in the  $13 \text{ e}^-/\text{DN}$  gain state (Gain 3); Fourier analysis shows mainly two frequency components, with the secondary peak having  $1/3$  the power of the main peak. After correction for the CCD readout rate, the main peak occurs at 2.1 Hz; the secondary

peak at 2.5 Hz. This produces a beating pattern with a combined frequency of 0.4 Hz. In the WAC, the amplitude is much smaller ( $\sim 0.5$  DN for the  $12\text{ e}^-/\text{DN}$  (Gain 3) state), with a dominant readout-corrected frequency of 4.0 Hz; two smaller peaks of 1/10th the power occur at 1.9 and 5.9 Hz.

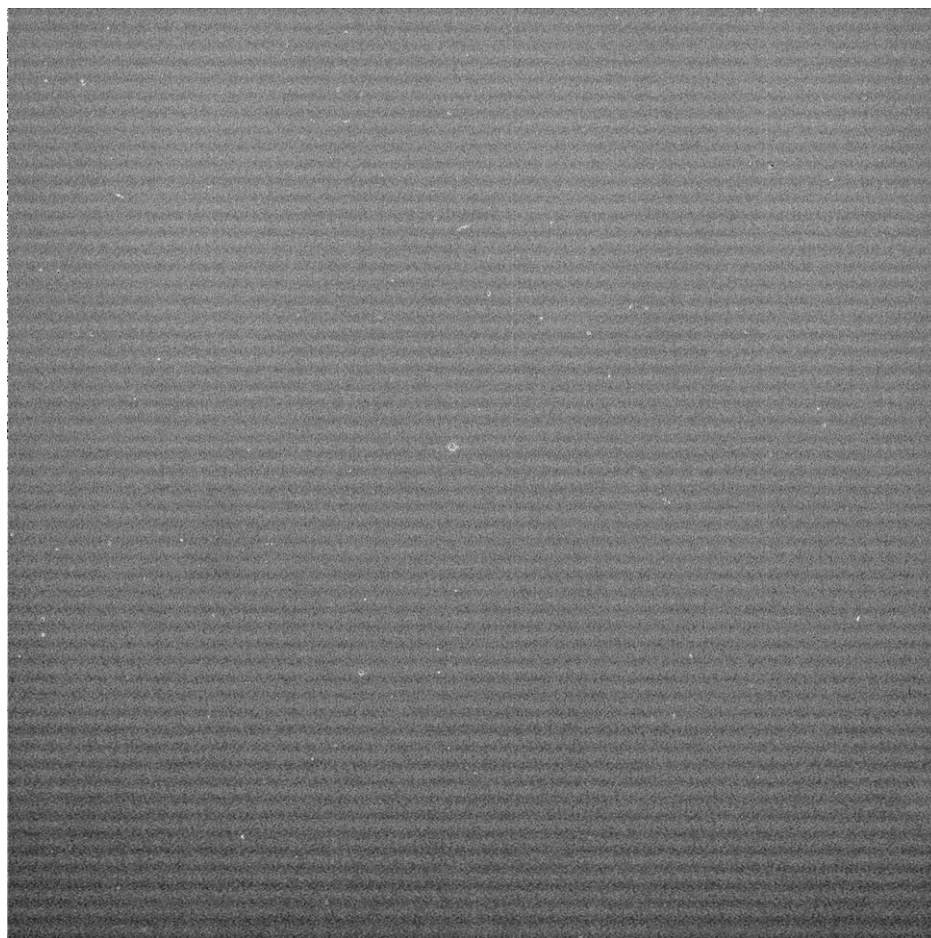
Calibration software being developed by the Imaging Team and within the Cassini Imaging Central Laboratory for Operations will contain algorithms designed to reduce this coherent noise in Cassini images without unacceptable damage to the image data themselves.



(A)

*Figure 31.* (A) Horizontal banding in the NAC is obvious at very low signal levels. The change in spatial frequency in this image is due to a change in readout rate from the CCD once the camera buffer is filled. Cosmic rays are evident. (B) The horizontal banding in the WAC.

*(Continued on next page)*



(B)

Figure 31. (Continued).

**3.11.1.2. Vertical Banding.** The ISS also exhibits other kinds of coherent noise and Figure 32 is an example of this. Irregular vertical banding of this type has been seen in many images; it seems to be absent in images that are readout in telemetry mode S&ER5. The source of the banding is presently unknown.

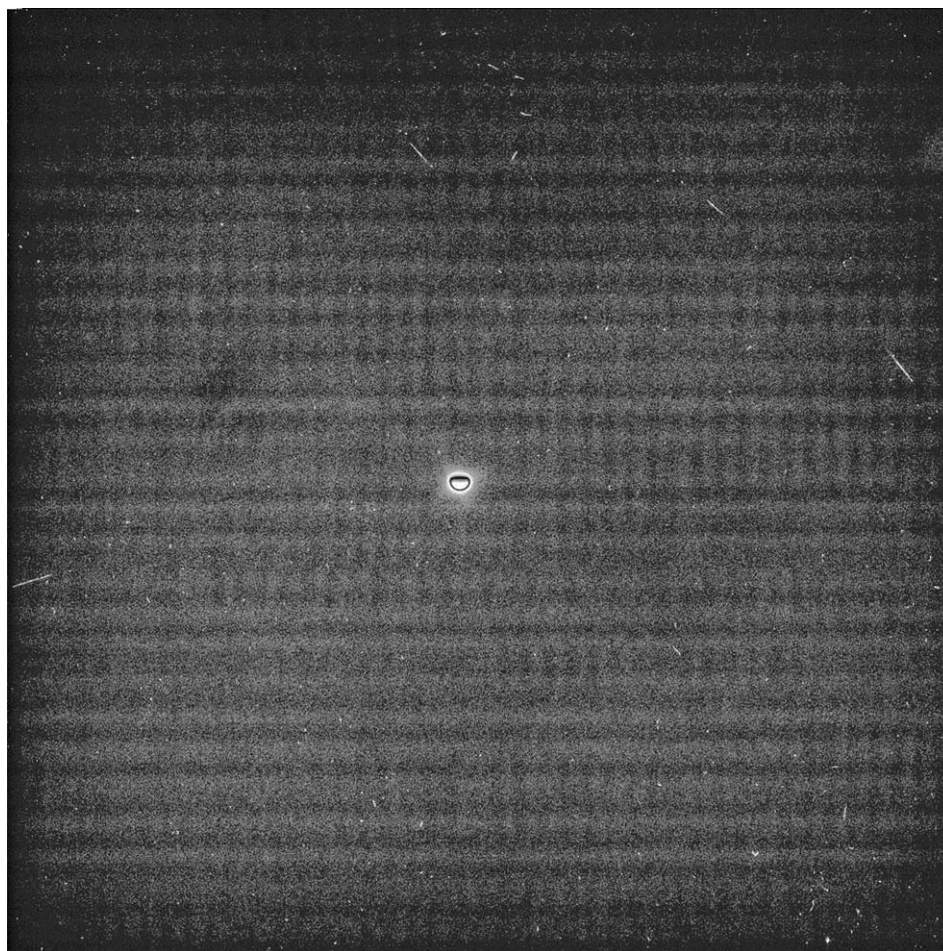
### 3.12. PERFORMANCE ON DIFFICULT TARGETS

#### 3.12.1. *Spacecraft Pointing Accuracy and Stability*

As the highest resolution imager on the Cassini Orbiter, the ISS is especially vulnerable to spacecraft jitter and pointing inaccuracies. The number of images needed to construct a gore-less mosaic depends on the accuracy of the absolute and relative spacecraft pointing. The quality of images and the detectability, especially of

difficult targets like unresolved satellites and very dark terrains on icy satellites, depend sensitively on how stable the spacecraft is during an exposure.

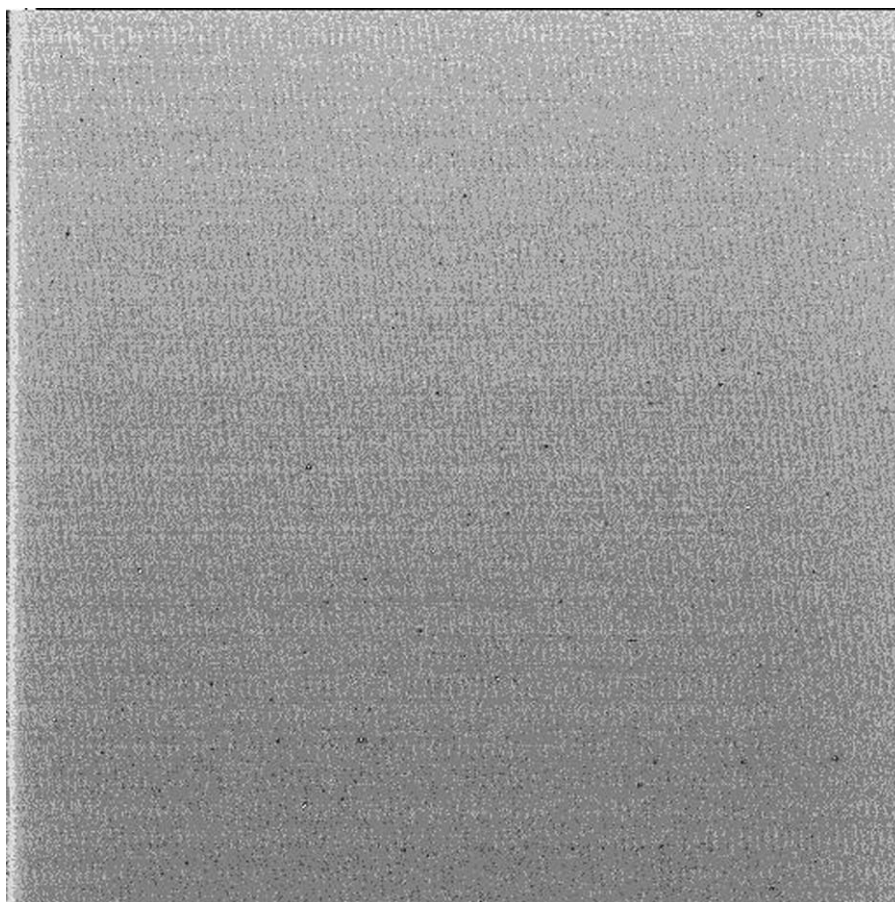
The absolute inertial attitude of the spacecraft is determined in flight by on-board algorithms which detect and measure the positions of stars observed in the Stellar Reference Units (SRU) or 'star trackers' on the RSP (Figure 14), and then calculate from star maps the orientation of the spacecraft. The SRU is deliberately out of focus so that the centroids of the stellar point response functions, which can be more precisely measured when de-focussed, can be determined to an ac-



(A)

*Figure 32.* Two examples of low-signal vertical banding. (A) A 38-s, gain state 2 (30 e-/DN),  $1 \times 1$ , unconverted, losslessly compressed narrow-angle camera image of Titan taken in April, 2004 and readout in S&ER3 pickup mode. (B) A 1-s, low gain state,  $2 \times 2$  summed, unconverted, uncompressed NAC image taken as part of a BOTSIM and readout in S&ER1 pickup mode.

*(Continued on next page)*



(B)

*Figure 32. (Continued).*

curacy of  $60 \mu\text{rad}$ , which in the SRU is 0.08 pixels. The FOV is  $15^\circ$ ; up to five stars are used in the navigation calculation. The boresight of the SRU is orthogonal to that of the ISS and pointed in the  $+X$  s/c direction. Rotation about the spacecraft  $Z$  s/c axis results in motion of objects in the line direction in the SRU and also in the line direction in the ISS. Thus, in the ISS line direction, inertial pointing can be controlled and determined to the SRU navigation quantization noise of  $</\sim 60 \mu\text{rad}$ .

However, motion of objects along the sample direction in the ISS is brought about by spacecraft rotation around the SRU boresight,  $+X$  s/c. Thus, to determine the boresight of the ISS in inertial space in the sample direction requires a measure of the twist of the SRU around its boresight. The accuracy and precision to which the latter can be determined depends sensitively on the distribution of the five stars used in the navigation calculation. If the five stars are clustered close to

the boresight and therefore provide a poor lever arm in the twist determination, the resulting angle will suffer greater uncertainty; the fact that the SRU exhibits barrel distortion, which when corrected can be as large as a pixel for stars near the edge of the field, means that even well-distributed stars can yield a relatively inaccurate value for the twist angle, and therefore for the sample location of the ISS boresight in inertial space. This systematic error will vary with the changing boresight position across the sky and with the orientation of the secondary axis around the boresight, since they determine the distribution of stars imaged by the square FOV of the SRU.

A further complication is that during long and continuous observing periods, when the spacecraft remains pointed at a single planetary target whose celestial coordinates as seen by the spacecraft are slowly changing, the star field imaged by the SRU will also change slowly. However, the discrete slippage of one star out of the SRU FOV and/or the entry of another can suddenly alter the *calculated* orientation of the spacecraft because of the effect mentioned earlier. This circumstance can masquerade as a delta function change in the inertial position of the ISS boresight. This was observed during Jupiter flyby.

The net result is that in absolute pointing, the differences between commanded and actual pointing of the Cassini orbiter can range up to 150 NAC pixels (or 900  $\mu\text{rad}$ ) in the sample direction – still an improvement over the 2 mrad pointing uncertainty for Voyager and for Cassini on thrusters – but is  $\leq 60 \mu\text{rad}$  in the line direction, equal to the quantization noise in the SRU calculation of orientation of the spacecraft. The relative pointing of the spacecraft is good in both directions:  $\sim \leq 50 \mu\text{rad}$ .

Once pointed, the orientation and direction of the spacecraft is remarkably steady when on reaction wheels. Exposures as long as 32 s on stars resulted in less than 6  $\mu\text{rad}$  (i.e., 1 NAC pixel) of smear. In images taken of the star Fomalhaut in September 2000, the pointing of the NAC over 50 min varied by only 18  $\mu\text{rad}$ , or three NAC pixels. Images of Saturn in the UV, taken on approach to orbit insertion, were acquired with 320-s exposure times and showed no noticeable smear.

Ironically, these values far exceed the initial advertised capability of the High-Precision Scan Platform on the original Mariner Mark II spacecraft, and are due to the large inertia of the Cassini spacecraft and the reaction wheels which maintain its orientation.

### 3.12.2. Point Spread Function

*3.12.2.1. In-Flight Calibrations.* The camera optics and filters cause some spreading of the images of point sources. The PSFs for both NAC and WAC were measured prior to flight; they were also measured in flight using the stars in the cluster M35 in the constellation Gemini. In 1-s images taken through the clear filters in both cameras, using unconverted (12-bit), unsummed data modes and a gain state of 29  $e^-/\text{DN}$ , images of stars were fitted by a two-dimensional



Gaussian function, with the height and width as adjustable parameters. (A Gaussian function is not an exact match to the shape of the PSF, but a least-squares fitting using one does an adequate job of measuring dimensions.) The FWHM of the fitted functions were 1.3 pixels through the NAC clear filter and 1.8 pixels through the WAC clear filter; the RMS residuals in the fits are below 0.06 pixels, with no sign of obvious trends in the results with changing position on the CCDs.

*3.12.2.2. NAC Haze Anomaly of 2001.* In May 2001 (Day 150), in NAC images taken of the Pleiades, a diffuse circular halo appeared around the central peak of the image of Maia; WAC images were not likewise degraded. The apparent cause of this anomaly was the resumption of normally scheduled decontamination cycles after a 13-month hiatus. Decontamination is a process by which the two heaters, attached to each of the radiators of the NAC and WAC cameras and specially placed for such activity, are turned On and heat the CCD. The purpose is to “bake off” any contamination that may have condensed on the cold parts of the instrument. The May cycle was the first in flight to cover a particularly large range in temperature – from the  $-90^{\circ}\text{C}$  operating temperature up to  $-30^{\circ}\text{C}$  for 16 h – and was the first after the Jupiter encounter. The halo size and intensity were wavelength dependent: the intensity of the brightest part of the halo was only 1–2% of the central peak, but because of its spatial extent, contained 30–70% of the light of the star. The properties of the PSF were consistent with contamination by very small particles on a transmissive surface causing a diffraction pattern in images of point source objects. The source of this contamination has not been identified but may have been something in the camera’s environment that outgassed during the May 2001 decontamination cycle and subsequently condensed on the CCD, either the window or the CCD itself.

The Instrument Operations team at JPL responsible for the health and safety of the ISS conducted additional conservative decontamination cycles, carefully designed to take small increments in temperature between test imaging. These occurred in October 2001 and January 2002, each for a week. A third began on March 5, 2002 and lasted 57 days, and a fourth began on May 9 and lasted for 60 days. After the third cycle, the haze disappeared leaving the point response function of the NAC within pre-anomaly limits; no significant improvement has been seen since then. The quoted values for the NAC point response function are those determined in flight after haze evaporation. Figure 33 shows images of stars taken before the anomaly appeared, during its presence, and then after it disappeared.

### *3.12.3. Detectivity of Point Sources*

The detectivity of point sources with a space-based imaging system depends critically on the photometric sensitivity of the detector, the throughput of the imaging

device, and the stability of the spacecraft. The noted stability of the Cassini spacecraft when stabilized on reaction wheels has translated into a surprisingly good capability to detect faint point sources. This is an important characteristic when the goal is to search for previously undetected satellites.

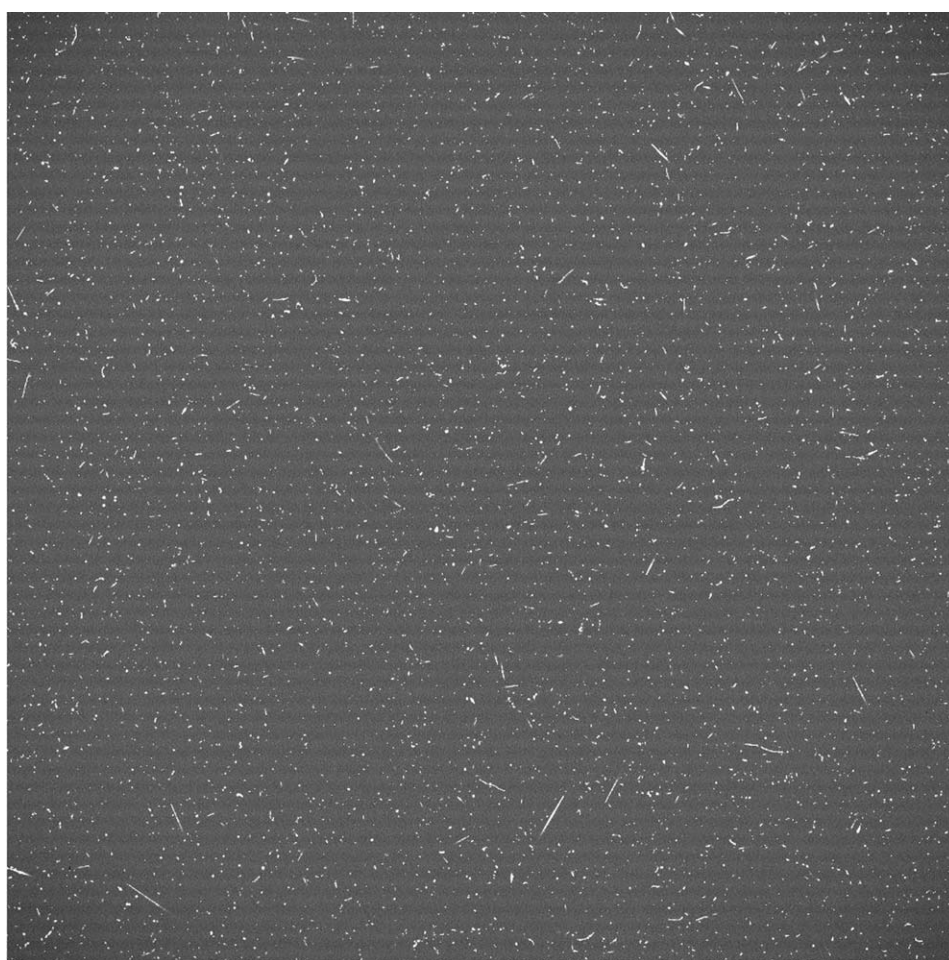
In NAC images of the open cluster M35 in Gemini, taken for purposes of calibrating the geometric fidelity and point response of the cameras, the limiting magnitude for losslessly compressed 12-bit images in gain state 2 was  $M_v \sim 14$  in 1 s through the clear filter. When the images were converted first to 8 bits and then sent through the lossless compressor, the limiting magnitude became  $M_v \sim 13$  in the NAC clear filter for a 1 s exposure. The brightest stars in these images were  $M_v = 6.3$  and were not saturated. In the WAC, the limiting magnitudes in 1 s in losslessly compressed 12- and 8-bit images were  $\sim 11.6$  and  $10.6$ , respectively; the brightest unsaturated star was  $M_v = 3.4$ .

At Saturn, these numbers imply a detection limit for new unresolved satellites in unconverted images (12-bit) in the absence of a severe scattered light background given by  $I/F r^2/D^2 \sim 4.3 \times 10^{-15}/t$  (s) in the NAC, and  $\sim 3.9 \times 10^{-14}/t$  (s) in the WAC, where  $I/F$  is the phase-corrected reflectivity of the object,  $D$  the distance of Cassini from the object,  $r$  the object's radius, and  $t$  (in seconds) is the residence time of the object in a pixel or the exposure time, whichever is shorter. Given the remarkable stability of the spacecraft on reaction wheels – i.e., a variation of only three NAC pixels over 50 min – the detection limit for small unseen bodies would appear to be affected by the amount of time one has to observe, the relative motion of spacecraft and object, including its orbital motion, which will ultimately determine the residence time in a pixel, and the desire to keep the confusion of cosmic ray hits to a minimum (see Figure 34.) However, scattered light can be a serious limiting factor when observations are made close to Saturn (Figure 35). Detection limits for small satellites between the orbits of Rhea and Hyperion, a region being searched on approach to Saturn when the phase



*Figure 33.* The figure above show stellar images taken before the anomaly, one image taken after the anomaly surfaced, and three taken after the decontamination sequences, all in the same BL1/CL2 filters and adjusted for total stellar brightness. The images are all contrast enhanced in the same manner to show the faint extended light. All images were taken at a CCD temperature of  $-90^\circ$  C. Calculations indicate that for this filter combination, approximately 68% of the light fell outside a radius of five pixels when the anomaly was at its maximum. After the first sequence (third image above), that fraction was reduced to 44%; after the second (fourth image above), 18%. It is now 5% (fifth image above). . . back to pre-anomaly values.

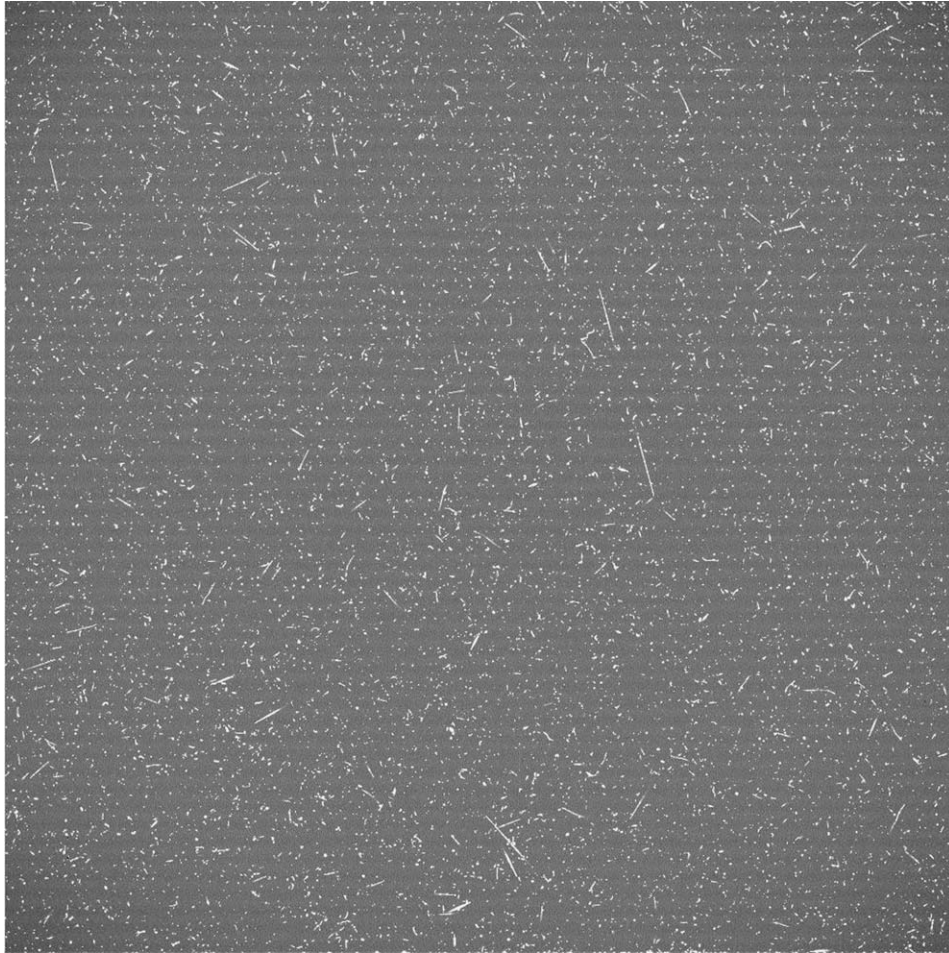
angle is  $\sim 70^\circ$ , are expected to be  $r \sim 3$  km in 82-s NAC exposures for objects with a geometric albedo equal to that of Hyperion (0.3). During observations designed to search for ring-embedded moonlets when the pixel residence time is limited by the rapid orbital motion, moons observed at low phase with  $r \sim 1$  km and a geometric albedo equal to that of typical ring particles should be easily detected.



(A)

*Figure 34.* (A) A 560-s dark exposure in the WAC. (B) A 1200-s dark exposure in the WAC. In both, the 100-DN background and cosmic rays are evident.

*(Continued on next page)*



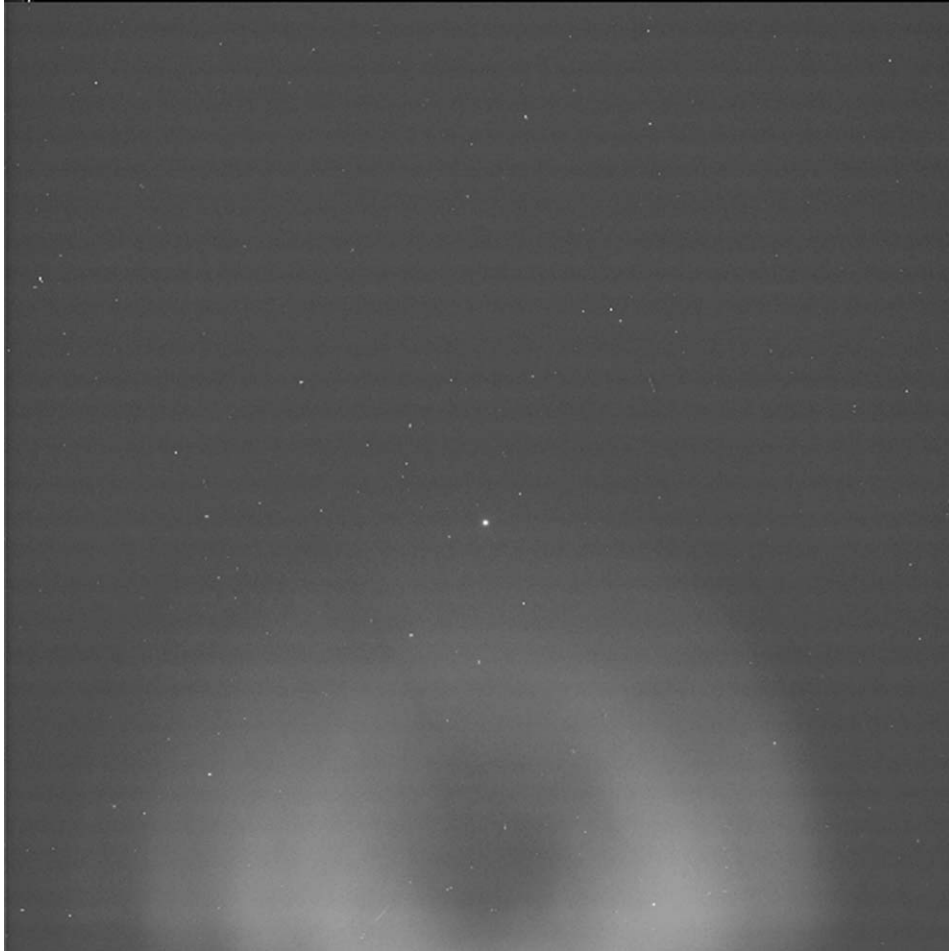
(B)

*Figure 34. (Continued).*

#### 3.12.4. *Expected Performance on Diffuse Sources*

The detectivity of diffuse sources, such as tenuous rings like the E and G rings of Saturn, depends less on spacecraft stability than on the CCD dynamic range, noise sources, photometric sensitivity, the light scattered from nearby bright sources (like Saturn's main rings) into the camera, and the desire to keep the number of cosmic rays in the image to a minimum. The latter can be a big problem for very long exposures (Figure 34), and the scattered light can be a big problem when the angular distance to a bright source is small (Figure 35). Because of these effects, typical exposures to search for new diffuse rings, and to characterize the ones already known to be there, will be a hundred seconds or less, and will generally utilize the summation mode for increasing signal to noise when the resolving capability

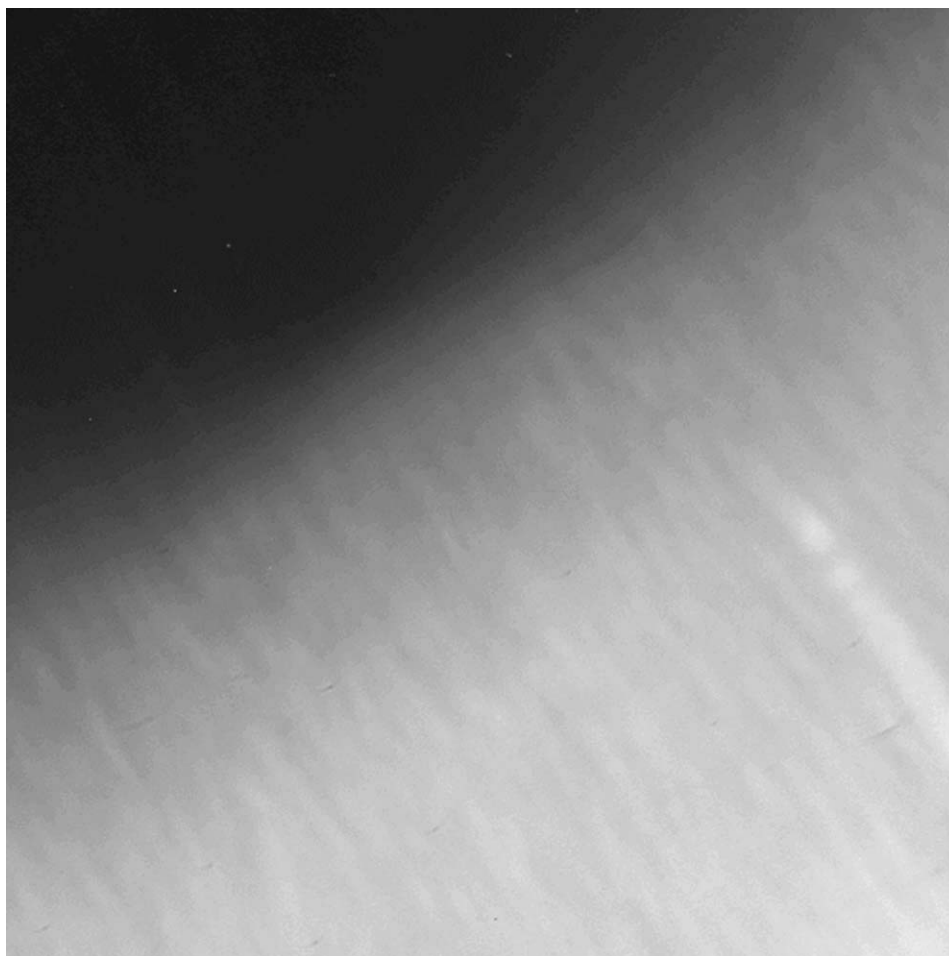
can tolerate it. Polarizers for potentially separating out generally polarized light reflected from natural ring particles from unpolarized light scattered in the optics will also be employed. Such exposure times may give a detection limit of better than  $I/F \sim 10^{-9}$  with a  $S/N \sim 10\text{--}30$  for those circumstances where scattered light is not a factor; i.e., when Cassini is in at close range and the angular distance to



(A)

*Figure 35.* (A) An 18-s narrow-angle camera image, one in a series of satellite search images taken close to the planet's rings (off the bottom of the frame) in the CLR filter, using lossless compression,  $1 \times 1$  mode, gain state 3 (i.e., high gain state). The 2-Hz pattern is apparent. The pattern at the bottom of the frame is light scattered off the NAC's secondary mirror and its supports. (B) A 320-msec WAC image taken through the BL1 filter, about  $20^\circ$  away from the Sun, illustrating the structure present in the image of the light scattered in the WAC optics.

*(Continued on next page)*



(B)

*Figure 35. (Continued).*

Saturn is large. We thus expect the Cassini ISS to have the ability to detect diffuse rings several hundred times fainter than G ring.

### 3.13. CALIBRATION

This section describes the relationship between measured signal,  $S$  ( $e^-/\text{pixel}$ ), the corresponding image values or data numbers (DN), and incident intensity  $I$ , and outlines the steps required to derive  $I$  from the DN values. (Most filters are not sensitive to the polarization state of the target, and so the methodology outlined later neglects polarization. Polarization must be taken into account when polarizing filters are used.) Definitions used in this section are given in Table XIII.

TABLE XIII  
Calibration definitions and units.

Quantity	Units	Definition
$\Omega$	Steradian	Solid angle sampled by one pixel
$A$	$\text{cm}^2$	Collecting area of camera optics $0.25 \pi d^2$ , $d$ is the primary mirror or lens diameter
$C(f_1, f_2)$		Absolute sensitivity correction factor determined from in-flight calibration
$e_p(i, j)$	Electrons	Electrons produced by photons striking the CCD
$f_1, f_2$		Filter 1 in wheel 1, filter 2 in wheel 2
$FF(i, j, f_1, f_2)$		Flat field relative sensitivity
$g$	Electrons/DN	Gain constant (Table X)
$I(i, j, \lambda)$	Photons/( $\text{cm}^2 \text{ s nm steradian}$ )	Intensity at pixel $(i, j)$ and $\lambda$
Line		The vertical coordinate (1:1024) of the image. Index $j$ indicates line number
$QE(i, j, \lambda)$	Electrons/photon	CCD quantum efficiency
$RBI(i, j, \text{mode})$	DN	Residual bulk image
Sample		The horizontal coordinate (1:1024) of the image. Index $i$ is used in this document for sample number
$t(i)$	Seconds	Shutter open time, depends on sample number
$T_0(i, j, \lambda)$		Optics transmission. Accounts for beam obscuration as well as losses at lens and mirror surfaces
$T_1(i, j, \lambda)$		Filter 1 transmission
$T_2(i, j, \lambda)$		Filter 2 transmission

### 3.13.1. Methodology

To understand the processes involved in calibration, it is useful to follow the light as it travels through the optical system, is converted to an electric signal and a data number and then is processed by the digital electronics.

The light that hits the CCD first passes through the camera optics and two filters, and the shutter. As a result of this process, the number of photons incident on one pixel at location  $(i, j)$  is  $A\Omega t(i) I(i, j, \lambda) T_0(i, j, \lambda) T_1(i, j, \lambda) T_2(i, j, \lambda)$ . Note that the exposure time depends on sample number ( $i$ ) because the shutter velocity across the CCD is not uniform. Note also that the actual shutter open time differs significantly from the commanded time for one of the exposures on each camera (20 ms for the WAC and 25 ms for the NAC).

Some of the photons (a fraction  $QE(i, j, \lambda)$ ) that strike a pixel will be converted to electrons. The number of electrons generated by photons is given by

$$e_p(i, j) = A\Omega t(i) \int I(i, j, \lambda) T_0(i, j, \lambda) T_1(i, j, \lambda) T_2(i, j, \lambda) QE(i, j, \lambda) d\lambda \quad (1)$$

The optics and filter transmissions have spatial dependence because of low spatial frequency components (e.g. vignetting) and high spatial frequency components (dust particles). Calibration measurements are not able to determine the source of the spatial variations and so all spatial variations are combined and taken out of the wavelength integral. Henceforth, we will call this combined relative spatial dependency  $FF(i, j, f_1, f_2)$ . It is obtained with flat-field calibration measurements. It is a relative dependency because it is normalized to unity, i.e.  $(1/N^2) \sum_{j=1}^N \sum_{i=1}^N FF(i, j, f_1, f_2) = 1.0$ . The dependence on  $f_1$  and  $f_2$  reflects the fact that the FF depends on the filters 1 and 2. Then Equation (1) becomes

$$e_p(i, j) = C(f_1, f_2) A \Omega t(i) FF(i, j, f_1, f_2) \int I(i, j, \lambda) T_0(\lambda) T_1(\lambda) T_2(\lambda) \times QE(\lambda) d\lambda \quad (2)$$

In Equation (2),  $T_0(\lambda)$ ,  $T_1(\lambda)$ , and  $T_2(\lambda)$  refer to transmissions averaged over the focal plane. These were measured as part of the calibration procedure. A new term  $C(f_1, f_2)$  was introduced into Equation (2). It is a correction factor to account for the fact that there are errors in the calibration measurements of absolute sensitivity. This factor will be determined from in-flight absolute calibration of standard stars and other objects whose radiometric flux or intensity is independently calibrated. If the ground calibration measurements are accurate it should be close to unity.

Other processes add to or reduce the number of electrons in a pixel. Residual bulk image (RBI) from light flood/erase cycle, and (at a very low level) previous exposures, and dark current add electrons. If anti-blooming is on electrons can be shifted from one pixel to an adjacent pixel containing traps. The pixel with the traps will accumulate electrons at the expense of its neighbor. The neighbor is always the adjacent pixel in the line direction.

Dark current is usually negligible except at the edge of the image. However, an uncompressed unsummed ( $1 \times 1$ ) image will readout partially into memory and then wait since the camera memory cannot store an entire image. If the bus rate is low, the remaining image may sit on the CCD for many seconds. During this time, dark current at the edge of the frame builds up. Since the image is only partially readout, former line 337 waits at the edge of the CCD where dark current builds rapidly. Which line waits at the edge of the frame depends on the data rate and possibly also whether compression is used. Line 337 was observed to have bright pixels in uncompressed calibration frames taken in the laboratory, all at a rate of 60.9 kbits/s. All lines after 336 contain enhanced RBI electrons from the time spent waiting.

The RBI from the part of the image remaining on the chip also builds up. Therefore, the resulting dark current and RBI pattern has a complicated spatial structure and depends on how the chip was readout, which in turn depends on the data rate, the summation mode, exposure time, which camera was read first after simultaneous shuttering, and compression. To remove the unwanted signal,



one would either take a series of dark frames in each mode used during the image sequence (potentially requiring large data volumes and long observation times) or produce these from a model of the dark current as described earlier. We have chosen the latter. Here, mode refers to all the factors that influence the time spent on the chip and the read pattern. These factors include exposure time, summation mode, compression mode, framing time, readout rate, etc.

The CCD contains a summation well. On-chip summation of  $2 \times 2$  or  $4 \times 4$  pixels can be commanded. Data volumes in these summation modes are small enough that the entire chip can be read to memory.

Voltages on the chip are set so that the zero level (no electrons in the pixel) will produce a positive DN value. This is called the bias level. It should not change except over long periods or after a voltage reset. It can be measured for each frame from the over-clocked pixels. Calibration data taken in the thermal vacuum chamber revealed that the bias level, as revealed by over-clocked pixels, increases with increasing exposure time. The reason for this is unknown. For gain state 3, the bias level is a function also of the electronics temperature. To ensure that the correct bias level is subtracted, the bias level should be obtained from the over-clocked pixels for each frame. The best measure of the bias level is to average as many over-clocked pixels as possible.

The summation well is deep enough to accommodate  $2 \times 2$  summation moderately well, but is not adequate for  $4 \times 4$  summation in the lowest gain state. DN values above about 1600 in the lowest gain state depart from the linear coefficients derived from low DN levels. Nonlinearity is noticeable in other gain states as well. It is least severe for the highest gain state. A quadratic term was derived from linearity test data, and the calibration procedure applies a quadratic-term correction to extend the DN range over which the calibration is good to 1% or better. For  $1 \times 1$  and  $2 \times 2$  summation the entire range of the 12-bit readout can be corrected to better than 1%. In these modes all unsaturated pixels are calibrated. For  $4 \times 4$  summation with gain 0, a separate file containing maximum allowed DN needs to be checked to make sure the DN value for any pixel is not above the DN range over which calibration is accurate to 1% or better.

The electrons on the CCD are shifted to an output register and then to the ADC. The ADC introduces a slight error in the DN levels because of a process called uneven bit weighting. Instead of a one-to-one linear correspondence between input signal and output DN, some of the DN values are under-populated and some are over-populated. Four gain states are available. The uneven weighting is different for each of the gain states.

Data from the ADC are 12-bit numbers. These can be sent to memory or passed through one of the 12-to-8 tables. One of the tables approximates a square root function. The other takes the eight least-significant bits.

Eight-bit data can be passed through one of two compressors. One is a lossless Huffman compressor. The other is a lossy cosine transform compressor.

Radiometric calibration requires the following steps, which reverse the effects of each of the processes listed earlier.

1. Decompression if compression was used. (This step is performed at JPL before images are available to the Imaging Science team.)
2. Conversion from 8- to 12-bit words if a 12-to-8 table was used.
3. Correction for uneven bit weighting using a table appropriate for the gain state.
4. Bias subtraction using over-clocked pixel values (average of many to improve statistics).
5. Removal of the coherent horizontal banding using as a representative source of the noise signal, either the over-clocked pixel values for each line or some mean taken from the image itself. (The latter is used when there is black sky in the image with which to measure the banding signal.)
6. Subtraction of appropriate dark frame containing RBI and dark current corresponding to the exposure time, summation mode, gain state, and readout mode of the image. This frame has had its own bias value already subtracted and may contain some negative DN values.
7. Correction for bright/dark differences in anti-blooming mode.
8. Correction for nonlinearity for the appropriate gain state.
9. Correction of static blemishes on the CCD ('bad pixels').
10. Multiply by the gain constant  $g$ . The result will be  $e_p(i, j)$  as given by Equation (2).
11. Divide the frame by the factors  $C(f_1, f_2)A\Omega t(i)FF(i, j, f_1, f_2)$ .
12. Divide the image values by  $\int T_0(\lambda)T_1(\lambda)T_2(\lambda)QE(\lambda)d\lambda$ .  
The resulting image will be an array of intensities averaged over the passband of the filter with a weighting function  $T_0(\lambda)T_1(\lambda)T_2(\lambda)QE(\lambda)$ .
13. The quantity  $I/F$  is often desired for solar system objects, where  $\pi F$  is the incident solar flux. The appropriate value of  $F$  is the passband-averaged  $F$  weighted the same way as the intensity, namely

$$F = \frac{\int F_1(\lambda)T_0(\lambda)T_1(\lambda)T_2(\lambda)QE(\lambda)d\lambda}{\pi R^2 \int T_0(\lambda)T_1(\lambda)T_2(\lambda)QE(\lambda)d\lambda}$$

In the above equation  $F_1$  is the solar flux at 1 AU and  $R$  is the distance between the sun and target body in AU.

14. Interpolate over isolated saturated pixels or pixel-pairs from anti-blooming, if desired. All saturated pixels are identified and stored in a separate file.

### 3.13.2. *Calibrated Photometric Performance on Resolved Targets*

At the time of writing, the calibration of the ISS is not complete, and more in-flight data are required. However, we have preliminarily calibrated the most useful filters and filter combinations and the results have been cast in terms of a simple relation giving the signal,  $S$ , in  $e^-/\text{pixel}$ , as a function of the exposure time,  $t_{\text{exp}}$ , and the  $I/F$

TABLE XIV

The factor,  $\omega_0^{\text{NAC}}$ , relating the brightness of the target,  $I/F$ , to the signal,  $S$  (electrons/pixel), and exposure time in the NAC camera.

F1	F2	$\lambda_{\text{cen,NAC}}$	$\lambda_0^{\text{NAC}}$
UV1	CL2	258	3.54E+02
UV2	CL2	298	2.59E+03
UV2	UV3	316	1.43E+03
CL1	UV3	338	1.54E+04
P120	UV3	341	4.96E+03
P60	UV3	341	5.15E+03
P0	UV3	341	5.98E+03
CL1	BL2	440	1.74E+04
P120	BL2	440	5.89E+03
P60	BL2	440	5.96E+03
P0	BL2	440	6.49E+03
BL1	CL2	451	8.41E+04
BL1	GRN	497	4.99E+03
CL1	GRN	568	3.49E+05
P120	GRN	569	1.14E+05
P60	GRN	569	1.20E+05
P0	GRN	569	1.21E+05
RED	GRN	601	1.43E+05
CL1	CL2	611	1.26E+06
IRP0	GRN	614	3.69E+04
P120	CL2	617	3.90E+05
P60	CL2	617	3.90E+05
P0	CL2	617	3.90E+05
CL1	MT1	619	1.10E+04
P120	MT1	619	3.71E+03
P60	MT1	619	3.71E+03
P0	MT1	619	3.71E+03
IRP0	MT1	619	4.62E+03
CL1	CB1	619	6.06E+04
P120	CB1	620	2.03E+04
P60	CB1	620	2.03E+04
P0	CB1	620	2.03E+04
IRP0	CB1	623	2.19E+04
RED	CL2	650	4.20E+05
HAL	CL2	656	2.64E+04
RED	IR1	702	1.31E+05

(Continued on next page.)

TABLE XIV  
(Continued.)

F1	F2	$\lambda_{\text{cen,NAC}}$	$\lambda_0^{\text{NAC}}$
CL1	MT2	727	1.24E+04
IRP0	MT2	727	6.07E+03
P120	MT2	727	5.37E+03
P60	MT2	727	5.46E+03
P0	MT2	727	6.00E+03
P120	IR1	740	1.71E+05
P60	IR1	740	1.71E+05
P0	IR1	740	1.71E+05
IRP0	CL2	746	4.30E+05
CL1	CB2	750	2.75E+04
IRP0	CB2	750	1.34E+04
P120	CB2	750	1.27E+04
P60	CB2	750	1.27E+04
P0	CB2	750	1.27E+04
CL1	IR1	752	3.92E+05
IRP0	IR1	753	2.03E+05
IR2	IR1	827	4.53E+04
IR2	CL2	862	1.32E+05
CL1	MT3	889	1.06E+04
IRP0	MT3	889	5.30E+03
IR2	IR3	902	4.06E+04
CL1	IR3	930	6.70E+04
IRP0	IR3	930	3.63E+04
CL1	CB3	938	4.70E+03
IRP0	CB3	938	2.53E+03
IR4	IR3	996	6.12E+03
IR4	CL2	1002	7.20E+03

of the target for these filters and combinations. This relation, computed for targets at the heliocentric distance of Saturn (i.e., 9.14 AU) on July 1, 2006, in the middle of the nominal Cassini orbital tour, is

$$S(\text{e}^-/\text{pixel}) = I/F * w_0 * t_{\text{exp}}.$$

To convert to DN, the relation is:

$$\text{DN} = S(\text{e}^-/\text{pixel})/\text{GS}(\text{e}^-/\text{DN}),$$

where GS is the gain state value in  $\text{e}^-/\text{DN}$  given in Table X. The  $\omega_0$  values were calculated starting with the ISS component ground calibrations for the transmission

TABLE XV

The factor,  $\omega_0^{\text{WAC}}$ , relating the brightness of the target,  $I/F$ , to the signal,  $S$  (electrons/pixel), and exposure time in the WAC camera.

F1	F2	$\lambda_{\text{cen, WAC}}$	$\omega_0^{\text{WAC}}$
CL1	VIO	420	8.61E+04
CL1	BL1	460	1.08E+06
CL1	GRN	567	4.76E+06
CL1	CL2	635	1.32E+07
CL1	RED	648	5.86E+06
CL1	HAL	656	3.48E+05
CL1	IRP90	710	3.65E+06
CL1	IRP0	710	3.65E+06
MT2	CL2	728	1.40E+05
MT2	IRP90	728	6.48E+04
MT2	IRP0	728	6.48E+04
CL1	IR1	742	4.00E+06
CB2	IR1	752	2.74E+05
CB2	CL2	752	2.94E+05
CB2	IRP90	752	1.39E+05
CB2	IRP0	752	1.39E+05
IR2	IR1	826	2.56E+05
IR2	CL2	853	5.68E+05
IR2	IRP90	853	2.80E+05
IR2	IRP0	853	2.80E+05
MT3	CL2	890	2.90E+04
MT3	IRP90	890	1.43E+04
MT3	IRP0	890	1.43E+04
IR3	CL2	918	1.58E+05
IR3	IRP90	918	7.81E+04
IR3	IRP0	918	7.81E+04
CB3	CL2	939	8.39E+03
CB3	IRP90	939	4.16E+03
CB3	IRP0	939	4.16E+03
IR4	CL2	1001	9.31E+03
IR4	IRP90	1001	4.62E+03
IR4	IRP0	1001	4.62E+03
IR5	CL2	1028	1.15E+03
IR5	IRP90	1028	5.72E+02
IR5	IRP0	1028	5.72E+02

of the optics, filters, quantum efficiency, shutter performance and gain. Of these, uncertainty in the quantum efficiency (approximately 20%) dominates the uncertainty budget. (In comparison, the uncertainty of stellar fluxes is on the order of 10%, which is the uncertainty we expect to achieve when calibration is complete.) In flight, we relied primarily on photometric standard stars with ancillary information from calibrated observations of Jupiter, Saturn and Saturn's rings.

For the NAC  $\omega_0$  factors, we used standard star images taken during cruise. Specifically, HD339479 images from cruise load C26 were used, as well as Vega and 77 Tau images from loads C37 and C40. Spectra for HD339479 and 77 Tau were taken from the Bruzual-Persson-Gunn-Stryker Spectrophotometric Atlas, Space Telescope Science Institute Data Analysis System (Gunn and Stryker, 1983); the spectrum for Vega was taken from Colina *et al.* (1996).

All images were processed using the CISSCAL calibration software, and aperture photometry was performed using IDL. Filter-specific correction factors were then calculated by taking the ratio of the observed integrated stellar fluxes to the expected values. The resulting correction factors varied smoothly with the central wavelength of the filter combination, and so a quantum efficiency correction function was derived to apply to the system transmission integral. With this correction in place, the images were calibrated yet again, and aperture photometry was performed as before. Residual sensitivity offsets were then taken into account by calculating filter-specific correction factors. The resulting NAC  $\omega_0$  values, which are recorded in Table XIV, have errors on the order of 10–20%, due largely to photometric uncertainty and systematic effects such as the contribution of noise from the horizontal banding (Figure 31) as well as the lack of an adequate dark current model. In general, values for the single broad-band filters are 5–10% less uncertain than those for narrow-band and combination filters.

Due in part to a lack of sufficient standard star images, and also in order to take advantage of as many illuminated pixels as possible, we did not repeat the above analysis for the WAC, but instead used November 2003 approach images of Saturn. Photometry was performed for all available filter combinations, and the resulting disk-and-ring-integrated fluxes were plotted as a function of wavelength for both the NAC and WAC. From this, a quantum efficiency correction was derived analogous to that described earlier for the NAC. No filter-specific correction factors have been calculated yet, as was done for the NAC, and therefore no residual sensitivity offsets have yet been computed. Because of this, and because the WAC sensitivity correction is tied to the accuracy of the NAC analysis, the resultant WAC  $\omega_0$  factors exhibit varying uncertainties on the order of 15–25%, depending on the filter combination.

Tables XIV and XV give the  $\omega_0$  factors for the most common NAC and WAC filters and filter combinations.

### Acknowledgments

A great many people over the last 13.5 years have contributed to the success of the Cassini Imaging Science experiment. It would be an impossible task to name every one. Special thanks go to the engineers at JPL with whom the Imaging Team had the pleasure of working in designing and developing the cameras in the pre-launch years: notable among them are Tom Livermore, William Harris, Cindy Kahn, Len Snyder, and Lloyd Adams. We also thank the scientists, engineers and others across the imaging team and at JPL who have either made significant contributions in the pre-launch years to the calibration of the instrument or are currently responsible for various aspects of the operations and in-flight calibration of the ISS: John Barbara, Michael Belanger, Emma Birath, Rachel Carson, Sebastien Charnoz, Chris Clark, Tilmann Denk, Preston Dyches, Mike Evans, Joe Ferrier, Heidi Finn, Kevin Grazier, Paul Helfenstein, Pauline Helfenstein, Bob Jacobson, Dyer Lytle, Nicole Martin, Dave O'Brien, Leslie Pieri, Jon Proton, Josh Riley, Diane Sherman, Joseph Spitale, Elizabeth Turtle, Ashwin Vasavada, Daren Wilson, Charlie Avis, Amy Culver, John Diehl, James Gerhard, Tina Pavlicek, Candy Hansen, Brad Wallis, and others. We also thank Phillip Dumont at JPL whose code was used to calculate contrasts on Titan.

### References

- Allison, M., Del Genio, A. D., and Zhou, W.: 1995, *Geophys. Res. Lett.* **22**, 2957.  
 Allison, M., Godfrey, D. A., and Beebe, R. F.: 1990, *Science* **247**, 1061.  
 Allison, M.: 2000, *Planet Space Sci.* **48**, 753.  
 Banfield, D., Gierasch, P. J., Bell, M., Ustinov, E., Ingersoll, A. P., Vasavada, A. R., *et al.* : 1998, *Icarus* **135**, 230.  
 Baum, W. A., *et al.*: 1981, *Icarus* **47**, 84–96.  
 Bell, J. F., Cruikshank, D. P., and Gaffey, M. J.: 1985, *Icarus* **61**, 192.  
 Bierhaus, E. B., Chapman, C. R., Merline, W. J., Brooks, S. M., and Asphaug, E.: 2001, *Icarus* **153**, 264–276.  
 Bird, M. K., Dutta-Roy, R., Heyl, M., Allison, M., Asmar, S. W., Folkner, W. M., Preston, R. A., Atkinson, D. H. *et al.*: 2002, *Space Sci. Rev.* **104**, 613.  
 Borderies, N., Goldreich, P., and Tremaine, S.: 1982, *Nature* **299**, 209–211.  
 Borderies, N., Goldreich, P., and Tremaine, S.: 1983, *Icarus* **55**, 124–132.  
 Bosh, A. and Rivkin, A.: 1996, *Science* **272**, 518–521.  
 Brahic, A.: 1977, *Astron. Astrophys.* **54**, 895–907.  
 Brown, M. E., Bouchez, A. H., and Griffith, C. A.: 2002, *Nature* **420**, 795–797.  
 Buratti, B. J., Mosher, J. A., Nicholson, P. D., McGhee, C. A., and French, R. G.: 1998, *Icarus* **136**, 223–231.  
 Buratti, B., Mosher, J. A., and Johnson, T. V.: 1990, *Icarus* **87**, 339–357.  
 Buratti, B. J., and Veverka, J.: 1984, *Icarus* **58**, 254–264.  
 Buratti, B. J.: 1984, *Icarus* **59**, 392–405.  
 Buratti, B. J.: 1985, *Icarus* **61**, 208–217.  
 Buratti, B. J.: 1988, *Icarus* **75**, 113–126.  
 Burns, J. A., *et al.*: 1984, in: *Planetary Rings*, University of Arizona Press, Tucson, p. 200.

- Burns, J. A., Hamilton, D. P., and Showalter, M. R.: 2001, in: Grun, E., Gustafson, B. A. S., Dermott, S. F., and Fechtig, H. (eds.), *Interplanetary Dust*, Springer, Berlin, pp. 641–725.
- Burns, J. A., Kolvoord, R. A., and Hamilton, D. P.: 1989, *An Assessment of Potential Hazards to the Cassini Spacecraft from Debris Along Satellite Orbits. Cassini Mission: Saturn Orbiter Proposal Information Package*, Vol. XIII, JPL D-6464, pp. 6-1–6-23.
- Burns, J. A., Showalter, M. R., Hamilton, D. P., Nicholson, P. D., dePater, I., and Thomas, P. C.: 1999, *Science* **284**, 1146.
- Campbell, D. B., Black, G. J., Carter, L. M., and Ostro, S. J.: 2003, *Science* **302**, 431–434.
- Campbell, J. K. and Anderson, J. D.: 1989, *Astron. J.* **97**, 1485–1495.
- Carr, M. H., *et al.*: 1998, *Nature* **391**, 363–365.
- Chandrasekhar, S.: 1960, *Radiative Transfer*, Dover, New York.
- Chapman, C. R. and McKinnon, W. B.: 1986, in: *Satellites*, University of Arizona Press, Tucson, AZ, p. 492.
- Chapman, C. R., Merline, W. J., Bierhaus, B., and Brooks, S.: 1998, LPSC XXIC, abstract #1927.
- Colas, F., Frappa, E., Gomez, J., Laques, P., Lecacheux, J., and Tagger, M.: 1995, *International Astronomical Union Circular 6129*, Saturn.
- Colina, L., Bohlin, R. C., and Castelli, F.: 1996, in *Observatory Support Group Instrument Science Report (ISR CAL/SCS-008)*.
- Colombo, G., Goldreich, P., and Harris, A. W.: 1976, *Nature* **264**, 344–345.
- Cook, A. F. and Franklin, F. A.: 1970, *Icarus* **13**, 282–291.
- Cooke, M. L.: 1991, ‘Saturn’s Rings: Radial Variation in the Keeler Gap and C Ring Photometry’, *Ph.D. Thesis*, Cornell University.
- Croft, S. K., Lunine, J. I., and Kargel, J.: 1988, *Icarus* **73**, 279–293.
- Cruikshank, D. P., Roush, T. L., Owen, T. C., Geballe, T. R., Dalle, C. M., Ore, B. N., *et al.*: 1999, *Am. Astron. Soc. Bull.* **31**, 302.
- Cruikshank, D. P.: 1981, *Icarus* **41**, 246–258.
- Cruikshank, D. P., Veverka, J., and Lebofsky, L. A.: 1984, in: *Saturn*, University of Arizona Press, Tucson, AZ, pp. 640–667.
- Cruikshank, D. P., Bell, J. F., Gaffey, M. J., Brown, R. H., Howell, R., Beerman, C., *et al.*: 1983, *Icarus* **53**, 90–104.
- Cuzzi, J. N., Lissauer, J. J., and Shu, F. H.: 1981, *Nature* **292**, 703–707.
- Cuzzi, J. N., Lissauer, J. J., Esposito, L. W., Holberg, J. B., Marouf, E. A., Tyler, G. L., *et al.* (eds.), *Planetary Rings*, University of Arizona Press, Tucson, pp. 73–199.
- Cuzzi, J. N., Durisen, R. H., Burns, J. A., and Hamill, P.: 1979, *Icarus* **38**, 54–68.
- Cuzzi, J. N. and Scargle, J. D.: 1985, *Astrophys. J.* **292**, 276–290.
- Cuzzi, J. N. and Burns, J. A.: 1988, *Icarus* **74**, 284.
- Daisaka, H. and Ida, S.: 1999, *Earth Planet Space* **51**, 1195–1213.
- Daisaka, H., Tanaka, H., and Ida, S.: 2001, *Icarus* **154**, 296–312.
- Davies, M. E. and Katayama, F. Y.: 1983a, *J. Geophys. Res.* **88**, 8729–8735.
- Davies, M. E. and Katayama, F. Y.: 1983b, *Icarus* **56**, 603–610.
- Davies, M. E., Colvin, T. R., Oberst, J., Zeitler, W., Schuster, P., Neukum, G., *et al.*: 1998, *Icarus* **135**, 372–376.
- Degawij, J., Andersson, L. E., and Zellner, B.: 1980, *Icarus* **44**, 520–540.
- Del Genio, A. D. and McGrattan, K. B.: 1990, *Icarus* **84**, 29.
- Del Genio, A. D. and Zhou, W.: 1996, *Icarus* **120**, 332–343.
- Del Genio, A. D., Zhou, W., and Eichler, T. P.: 1993, *Icarus* **101**, 1–17.
- Denk, T., Matz, K. D., Roatsch, T., Wolf, U., Wagner, R. J., Neukum, G., *et al.*: 2000, *Lunar Planet. Sci. Conf. XXXI*, abstract no. 1596 (CD-ROM).
- Dermott, S. F. and Thomas, P. C.: 1994, *Icarus* **109**, 241–257.
- Dermott, S. F. and Thomas, P. C.: 1988, *Icarus* **73**, 25–65.



- Dones, L., Cuzzi, J. N., and Showalter, M. R.: 1993, *Icarus* **105**, 184–215.
- Dones, L. and Porco, C. C.: 1989, *Bull. Amer. Astron. Soc.* **21**, 929.
- Dowling, T. E. and Ingersoll, A. P.: 1989, *J. Atmos. Sci.* **46**, 3256.
- Doyle, L. R. and Grün, E.: 1990, *Icarus* **85**, 168–190.
- Durham, W. B. and Stern, L. A.: 2001, *Ann. Rev. Earth Planet. Sci.* **29**, 295.
- Durisen, R. H., Bode, P. W., Cuzzi, J. N., Cederbloom, S. E., and Murphy, B. E.: 1992, *Icarus* **100**, 364–393.
- Dyudina, U. A., Ingersoll, A. P., Vasavada, A. R., and Ewald, S. P.: 2001, *Icarus* **160**, 336–349.
- Dyudina, U., Del Genio, A. D., Ingersoll, A. P., Porco, C. C., West, R. A., Vasavada, A. R. *et al.*: 2004, *Icarus*, in press.
- Ellsworth, K. and Schubert, G.: 1983, *Icarus* **54**, 490–510.
- Engel, S., Lunine, J. I., and Hartmann, W. K.: 1995, *Planet. Space Sci.* **43**, 1059–1066.
- Esposito, L. W., Harris, C. C., and Simmons, K. E.: 1987, *Astrophys. J. Suppl.* **63**, 749–770.
- Esposito, L. W., Cuzzi, J. N., Holberg, J. B., Marouf, E. A., Tyler, G. L., and Porco, C. C.: 1984, in: Gehrels, T., and Matthews, M. S. (eds.), *Saturn*, University of Arizona Press, Tucson, pp. 463–545.
- Esposito, L. W., O’Callaghan, M., and West, R. A.: 1983, *Icarus* **56**, 439–452.
- Estrada, P. R. and Cuzzi, J. N.: 1996, *Icarus* **122**, 251–272.
- Fanale, F. P., *et al.*: 1998, *Icarus* **139**, 179–188.
- Federico, C. and Lanciano, P.: 1983, *Ann. Geophys.* **1**, 469–476.
- Figueredo, P. H., Chuang, F. C., Rathbun, J., Kirk, R. L., and Greeley, R.: 2002, *J. Geophys. Res.* **107**, NO.E5, 10.1029 (2001JE001591).
- Flasar, F. M., Samuelson, R. E., and Conrath, B. J.: 1981, *Nature* **292**, 693–698.
- Flasar, F. M., Samuelson, R. E., and Conrath, B. J.: 1981, *Nature* **292**, 693.
- Franklin, F. A. and Colombo, G.: 1978, *Icarus* **33**, 279–287.
- Franz, O. G., Millis, R. L.: 1975, *Icarus* **24**, 433–442.
- French, R. G. and Nicholson, P. D.: 2000, *Icarus* **145**, 502–523.
- French, R. G., Cuzzi, J. N., Danos, R., Dones, L., and Lissauer, J.: 1998, in: *The Jovian System After Galileo, The Saturnian System Before Cassini-Huygens*, International Symposium, Nantes, France, 11–15 May, 1998.
- French, R. G., Dones, L., and Salo, H.: 2000, *DDA Meeting #31 of the American Astronomical Society*, abstract #08.02.
- French, R. G.: 2003, *Icarus* **162**, 143–170.
- Gault, D. E. and Sonett, C. P.: 1982, *Geol. Soc. Amer.*, Special Paper **190**, 69.
- Gierasch, P. J., Ingersoll, A. P., Banfield, D., Ewald, S. P., Helfenstein, P., Simon-Miller, A., *et al.*: 2000, *Nature* **403**, 628.
- Giese B., Oberst, J., Roatsch, T., Neukum, G., Head, J. W., and Pappalardo, R. T.: 1998, *Icarus* **135**, 303–316.
- Giese, B., Oberst, J., and Kirk, R.: 1996, *ISPRS*, Vol. 31, Part B3, Vienna, pp. 245–250.
- Gladman, B., Kavelaars, J. J., Holman, M., Nicholson, P. D., Burns, J. A., Hergenrother, C. W., *et al.*: 2001, *Nature* **412**, 163.
- Goertz, C. K. and Morfill, G.: 1983, *Icarus* **53**, 219–229.
- Goguen, J., Trippico, M., and Morrison, D.: 1983, *Bull. Am. Astron. Soc.* **15**, 855.
- Goldreich, P. and Tremaine, S. D.: 1978, *Icarus* **34**, 240–253.
- Goldreich, P., Rappaport, N., and Sicardy, B.: 1995, *Icarus* **118**, 414–417.
- Golombek, M. P. and Allison, M. L.: 1981, *Geophys. Res. Lett.* **8**, 1139.
- Gomez, D., Pietro, O., Rodriguez, M. A.: 1996, *Lunar Planet. Sci. Conf.* **27**, 433.
- Grasset, O., Sotin, C., Deschamps, F.: 2000, *Planet. Space Sci.* **48**, 617–636.
- Gresh, D. L., Rosen, P. A., Tyler, G. L., and Lissauer, J. J.: 1986, *Icarus* **68**, 481–502.

- Griffith, C. A., Owen, T., Miller, G., and Geballe, T.: 1998, in: *Paper Presented at 'The Jovian System after Galileo, The Saturnian System before Cassini (Huygens'*, Nantes, France.
- Griffith, C. A., Owen, T., Geballe, T. R., Rayner, J., and Rannou, P.: 2003, *Science* **300**, 628–630.
- Grün, E., Goertz, C. K., Morfill, G. E., and Havnes, O.: 1992, *Icarus* **99**, 191–201.
- Gunn, J. E. and Stryker, L. L.: 1983, *Ap. J. Suppl. Ser.* **52**, 121.
- Haff, P. K., Eviatar, A., and Siscoe, G. L.: 1983, *Icarus* **56**, 426–438.
- Hamilton, D. P. and Burns, J. A.: 1994, *Science* **264**, 550–553.
- Hänninen, J. and Salo, H.: 1994, *Icarus* **108**, 325–346.
- Hänninen, J. and Salo, H.: 1995, *Icarus* **117**, 435–438.
- Hansen, J. E. and Travis, L. D.: 1974, *Space Sci. Rev.* **16**, 527–610.
- Hapke, B.: 1981, *J. Geophys. Res.* **86**, 3039–3054.
- Hapke, B.: 1984, *Icarus* **59**, 41–59.
- Hapke, B.: 1986, *Icarus* **67**, 264–280.
- Harper, D. and Taylor, D. B.: 1993, *Astron. Astrophys.* **268**, 326–349.
- Hartmann, W. K.: 1984, *Icarus* **60**, 56.
- Hillier, J. K. and Squyres, S. W.: 1989, *Bull. Am. Astron. Soc.* **21**, 983.
- Horn, L. J. and Cuzzi, J. N.: 1996, *Icarus* **119**, 285–310.
- Hourdin, F., Talagrand, O., Sadourny, R., Courtin, R., Gautier, D., and McKay, C. P.: 1995, *Icarus* **117**, 358–374.
- Hubbard, et al.: 1993, 'The occultation of 28 Sgr by Titan', *Astron. & Astrophys.* **269**, 541–563.
- Hueso, R. and Sanchez-Lavega, A.: 2001, *Icarus* **151**, 257.
- Ingersoll, A. P., Beebe, R. F., Conrath, B. J., and Hunt, G. E.: 1984, in: Gehrels, T., and Matthews, M. S. (eds.), *Saturn*, University of Arizona Press, Tucson, p. 195.
- Ingersoll, A. P., Gierasch, P. J., Banfield, D., Vasavada, A. R., and the Galileo Imaging Team: 2000, *Nature* **403**, 630.
- Ingersoll, A. P., Vasavada, A. R., Little, B., Anger, C. D., Bolton, S. J., Alexander, C., et al.: 1998, *Icarus* **135**, 251.
- Ingersoll, A. P.: 1990, *Science* **248**, 308.
- Jankowski, D. G. and Squyres, S. W.: 1988, *Science* **241**, 1322–1325.
- Jarvis, K. S., Vilas, F., Larson, S. M., and Gaffey, M. J.: 2000, *Icarus* **146**, 125–132.
- Jeffreys, H.: 1947, *Monitor. Not. R. Astron. Soc.* **107**, 263–267.
- Johnson, T. V., Veeder, G. J., and Matson, D. L.: 1975, *Icarus* **24**, 428–432.
- Kahn, C. and King, W.: 1996, *Cassini/Huygens: A Mission to the Saturnian System*, SPIE, Vol. 2803, pp. 187–196.
- Kargel, J. S. and Pozio, S.: 1996, *Icarus* **119**, 385–404.
- Kargel, J. S. and Croft, S. K.: 1989, *Lunar Planet. Sci.* **XX**, 500.
- Kargel, J. S., Croft, S. K., Lunine, J. I., and Lewis, J. S.: 1991, *Icarus* **89**, 93–112.
- Kirk, R. L., Howington-Kraus, E., Redding, B., Galuszka, D., Hare, T. M., Archinal, B. A., et al.: 2003, *J. Geophys. Res.* **108**, E12, ROV 29-1.
- Kivelson, M. G., et al.: 2004, in: Bagenal, F. (ed.), *Jupiter: The Planet, Satellites, and Magnetosphere*, Cambridge University Press, Cambridge.
- Larson, S. M., Fountain, J. W., Smith, B. A., and Reitsema, H. J.: 1981, *Icarus* **47**, 288–290.
- Lemmon, M. T.: 1994, 'Properties of Titan's Haze', *Ph.D. Dissertation*, University of Arizona.
- Lewis, J. S.: 1972, *Icarus* **16**, 241–252.
- Lewis, M. C. and Stewart, G. R.: 2000, *Astron. J.* **120**, 3295–3310.
- Li, L., Ingersoll, A., Vasavada, A. R., Porco, C. C., Del Genio, A. D., and Ewald, S. P.: 2004, *Icarus*, in press.
- Lindal, G. F., Wood, G. E., Hotz, H. B., and Sweetnam, D. N.: 1983, *Icarus* **53**, 348–363.
- Lissauer, J. J.: 1985, *Icarus* **62**, 433–447.
- Lissauer, J. J., Shu, F. H., and Cuzzi, J. N.: 1981, *Nature* **292**, 707–711.

- Lissauer, J. J., Squyres, S. W., and Hartmann, W. K.: 1988, *J. Geophys. Res.* **93**, 13776.
- Little, B., Anger, C. D., Ingersoll, A. P., Vasavada, A. R., Senske, D. A., Breneman, H. H., *et al.*: 1999, *Icarus* **142**, 306.
- Lopes-Gautier, R., *et al.*: 1998, *Icarus* **140**, 243–264.
- Lorenz, R. D.: 1997, *Planet. Space Sci.* **45**, 1009–1019.
- Lucchitta, B. K.: 1980, *Icarus* **44**, 481.
- Lunine, J. I. and Soderblom, L. A.: 2002, *Space Sci. Rev.* **118**, 191–208.
- Lunine, J. I. and Lorenz, R. D.: 1996, *SPIE*, **2803**, 45–54.
- Lunine, J. I. and Stevenson, D. J.: 1985, *Ices in the Solar System*, D. Reidel Publishers, p. 741.
- Lunine, J. I., Lorenz, R. D., and Hartmann, W. K.: 1998, *Planet. Space Sci.* **46**, 1099–1107.
- Malin, M. C., Danielson, G. E., Ravine, M. A., and Soulanille, T. A.: 1992, *J. Geophys. Res.* **97**, 7699–7718.
- Marley, M. S. and Porco, C. C.: 1993, *Icarus* **106**, 508–524.
- Marouf, E. A., Tyler, G. L., and Rosen, P. A.: 1986, *Icarus* **68**, 120–166.
- McCord, T. B., Johnson, T. V., and Elias, J. H.: 1971, *Astrophys. J.* **165**, 413–424.
- McGhee, C., French, R., Dones, L., Cuzzi, J., Salo, H. J., and Danos, R.: 2004, *Icarus*, in press.
- McKinnon, W. B.: 1985, *Bull. Am. Astron. Soc.* **17**, 922.
- Melosh, H. J., Janes, D. M., Jankowski, D. G., and Squyres, S.: 1989, *Science* **245**, 194–196.
- Moore, J. M.: 1984, *Icarus* **59**, 205–220.
- Moore, J. M. and A'Hearn, J. L.: 1983, *J. Geophys. Res.* **88**, 577.
- Moore, J. M., *et al.*: 1998, *Icarus* **140**, 294.
- Moore, J. M., Horner, V. M., and Greeley, R.: 1985, *J. Geophys. Res.* **90**, 785–795.
- Moore, J. M.: 1984, *Icarus* **59**, 205–220.
- Morfill, G., Grun, E., and Johnson, T. V.: 1983, *J. Geophys. Res.* **88**, 5573–5579.
- Murray, C. D. and Dermott, S. F.: 1999, *Solar System Dynamics*, Cambridge University Press, Cambridge.
- Murray, C. D. and Gordon, M., Giulatti-Winter, S. M.: 1997, *Icarus* **129**, 304.
- Namouni, F. and Porco, C.: 2002, *B.A.A.S.* **34**, 884.
- Namouni, F. and Porco, C.: 2002, *Nature* **417**, 45–47.
- Neukum, G., Wagner, R., Wolf, U., Ivanov, B. A., Head III, J. W., Pappalardo, R. T., *et al.*: 1998, *Lunar Planet. Sci. Conf. XXIX*, abstract no. 1742 (CD-ROM).
- Neukum, G.: 1985, *Adv. Space Res.* **5**, 107–116.
- Neukum, G.: 1997, Barbieri, in: C., Rahe, J. H., and Johnson, T. V. (eds.), *Proceedings of the Conference on The Three Galileos: The Man, The Spacecraft, The Telescope*, Padova, Italy, January 7–10, 1997, Kluwer Academic Publishers, Dordrecht, pp. 201–212.
- Nicholson, P. D. and Porco, C. C.: 1988, *J. Geophys. Res.* **93**, 10,209–10,224.
- Nicholson, P. D., Campbell, D. B., French, R. G., Black, G. J., Margot, J. L., Nolan, M.: 2000, *B.A.A.S.* **321**, 2086.
- Nicholson, P. D. *et al.*: 1996, *Science* **272**, 509–515.
- Nicholson, P. D., Hamilton, D. P., Matthews, K., and Yoder, C. F.: 1992, *Icarus* **100**, 464–484.
- Nicholson, P. D., Showalter, M. R., Dones, L., French, R. G., Larson, S. M., Lissauer, J. J., *et al.*: 1996, *Science* **272**, 509.
- Nimmo, F., Pappalardo, R. T., and Giese, B.: 2003, *Icarus* **166**, 21–32.
- Noland, M., Veverka, V., Morrison, D., Cruikshank, D. P., Lazarewicz, A. R., Morrison, N. D., *et al.*: 1974, *Icarus* **23**, 334–354.
- Oberst J., Whlisch, M., Cook, A. C., Roatsch, T., and Jaumann, R.: 1997, *EOS Trans. Am. Geophys. Union* **445**, 450.
- Oberst, J., Schreiner, J. B., Giese, B., Neukum, G., Head, J. W., Pappalardo, R., *et al.*: 1999, *Icarus* **140**, 283–293.

- Oberst, J., Giese, B., Schuster, P., Schreiner, B., Zeitler, W., Wagner, R., Roatsch, T., and Neukum, G.: 1998, in: *Euroconference on The Jovian System After Galileo—The Saturnian System Before Cassini*, May 11–15, Nantes, France, pp. 72–73.
- Oberst, J., Zeitler, W., and Parker, T.: 1999, *EOS Trans. Am. Geophys. Union* **80** (46), 549–553.
- Oberst, J. and Schuster, P.: 2004, *J. Geophys. Res.* **109**, 4003.
- Ockert, M. E., Cuzzi, J. N., Porco, C. C., and Johnson, T. V.: 1987, *J. Geophys. Res.* **92**, 14,969–14,978.
- Owen, T. C., Cruickshank, D. P., Dalle Ore, C. M., Geballe, T. R., Roush, T. L., DeBergh, C.D., *et al.*: 2001, *Icarus* **149**, 160–172.
- Pang, K., Voge, C. C., Rhoads, J. W., and Ajello, J. M.: 1984, *J. Geophys. Res.* **89**, 9459–9470.
- Parmentier, E. M., Squyres, S. W., Head, J. W., and Allison, M. L.: 1982, *Nature* **295**, 290.
- Passey, Q. R.: 1983, *Icarus* **53**, 105.
- Pechmann, J. B. and Ingersoll, A. P.: 1984, *J. Atmos. Sci.* **41**, 3290–3313.
- Plescia, J. B. and Boyce, J. M.: 1985, *J. Geophys. Res.* **90**, 2029.
- Plescia, J. B.: 1987, *Nature* **327**, 201.
- Plescia, J. B.: 1983, *Icarus* **56**, 255–277.
- Polvani, L. M., Wisdom, J., De Jong, E., and Ingersoll, A. P.: 1990, *Science* **249**, 1393.
- Porco, C. C.: 1990, *Adv. Space Res.* **10**, 221–229.
- Porco, C. C. and Danielson, G. E.: 1982, *Astron. J.* **87**, 826–833.
- Porco, C. C. and Danielson, G. E.: 1984, in: Brahic, A. (ed.), *Proceedings of IAU Colloquium #75, Planetary Rings*, CNES, Toulouse, France, p. 219.
- Porco, C. C. and Nicholson, P. D.: 1987, *Icarus* **72**, 437–467.
- Porco, C. C., Pantazopoulou, M., Throop, H., Richardson, D., Quinn, T., Kehoe, T. J. J., *et al.*: 2005, ‘Light Scattering in Saturn’s Rings: Basic Formulation, Ring Thickness and the A Ring Azimuthal Asymmetry’, manuscript in preparation.
- Porco, C. C., Throop, H. B., and Richardson, D. C.: 2001, in: *DPS Meeting #33 of the American Astronomical Society*, abstract #29.01.
- Porco, C. C., Pantazopoulou, M. J., Richardson, D., Quinn, T., and Kehoe, T. J. J.: 1999, in: *DPS Meeting #31 of the American Astronomical Society*, abstract #44.03.
- Porco, C., Nicholson, P. D., Borderies, N. B., Danielson, G. E., Goldreich, P., Holberg, J. B., *et al.*: 1984a, *Icarus* **60**, 1.
- Porco, C., Danielson, G. E., Goldreich, P., Holberg, J. B., and Lane, A. L.: 1984b, *Icarus* **60**, 17–28 (erratum in *Icarus* **61**, 173).
- Porco, C. C. *et al.*: 2003, *Science* **299**, 1469.
- Porco, C. C. and Goldreich, P.: 1987, *Astron. J.* **93**, 724–729.
- Porco, C. C.: 1991, *Science* **253**, 995.
- Porco, C. C., Cuzzi, J. N., Ockert, M. E., and Terrile, R. J.: 1987, *Icarus* **72**, 69–78.
- Prockter, L. M. and Pappalardo, R. T.: 2003, *Lunar Planet. Sci. Conf.* **34**, abstract 1620.
- Poulet, F., Cuzzi, J. N., French, R. G., and Dones, L.: 2002, *Icarus* **158**, 224.
- Prinn, R. G. and Fegley, B.: 1981, *Astrophys. J.* **249**, 308–317.
- Rappaport, N.: 1998, *Icarus* **132**, 36–42.
- Raulin, F. and Owen, T.: 2002, *Space Sci. Rev.* **104**, 377–394.
- Rebiai, R., Scurlock, R. G., and Rest, A. J.: 1984, *Adv. Cryogen. Eng.* **29**, 1005.
- Reynolds, R. T. and Cassen, P. M.: 1979, *Geophys. Res. Lett.* **6**, 121.
- Richardson, D. C.: 1994, *Monitor. Not. R. Astron. Soc.* **269**, 493–511.
- Richardson, D. C.: 1995, *Icarus* **115**, 320.
- Richardson, D. C., Quinn, T., Stadel, J., and Lake, G.: 2000, *Icarus* **143**, 45–59.
- Richardson, J., Lorenz, R. D., and McEwen, A. S.: 2004, *Icarus* **170**, 113–124.

- Roddier, C., Roddier, F., Graves, J. E., and Northcutt, M. J.: 1998, *Icarus* **136**, 50.
- Roe, H. G., De Pater, I., Macintosh, B. A., and McKay, C. P.: 2002, *Astrophys. J.* **581**, 1399–1406.
- Rosen, P. A., Tyler, G. L., Marouf, E. A., and Lissauer, J. J.: 1991, *Icarus* **93**, 25–44.
- Ross, M. N. and Schubert, G.: 1988, *Icarus* **75**, 479–484.
- Ross, M. N. and Schubert, G.: 1989, *Icarus* **78**, 90–101.
- Rossow, W. B. and Williams, G. P.: 1979, *J. Atmos. Sci.* **36**, 377–389.
- Safronov, V. S. and Ruskol, E. L.: 1977, *Planetary Satellites*, University of Tucson Press, Acizona/Tucson pp. 505–512.
- Safronov, V. S.: 1972, 'Evolution of the protoplanetary cloud and formation of the Earth and planets', NASA TT-F-677.
- Safronov, V. S., Perchernikova, G. V., Ruskol, E. L., and Vitjazev, A. V.: 1986, *Satellites*, University of Arizona Press, Tucson, pp. 89–116.
- Sagan, C. and Dermott, S. F.: 1982, *Nature* **300**, 731.
- Sagan, C. and Thompson, W. R.: 1984, *Icarus* **59**, 133.
- Salo, H.: 1992, *Nature* **359**, 619–621.
- Salo, H.: 1995, *Icarus* **117**, 287–312.
- Salo, H., Schmidt, J., and Spahn, F.: 2001, *Icarus* **153**, 295–315.
- Salo, H., Karjalainen, R., and French, R. G.: 2000, in: *DDA Meeting #31 of the American Astronomical Society*, abstract #08.01.
- Sanchez-Lavega, A., Colas, F., Lecacheux, J., Laques, P., Miyazaki, I., and Parker, D.: 1991, *Nature* **353**, 397.
- Sanchez-Lavega, A., *et al.*: 1996, *Science* **271**, 631.
- Sanchez-Lavega, A., Lecacheux, J., Colas, F., Rojas, J. F., and Gomez, J. M.: 1999, *Planet. Space Sci.* **47**, 1277.
- Sanchez-Lavega, A., Perez-Hoyos, F., Rojas, J. F., Hueso, R., and French, R. G.: 2003, *Nature* **423**, 623.
- Schenk, P. M. and Moore, J. M.: 1995, *J. Geophys. Res.* **100**, 19009–19022.
- Schenk, P. M.: 2002, *Nature* **417**, 419–421.
- Schenk, P. M.: 1989, *J. Geophys. Res.* **94**, 3813–3832.
- Schenk, P. M.: 1991, *J. Geophys. Res.* **96**, 1887–1906.
- Schenk, P. M., Chapman, C., Zahnle, K., and Moore, J.: 2004, in: Bagenal, F., Downing, T. E., and McKinnon, W. B. (eds.), *Jupiter: The Planet, Satellites, and Magnetosphere*, Cambridge University Press, Cambridge (chapter 18).
- Schenk, P. M., Wilson, R. R., and Davies, A. G.: 2004, *Icarus* **169**, 98–110.
- Schmidt, J., Salo, H., Spahn, F., and Petzschmann, O.: 2001, *Icarus* **153**, 316–331.
- Schmit, U. and Tscharnuter, W. M.: 1999, *Icarus* **138**, 173–187.
- Schubert, G., Anderson, J. D., Spohn, T., and McKinnon, W. B.: 2004, in: Bagenal, F. (ed.), *Jupiter: The Planet, Satellites, and Magnetosphere*, Cambridge University Press, Cambridge (chapter 13).
- Schubert, G., Stevenson, D. J., and Ellsworth, K.: 1981, *Icarus* **47**, 46.
- Shoemaker, E. M.: 1960, *International Geological Conference XXI*, Norden, vol. 21, p. 418.
- Showalter, M. R., Cuzzi, J. N., Marouf, E. A., and Esposito, L. W.: 1986, *Icarus* **66**, 297–323.
- Showalter, M. R.: 1991, *Nature* **351**, 709–713.
- Showalter, M. R. and Cuzzi, J. N.: 1993, *Icarus* **103**, 124.
- Showalter, M. R., Cuzzi, J. N., and Larson, S.: 1991, *Icarus* **94**, 451.
- Showalter, M. R.: 1996, *Icarus* **124**, 667.
- Showalter, M. R.: 1998, *Science* **282**, 1099.
- Shu, F. H.: 1984, in: Greenberg, R., and Brahic, A. (eds.), *Planetary Rings*, University of Arizona Press, Tucson, pp. 513–561.
- Shu, F. H., Cuzzi, J. N., and Lissauer, J. J.: 1983, *Icarus* **53**, 185–206.

- Sicardy, B., Brahic, A., Ferrari, C., Gautier, D., Lecacheux, J., Lellouch, E., *et al.*: 1990, *Nature* **343**, 350–353.
- Simonelli, D. P., Kay, J., Adinolfi, D., Veverka, J., Thomas, P. C., and Helfenstein, P.: 2000, *Icarus* **138**, 249–255.
- Smith, B. A., Soderblom, L. A., Johnson, T. V., Ingersoll, A. P., Collins, S. A., Shoemaker, E. M., *et al.*: 1979a, *Science* **204**, 951.
- Smith, B. A., Soderblom, L. A., Beebe, R., Boyce, J., Briggs, G., Carr, M., *et al.*: 1979b, *Science* **206**, 927.
- Smith, B. A., *et al.*: 1981, *Science* **212**, 163–191.
- Smith, B. A., *et al.*: 1982, *Science* **215**, 504–537.
- Smith, B. A., *et al.*: 1986, *Science* **233**, 43.
- Smith, B. A., *et al.*: 1990, *Science* **246**, 1422.
- Smith, P. H., Lemmon, M. T., Lorenz, R. D., Sromovsky, L. A., Caldwell, J. J., and Allison, M. D.: 1996, *Icarus* **119**, 336.
- Soter, S.: 1974, Proceedings, IAU Planetary Satellites Conf., Cornell University.
- Squyres, S. W. and Croft, S. K.: 1986, *Satellites*, University of Arizona Press, Tucson, pp. 293–341.
- Squyres, S. W. and Sagan, C.: 1983, *Nature* **303**, 782–785.
- Squyres, S. W., Buratti, B., Veverka, J., and Sagan, C.: 1984, *Icarus* **59**, 426–435.
- Squyres, S. W., Reynolds, R. T., Summers, A. L., and Shung, F.: 1988, *J. Geophys. Res.* **93**, 8779–8794.
- Squyres, S. W., Reynolds, R. T., Cassen, P. M., and Peale, S. J.: 1983, *Icarus* **53**, 319–331.
- Squyres, S. W.: 1980, *Geophys. Res. Lett.* **7**, 593–596.
- Stevenson, D. J.: 1992, *Proceedings of the Symposium on Titan*, Toulouse, France, September 9–12, 1991, ESA SP-338, ESA Publication Division, ESTEC, Noordwijk, The Netherlands, pp. 29–33.
- Stevenson, D. J.: 1982, *Nature* **298**, 142–144.
- Strom, R. G.: 1981, *Lunar Planet. Sci. XII, Suppl. A.*, **7**.
- Tholen, D. J. and Zellner, B.: 1983, *Icarus* **53**, 341–347.
- Thomas, P., Veverka, J., Morrison, D., Davies, M., and Johnson, T. V.: 1983, *J. Geophys. Res.* **88**, 8736–8742.
- Thomas, P. C. and Dermott, S. F.: 1991, *Icarus* **94**, 391–398.
- Thomas, P. C., Black, G. J., and Nicholson, P. D.: 1995, *Icarus* **117**, 128–148.
- Thomas, P. G.: 1988, *Icarus* **74**, 554–567.
- Thomas, P. J. and Squyres, S. W.: 1988, *J. Geophys. Res.* **93**, 14919–14932.
- Thompson, W. T., Lumme, K., Irvine, W. M., Baum, W. A., and Esposito, L. W.: 1981, *Icarus* **46**, 187–200.
- Throop, H. B. and Esposito, L. W.: 1998, *Icarus* **131**, 152.
- Throop, H. B., Porco, C. C., West, R. A., Burns, J. A., Showalter, M. R., and Nicholson, P. D.: 2004, *Icarus*, in press.
- Tobiska, W. K., Woods, T., Eparvier, F., Viereck, R., Floyd, L., Bouwer, D., *et al.*: 2000, *J. Atm. Solar Terr. Phys.* **62** (14), 1233–1250.
- Tokono, T. and Neubauer, F. M.: 2002, *Icarus* **158**, 499–515.
- Tomasko, M. G. and 13 others: 2002, *Space Sci. Rev.* **104**, 469–551.
- Toon, O. B., McKay, C. P., Courtin, R., and Ackerman, T. P.: 1988, *Icarus* **75**, 255.
- Trauger, J. T., Clarke, J. T., Ballester, G. E., Evans, R. W., Burrows, C. J., Crisp, D., *et al.*: 1998, *J. Geophys. Res.* **103**, 20,237.
- Tremaine S.: 2002, *Astron. J.* **125**, 894.
- Turtle, E. P. and Pierazzo, E.: 2001, *Science* **294**, 1326–1328.
- Turtle, E., *et al.*: 1990, *B.A.A.S.* **22**, 1041.
- Turtle, E. *et al.*: 1991, *B.A.A.S.* **23**, 1179.

- Vasavada, A. R., Bouchez, A. H., Ingersoll, A. P., Little, B., Anger, C. D., and the Galileo SSI Team: 1999, *J. Geophys. Res.* **104**, 27,133.
- Vasavada, A. R., Ingersoll, A. P., Banfield, D., Bell, M., Gierasch, P. J., Belton, M. J. S., *et al.*: 1998, *Icarus* **135**, 265.
- Verbiscer, A. and Veverka, J.: 1989, *Icarus* **82**, 336–353.
- Wagner, J. K., Hapke, B. W., and Wells, E. N.: 1987, *Icarus* **69**, 14–28.
- Wagner, R. and Neukum, G.: 1996, *Ann. Geophys.* **14** (Suppl. III), C794.
- Ward, W. R.: 1981, *Geophys. Res. Lett.* **8**, 641–643.
- West, R. A. and Smith, P. H.: 1991, *Icarus* **90**, 330–333.
- West, R. A., Friedson, A. J., and Appleby, J. F.: 1992, *Icarus* **100**, 245–259.
- Wilson, P. and Sagan, C.: 1995, *J. Geophys. Res.* **100**, 7531–7537.
- Wisdom, J. and Tremaine, S.: 1988, *Astron. J.* **95**, 925–940.
- Wisdom, J.: 2004, *Astron. J.* **128**, 484–491.
- Yoder, C. F.: 1979, *Nature* **279**, 767–770.
- Yoder, C. F., Colombo, G., Synnott, S. P., and Yoder, K. A.: 1984, *Icarus* **53**, 431.
- Young, R. E., Walterscheid, R. L., Schubert, G., Seiff, A., Linkin, V. M., and Lipatov, A. N.: 1987, *J. Atmos. Sci.* **44**, 2628–2639.
- Yung, Y. L., Allen, M., and Pinto, J. P.: 1984, *Astrophys. J. Suppl. Ser.* **55**, 465.
- Zahnle, K., Dones, L., and Levison, H. F.: 1998, *Icarus* **136**, 202–222.
- Zahnle, L., Schenk, P., Levison, H., and Dones, L.: 2003, *Icarus* **163**, 263–2889.
- Zebker, H. A., Marouf, E. A., and Tyler, G. L.: 1985, *Icarus* **64**, 531–548.
- Zeitler W. and Oberst, J.: 1998, *J. Geophys. Res.* **104**, 8935–8942.